UNIVERSITÉ DE MONTRÉAL

3D VISUALIZATION OF MICROVASCULAR NETWORKS USING MAGNETIC PARTICLES: APPLICATION TO MAGNETIC RESONANCE NAVIGATION

NINA OLAMAEI
INSTITUT DE GÉNIE BIOMÉDICAL
ÉCOLE POLYTECHNIQUE DE MONTRÉAL

THÈSE PRÉSENTÉE EN VUE DE L'OBTENTION
DU DIPLÔME DE PHILOSOPHIAE DOCTOR
(GÉNIE BIOMÉDICAL)
FÉVRIER 2015

UNIVERSITÉ DE MONTRÉAL

ÉCOLE POLYTECHNIQUE DE MONTRÉAL

Cette thèse intitulée :

3D VISUALIZATION OF MICROVASCULAR NETWORKS USING MAGNETIC PARTICLES: APPLICATION TO MAGNETIC RESONANCE NAVIGATION

présentée par : OLAMAEI Nina

en vue de l'obtention du diplôme de : Philosophiae Doctor

a été dûment acceptée par le jury d'examen constitué de :

Mme PÉRIÉ-CURNIER Delphine, Doctorat, présidente

Mme CHERIET Farida, Ph. D., membre et directrice de recherche

M. MARTEL Sylvain, Ph. D., membre et codirecteur de recherche

M. BEAUDOIN Gilles, Ph. D., membre

M. FERREIRA Antoine, Ph. D., membre

DEDICATION

To Parviz and Sousan

ACKNOWLEDGMENT

Though fascinating and unique as an experience, my route towards the end of this PhD program involved cumbersome challenges, the accomplishment of which would not be possible without the precious support of several people, to only some of whom it is possible to give particular mention here.

I would like to express my deep gratitude to my research supervisors, Professor Farida Cheriet, director of the "Imaging and 4D visualization" laboratory, and Professor Sylvain Martel, director of the "Nanorobotics laboratory". Farida has supported me throughout these years not only by providing an excellent guidance but also by furnishing my path with vision, motivation and encouragement. I am so grateful to Sylvain for his support and trust. His passion in research has undoubtedly been inspiring. His approach in dealing with compelling research problems and his high scientific standards set an example.

I would like to thank Dr. Sylvain Deschênes for his collaboration that made it possible for me to use the MRI facility at Saint-Justine hospital complemented by his insightful comments. I am also very grateful to Dr. Oleg Zabeida for his great help with the surface treatment of my microfluidic channels. He has been generous with his time and his vision. I would also like to thank Dr. Mahmood Mohammadi for his precious helps and comments on the generation of magnetic particles. I would like to thank Dr. Frederick Gosselin for his insightful discussions during the short time we worked together at Nanorobotics laboratory.

I am also indebted to the students I had the pleasure to work with. I am thankful to Azadeh Sharafi, Samira Taherkhani and Nasr Tabatabaei for being part of helpful discussions, their encouragement and empathy. I would like to thank Alexandre Bigot who was always willing to help and share his findings and experiences. Special thanks to Viviane Lalande, my French mentor and jogging partner, for her friendship and her time dedicated to correct my French writings. I am also grateful to other members of the Nanorobotics laboratory who each in one way or another helped me to complete this journey.

I would like to give a heartfelt, special thanks to my parents, Sousan and Parviz, and my dear sister, Raya, for their unconditional love and support from overseas. Without them, I would not have made it this far.

Finally, I would like to thank my partner and my best friend, Soroush, who has been my biggest supporter in this journey. He has taken care of whatever needed so that I could focus on my work. He has patiently read my thesis several times helping me to improve my writing skills. It was his constant help, encouragement and love that finally made it possible for me to see this project through to the end.

RÉSUMÉ

Les différentes modalités d'imagerie médicales fournissent des images cliniques de structures internes du corps humain à des fins diagnostiques et curatives. Leur première application en clinique remonte à trois décennies et depuis, grâce aux découvertes technologiques continues, de nouvelles fonctionnalités ont été intégrées aux systèmes d'imagerie. Aujourd'hui, des informations anatomiques et fonctionnelles précises peuvent être prélevées à partir de ces images dont la dimensionnalité a évolué du bidimensionnel au tridimensionnel incluant la dynamique. Une des modalités d'imagerie qui a largement profité de ces découvertes technologiques est l'imagerie par résonance magnétique (IRM). Par rapport aux autres techniques d'imagerie, l'IRM présente beaucoup d'avantages tels que la haute résolution spatiale et temporelle, le manque d'exposition aux rayonnements X et une pénétration tissulaire illimitée. Ceux-ci ont rendu l'IRM l'une des modalités les plus utilisées en clinique.

Malgré des améliorations récentes dans le fonctionnement des bobines de réception d'IRM et aussi des algorithmes de reconstruction, des progrès supplémentaires sont requis afin d'améliorer la visualisation des microstructures en clinique. La visualisation des microvaisseaux avec un diamètre de 200 µm, reste au-delà des capacités des modalités d'imageries cliniques actuelles.

Dans le traitement du cancer, une telle capacité pourrait fournir les informations nécessaires pour les nouvelles méthodes de délivrance ciblée de médicaments comme la navigation par résonance magnétique (NRM). Dans cette technique, afin d'améliorer l'indice thérapeutique, les microporteurs, chargés avec des agents thérapeutiques et des particules magnétiques, sont guidés le long d'une trajectoire qui mènerait vers une zone cancéreuse. Notre objectif est de telle trajectoire qui débuterait du bout du cathéter d'injection jusqu'à la destination finale, soit à proximité d'une zone tumorale.

Le contraste de susceptibilité magnétique dans l'IRM fournit un moyen pour prononcer l'effet d'une particule magnétique même si sa taille est beaucoup plus petite que la résolution spatiale de l'IRM. En raison de leur susceptibilité magnétique élevée, les matériaux magnétiques provoquent une inhomogénéité dans le champ magnétique local de l'IRM dans une mesure beaucoup plus importante que leur taille réelle. L'inhomogénéité apparaît dans les images de gradient écho pondéré en T_2^* sous forme d'une perte de signal. Cette approche présente un moyen de visualisation de microstructures en exploitant leur artefact de susceptibilité.

L'artefact de susceptibilité (perte de signal) a d'abord été caractérisé par des expériences de simulation sur les fantômes. L'étendue de l'artefact de susceptibilité s'est avérée corrélée avec la durée d'écho, le champ magnétique statique, la taille des particules et leur magnétisation à la saturation. Selon le temps d'écho, l'étendue de l'artefact est 75 à 146 fois et de 72 à 135 fois plus grande que la taille réelle de la particule à 3,0 T et à 1,5 T, respectivement.

Des particules magnétiques d'une taille micrométrique à forte aimantation sont classées comme matériaux ferromagnétiques. En raison de la magnétisation rémanente, l'utilisation de telles particules est limitée en clinique. Comme étape suivante, l'utilisation des agglomérations micrométriques, composées de nanoparticules superparamagnétiques, en tant qu'agents de contraste en IRM a été étudiée. Les agglomérations peuvent reproduire le comportement de microparticules magnétiques en termes d'artefact de susceptibilité dans une image. Les agglomérations ont été générées en utilisant une puce microfluidique en jonction-T. Un ferrofluide à base d'huile a été utilisé pour générer les gouttelettes d'huile dans l'eau. L'avantage d'utiliser un dispositif microfluidique est le contrôle précis de la taille des gouttelettes ainsi que leur espacement. Les microagglomérations de nanoparticules d'oxyde de fer ont été injectées dans des microcanaux de 200 μm et 50 μm de diamètre interne, respectivement. Les diamètres choisis sont dans l'échelle d'une grande et une petite artériole. Les résultats ont montré que les agglomérations de 50 μm de diamètre sont juste visibles dans les images d'une séquence d'écho de gradient rapide (TrueFISP).

Par la suite, on a étudié la précision de positionnement des particules à partir de leur effet de susceptibilité sur les images. Les images reconstruites contiennent deux types d'artefacts en présence de matériaux magnétiques: la distorsion géométrique et le déplacement d'écho. La première distorsion mène à un défaut d'alignement de la position des protons tandis que la seconde distorsion provoque une perte de signal sous forme d'une "trèfle à quatre feuilles" sur les plans frontal et sagittal et un cercle sur le plan transversal. Le déplacement d'écho génère une perte de signal d'une forme symétrique dont l'origine peut représenter la position de la particule. La distorsion géométrique déplace le centre de l'artefact et peut mener à une erreur de calcul de la position de la particule. Il a été montré que le déplacement d'écho est l'effet dominant sur la distorsion géométrique dans les séquences de gradient d'écho. Alors, la position des particules a été déterminée en se basant sur leur centre de gravité. L'erreur moyenne a été calculée et elle est environ la moitié de la taille d'un pixel. L'analyse de la dispersion a confirmé la reproductibilité des résultats.

A l'étape suivante, un réseau vasculaire 2D comprenant un canal d'entrée se diversifiant en huit canaux plus petits, en trois étapes, avec un diamètre interne de 150 µm au dernier niveau a été reconstruit. Les microagglomerations de nanoparticules d'oxyde de fer (150 ± 20 µM) ont été injectées dans un réseau vasculaire fabriqué en plexiglas en utilisant une machine de micro-usinage. Une séquence rapide multi-shot et sensible à la susceptibilité magnétique (TrueFISP) a été utilisée pour suivre les particules pendant leur injection dans le réseau. L'expérience a été répétée deux fois. La première et la deuxième expérience ont donné 70 et 114 images, respectivement. Les pertes de signal ont été identifiées visuellement et positionnées à travers leur centre de gravité. Toutes les positions ont été assemblées pour constituer la trajectoire des particules. Les résultats suggèrent que la technique peut être utilisée pour un suivi en temps réel des particules magnétiques pour regrouper les images d'un vaisseau sanguin qui est au-delà de la résolution d’un système IRM clinique.

Afin d’étendre l'approche d'une représentation 2D à 3D, nous avons proposé un nouvel algorithme basé sur la séquence TrueFISP de multi-shot et multi-tranche. La technique a été validée à l’aide d’un réseau 3D en verre. Les microagglomerations ont été injectées dans le réseau et ont été suivies dans différentes coupes. Le temps d'acquisition par coupe était de 0.6 s. L'erreur de reconstruction était plus élevée dans certains segments du réseau vasculaire. Ceci a été imposé par la limitation dans la diminution de l'épaisseur de coupe à cause de la dégradation du rapport signal sur bruit. L'erreur de mesure moyenne a été évaluée à ~ 0.4 mm.

Dans NRM, la représentation 3D des trajectoires de particules est une étape importante dans l'identification du réseau vasculaire menant au site de la tumeur. En raison de la résolution spatiale limitée des scanners d'IRM cliniques actuels, un positionnement précis des particules n’est pas possible. Cependant, le contraste de susceptibilité qui se présente dans les séquences à la base de gradient d’écho peut donner un aperçu sur la façon dont les particules sont réparties dans le champ de vision.

En conclusion, ce projet propose une nouvelle technique fiable dans la visualisation des microvaisseaux chez l’humain en utilisant un IRM clinique et les bobines réceptrices commerciales. Ceci est une étape importante dans le ciblage des tumeurs en utilisant NRM. Le suivi en temps réel des microagglomerations d'oxyde de fer mène à obtenir leur trajectoires de mouvement et les trajectoires mènent à une représentation 3D de la microvasculatures dans le corps humain qui n’est pas visibles à l'aide des modalités d’imageries cliniques actuelles. Les expériences in vivo restent pour valider l'application clinique de la technique proposée dans le cadre des futurs travaux. La carte 3D de la microvasculature alimentant un site tumoral mène à une amélioration significative de l'efficacité du ciblage de la tumeur en NRM tout en réduisant les effets secondaires de la chimiothérapie, le risque de reformage à la tumeur et des métastases aux autres organes.

ABSTRACT

Medical imaging modalities strive to provide clinical images of the human body's internal structures for diagnosis and treatment purposes. Their first application in clinical trial services goes back to three decades and owing to continuous technological inventions, new capabilities have ever since been incorporated into the imaging systems. Today, anatomical and functional data with finer details and larger image sizes can be achieved and dimensionality of the images has been increased from 2D to dynamic 3D fields. One of the imaging modalities that have probably profited the most from technological findings is the magnetic resonance imaging (MRI). Compared to the other imaging techniques, MRI has various advantages such as high spatial and temporal resolution, lack of radiation exposure and unlimited tissue penetration. These have turned the MRI to one of the most available modalities clinically.

Despite recent improvements in the MRI's receiver coils and reconstruction algorithms, further progress is yet sought to improve the visualization of the microstructures using the clinical MR scanners. Visualization of microvessels with an inner overall cross-sectional area of approximately less than 200 μm, remains beyond capabilities of the current clinical imaging modalities. In cancer therapy, such capability would provide the information required for the new delivery methods such as magnetic resonance navigation (MRN). In the MRN, to enhance the therapeutic index, microcarriers loaded with therapeutic agents and magnetic particles are navigated along a planned trajectory in the vicinity of the treatment region. Our objective is to provide such a trajectory map within an area covering the location of the catheter tip for the injection site up to the extremity of the particles' path i.e. vicinity of the treatment region such as a tumor site.

Susceptibility-based negative contrast in the MRI provides a way to enlarge the effect of a magnetic particle whereas its actual size is much smaller than the MRI's visualization capability. Due to their high magnetic susceptibility, magnetic materials cause an inhomogeneity in the local magnetic field of the MRI to an extent which is much larger than their actual size. The inhomogeneity appears in the T_2^*-weighed gradient echo images in the form of a signal void. This approach presents a method for visualization of microstructures through the susceptibility artifact.

The susceptibility artifact (signal void) was initially characterized through simulation and phantom experiments. The extent of the susceptibility artifact was found to be related to the echo time, static magnetic field, particle's size and saturation magnetization. Depending on the echo time, the extent of the artifact is 75 to 146 times and 72 to 135 times larger than the particle's actual size at a 3.0 T and a 1.5 T magnetic field, respectively.

Micron-sized magnetic particles with high magnetizations within the susceptibility spectrum are categorized as ferromagnetic materials. Due to the remanent magnetization, application of such particles is limited to clinical trials. As the next step, application of micron-sized agglomerations of superparamagnetic nanoparticles as contrast agents in the MRI was studied. Agglomerations can resemble the signal loss behavior of the microparticles in an image. The agglomerations were generated using a T-junction microfluidic chip. An oil-based ferrofluid was applied to generate oil in water droplets. The advantage of using a microfluidic device is the precise control over the size of the droplets as well as their spacing. Microagglomerations of iron-oxide nanoparticles were injected in microchannels of 200 μm and 50 μm in internal diameter respectively. The selected diameters are well in the scale of a large, and a small arteriole. The results showed that agglomerations of 50 μm in diameter are just visible in the images of a fast gradient echo sequence (TrueFISP).

Subsequently, the accuracy of particle positioning using their effect on the images was investigated. The reconstructed images are subject to two types of artifacts in the presence of magnetic materials: geometrical distortion and echo shifting. The former leads to a misregistration of the spins' position while the latter causes a signal loss in the form of a four-leaf-clover on the coronal and sagittal planes and a circle on the transversal plane. The echo shifting generates symmetric signal loss shapes the centers of which can represent the origin of the artifact and thus the position of the particle. On the other hand, the geometrical distortion displaces the center of the artifact and can lead to a miscalculation of the particle's position. It was shown that the echo shifting is the dominant effect over the geometrical distortion. Position of the particles was determined based on their center of gravity. The average error was calculated to be approximately half of a pixel's size. The variation analysis of the results confirmed the reproducibility of the results.

At the next step, a 2D vascular network including an inlet channel branching into eight smaller channels in a three-stage division with an inner diameter of 150 µm at the last level was reconstructed. Microagglomerations of iron oxide nanoparticles (150 ± 20 µm) were injected in a vascular network made of Plexiglas using a micro-milling machine and the high-pressure thermal sealing technique. A fast multi-shot susceptibility sensitive sequence (True-FISP) was used to track the particles as they were injected in the network. The experiment was repeated twice. The first and the second trials yielded 70 and 114 images, respectively. The signal voids were identified visually and positioned through their center of gravity. All the positions were assembled to build up the trajectory of the particles. The results suggested that the technique can be used through a real-time tracking of the magnetic particles to gather images of a blood vessel which is beyond the resolution of the scanner.

In order to expand the approach from a 2D to a 3D representation of the vascular network, we proposed a new algorithm based on a fast multi-shot, multi-slice susceptibility sensitive MR sequence. The technique was validated through phantom studies in a 3D network made of glass. Microagglomerations of iron-oxide nanoparticles were injected in the network and tracked in different imaging slices. The acquisition time per slice was 0.6 s. The reconstruction error was found to be higher in some segments of the vascular network. This was realized to be due to a limitation in decreasing the slice thickness and the loss of signal to noise ratio. The mean measurement error was calculated at ~ 0.4 mm.

In MRN, 3D representation of the particles' trajectories is an important step in identification of the vascular network leading to the tumor site. Due to the limited spatial resolution of the current clinical MR scanners, a precise positioning of the particles is not possible. However, the signal loss artifact in the GRE-based sequences can shed light on how the particles are distributed within the field of view.

In conclusion, this project proposes a new and reliable technique for visualization of human microvessels using a clinical MR scanner and commercial receiver coils. This will be an important step in tumor targeting using the MRN. Real-time tracking of microagglomerations of iron oxide nanoparticles can obtain their movement trajectory. Combination of such trajectories provides a 3D representation of the microvasculatures within the human body, not visible using the current clinical imaging modalities. In-vivo experiments remain as a future work to validate

clinical application of the proposed technique. Map of the local micro vasculature feeding a tumor site in MRN-assisted chemoembolization intervention, leads to a significant improvement on the efficiency of tumor targeting while reducing side effects of chemotherapy, risk of tumor reformation and metastases to the other organs.

TABLE OF CONTENTS

LIST OF TABLES

LIST OF FIGURES

LIST OF SYMBOLS AND ABBREVIATIONS

2D	Two dimensional
3D	Three dimensional
BOLD	Blood oxygenation level independent
b-SSFP	Balanced steady state free precession
COG	Center of gravity
CT	Computerized tomography
CTA	Computerized tomography angiography
DCE	Dynamic contrast enhanced
DSA	Digital subtraction angiography
EPI	Echo planar imaging
FISP	Fast imaging with steady state precession
fMRI	Functional magnetic resonance imaging
FOV	Field of view
FT	Fourier transform
GRE	Gradient Recalled echo
MAR	Motional averaging regime
MION	Monocrystaline iron oxide nanoparticles
MNP	Magnetic nanoparticle
MPIO	Micron-sized iron oxide
MR	Magnetic resonance
MRA	Magnetic resonance angiography
MRI	Magnetic resonance imaging

MRN	Magnetic resonance navigation
MVD	Microvessel density
NMR	Nuclear magnetic resonance
OCA	Optical coherence angiography
OFDI	Optical frequency domain imaging
PCB	Printed circuit board
PMMA	Polymethylmethacrylate
RES	Reticuloendothelial system
RF	Radio frequency
ROI	Region of interest
RTM	Residual transverse magnetization
SDR	Static dephasing regime
SDS	Sodium Dodecyl Sulfate
SE	Spin echo
SENSE	Sensitivity encoding
SMASH	Simultaneous acquisition of spatial harmonics
SNR	Signal to noise ratio
SNR	Signal to noise ratio
SPIO	Superparamagnetic iron oxide
TE	Echo time
TMMC	Therapeutic magnetic micro carriers
TR	Repetition time
USPIO	Ultra small Superparamagnetic iron oxide
VSM	Vibrating sample magnetometer

LIST OF APPENDICES

CHAPTER 1 INTRODUCTION

Cancer is a major chronic disease and a leading cause of mortality in Canada and around the world. Depending on type, number, location and stage of the cancerous tumors, one treatment option or a combination of different type of treatments may be considered. Palliative treatments prevent or slow the development of the cancer cells. In contrast, curative treatments seek to achieve a complete removal of cancer cells.

Surgery is a conventional therapeutic choice for localized and small cancer tumors. It is a curative approach to achieve a complete tumor resection or replacement [1]. It can be used alone or along with a complementary method such as chemotherapy or radiation therapy [2]. It can also be complemented by radiation therapy during the operation.

Radiation therapy uses high-energy radiations such as X-ray, gamma ray or protons to kill cancer cells through damaging their DNA. It can be performed locally or systematically and can be used before or after surgery to enhance or complete the main treatment. Due to the limitation on the radiation dose, this palliative technique is usually performed as a complementary treatment [3, 4].

Chemotherapy is a systemic palliative treatment that uses medicines to kill cancer cells. Medication can be received orally, intravenously or intra-arterially. During chemotherapy, drugs travel throughout the whole body to reach cancer cells. However, healthy cells are inevitably damaged as well. Chemotherapy is often prescribed as a complementary treatment after the surgery or radiation therapy to kill the remaining cancer cells or before the main treatment to shrink the tumors [5, 6].

Chemoembolization is a combination of chemotherapy and embolization procedure mostly used in the liver treatment. In this method drugs are intra arterially injected into the blood vessel supplying the tumor. Subsequently, embolic agents are released to embolize the vessel’s entry and trap the drugs in the tumor by ceasing the blood supply [7, 8]. Accordingly, a highly concentrated dose of therapeutic agents are delivered to the tumor site and the feeding blood vessels are partially occluded to starve the tumor of nutrients.

Targeted therapy is a fairly new type of treatment developed to attack cancer cells with reduced harm to the healthy tissue. In this technique drugs or other substances are applied that interfere with specific molecules involved in either growth or survival of the cancer cells. Targeted therapies are based on interactions with mediators capable of ceasing the development of cancerous tissue. Depending on the type of cancer, targeted therapy can be achieved through interference with the development of angiogenesis, prevention of cell growth signaling, stimulation of the immune system to destroy cancer cells or specific delivery of therapeutic agents to the cancer cells [9-11].

Magnetic resonance navigation (MRN) assisted chemoembolization has been proposed to overcome the drawbacks of older interventions. It has shown a great potential in targeted delivery of magnetic carriers loaded with therapeutic agents [12, 13]. The technique is based on therapeutic magnetic micro carriers (TMMC) which can be steered and tracked using an upgraded magnetic resonance imaging (MRI) system.

TMMC consists of biodegradable microparticles encapsulating magnetic nanoparticles and the antitumor drug. They measure 50 μm in diameter. The external magnetic field of the MRI (B_0) magnetizes the microparticles to saturation. The catheter tip can only be advanced to the level of the arteries. However, the tumor is located at the capillary level. Upon the release of the TMMCs, custom gradient coils are applied to induce a directional propulsion force on nanoparticles, embedded in the micro carriers. This technique leads to the controlled delivery of the therapeutic agents to the region of interest. In vivo targeting of the right or left liver lobes has been successfully achieved by MRN through the hepatic artery in a rabbit model [12]. The steering has been performed through a single bifurcation. However, steering through multiple bifurcations necessitates a precise map of the vasculature leading to the tumor. The gradient coils are applied according to a 3D pre-planned map of the local vasculature feeding the cancer tumor. Consequently, preparation of such a map is an essential step in this intervention. Current clinical imaging modalities are limited in resolving the vasculatures smaller than approximately 200 μm in diameter. As such, the visualization of arterioles and capillaries remain beyond the capability of current clinical imaging modalities.

This research study seeks to develop a clinical imaging technique to identify the vascular path leading to a tumor site with the purpose of improving the MRN technique. The development of such a map leads to steer the TMMCs through multiple bifurcations in the vascular network, enhancing the steering efficiency and reducing the side effects of the anti-cancer medications.

This thesis is presented in the format of an article-based thesis. The rest is organized in eight chapters. Chapter 2 presents a background on MR imaging and a relevant literature review on microvascular imaging. Chapter 3 discusses the assumptions and objectives of the thesis and the overall approach adopted to accomplish each objective. Chapters 4, 5 and 6 are devoted to original contributions of this thesis, corresponding to three articles published or submitted to peer-review journals. Chapter 4 includes the article accepted in March 2013 to be published in the «Journal of Applied Physics». It represents the visualization of microchannels measuring 50 µm in diameter, corresponding to small arterioles, using superparamagnetic iron oxide nanoparticles and a clinical MR scanner. Chapter 5 includes the article accepted in May 2014 for publication in the journal of «Applied Physics Letters» and it represents dynamic tracking of magnetic nanoparticles clusters for mapping microvascular networks. Chapter 6 includes an article on proposing and validating a method for 3D mapping of vascular network through a fast multi-slice multi-acquisition MR sequence. The article was submitted in October 2014 to the Journal of «IEEE Transactions on Biomedical Engineering». Chapter 7 presents a new technique developed for fabrication of an integrated microfluidic device to generate and inject iron oxide microagglomerations in a vascular network. Chapter 8 provides a discussion on all the work carried out during this research study. Finally, the conclusion discusses the contributions of this thesis and new avenues of research and recommendations for future works are also proposed.

CHAPTER 2 LITERATURE REVIEW

2.1 Magnetic resonance navigation (MRN)

Navigation of an untethered device in a living subject is of great interest for both therapeutic and diagnostic purposes. MRN is a newly developed approach to navigate an untethered micro device to a targeted location within the body accessible through the vascular network [14, 15]. The extremity of the catheter injecting therapeutic agents can only be advanced to the arterial level whereas tumors are often located at the capillary level (figure 2-1).

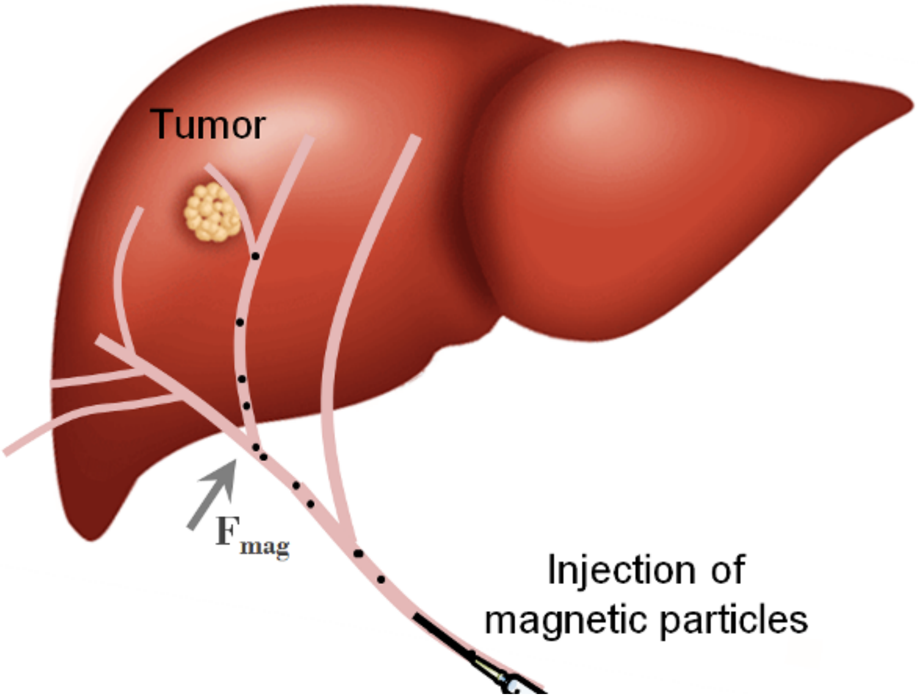

Figure 2-1: Sketch of MRI targeting of a tumor site by applying a magnetic force on volumes loaded with therapeutic agents and magnetic particles.

Therefore, a significant portion of the injected drug reaches the systemic circulation. In MRN, micro carriers loaded with therapeutic agents and magnetic particles are released and subsequently steering gradients are applied to navigate the carriers towards a selected capillary entry where the tumor is located (figure 2-2).

In [16], propulsion of a magnetic core in the carotid artery of a living swine showed feasibility of the technique in-vivo. Three orthogonal gradient coils inside a magnetic resonance imaging (MRI) scanner can induce a three dimensional directional magnetic force on a magnetic object. The magnetic force (F_{mag}) is proportional to the amplitude of the gradient vector and the magnetic moment of the object according to:

$$\vec{F}_{mag} = RV(M \cdot \nabla)B \qquad \text{(Eq. 2-1)}$$

where R is the duty cycle of the gradient, V and $\vec{M}$ are the volume and the magnetization of the magnetic object, respectively, $\vec{B}$ is the magnetic field and ∇ the vector differential operator.

In order to propel a magnetic object in the vascular network, the magnetic force should surmount the drag force applied by the flow. The weight of the magnetic object and its buoyancy can be neglected in small blood vessels since such parameters are smaller than the drag force by several orders of magnitude. Therefore, to achieve a strong magnetic force, magnetization of the magnetic object and the magnetic field gradient generated by the gradient coils should be maximized. In [17], a proportional-integral-derivative controller was used to navigate a ferromagnetic core along a predefined trajectory in real time. Operating inside an MRI system prevents simultaneous application of propulsion and tracking using MR images. Real-time tracking necessitated an alternation between these two processes. An advanced MR sequence based on magnetic signature selective excitation was developed and employed for fast tracking of a single magnetic object [18, 19].

Clinical MRI systems are typically capable of providing tens of mT/m of gradient in any direction. Such gradients are potentially capable of providing enough force to propel a ferromagnetic core, saturated in the magnetic field of an MRI, with a diameter of ~0.6 *mm* [14]. However, gradient amplitudes of several T/m would be required to propel a smaller ferromagnetic core or in smaller vascular networks. Compared to their ferromagnetic counterparts, superparamagnetic particles that are vastly used as contrast agents in MRI hold a significantly smaller magnetization. However, an agglomeration of such nanoparticles can be used as a steerable magnetic volume for therapeutic purposes. Their relative low magnetization should be compensated by application of higher gradient amplitudes.

In [13], therapeutic magnetic micro carriers (TMMC) were guided in real time in a phantom including a single bifurcation using magnetic gradients of 400 mT/m. TMMC were biodegradable microparticles loaded with iron cobalt nanoparticles. These particles possess a high saturation magnetization (72 emu/g) and therefore are an excellent candidate for both imaging and navigation purposes. Subsequently, TMMC particles loaded with doxorubicin were steered in-vivo to the left liver lobes through one bifurcation in a rabbit model using a clinical MR scanner equipped with upgraded gradient coils of 400 mT/m [12, 20]. Results suggested the potential of MRN for improving drug targeting in deep tissues.

In-vivo and in-vitro experiments have been performed to confirm the effectiveness of MRN in targeted drug delivery. Thus far, navigation of micro carriers has been carried out in-vivo through a single bifurcation and in-vitro inside a three bifurcation PMMA phantom [21]. However, the ultimate goal in MRN is to navigate microcarriers in-vivo through a vascular network of multiple bifurcation levels to the entry of a selected capillary. The direction and the time at which the magnetic gradients are applied depend on the local vasculature's map feeding the tumor. As such, preparation of a 3D map of the microvasculature prior to the intervention is a crucial step in MRN.

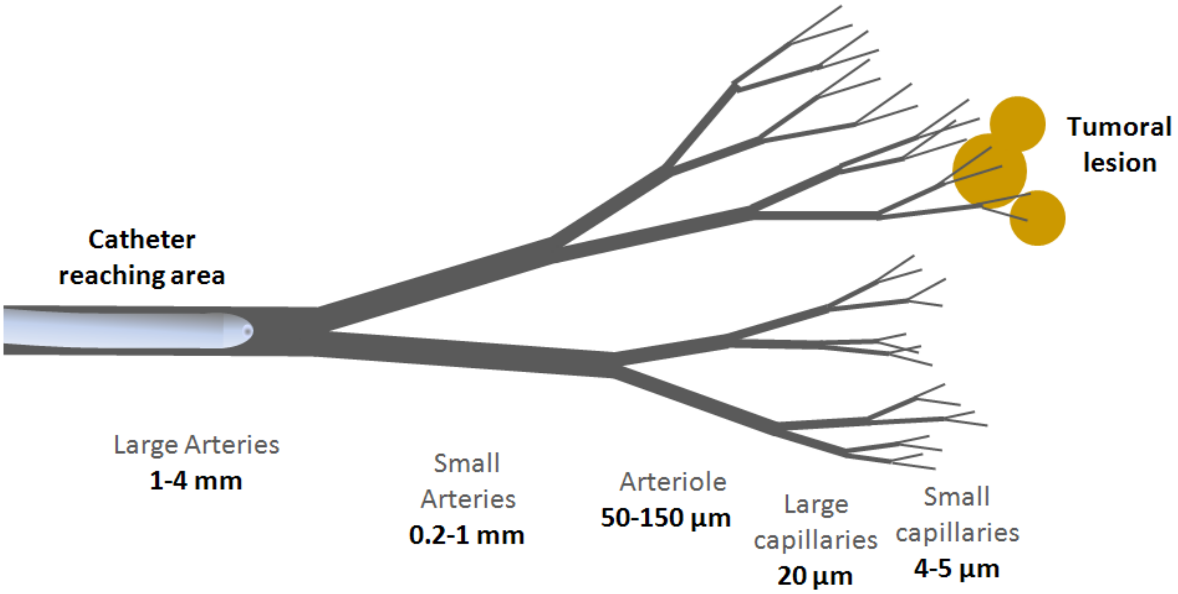

Figure 2-2: A vascular network and relative vessel diameters.

Current clinical angiography modalities can help to provide such a map. In section 2.3, the visualization of the vascular network using current clinical imaging modalities will be discussed.

2.2 Magnetic resonance imaging

MRI uses strong magnetic field and radio frequency waves to generate cross sectional images of internal structures of the body. This technique has profited from technological innovations to improve quality of the images as well as the acquisition speed. Subjected to a large magnetic field (B_0), Hydrogen atoms (protons) become aligned with the direction of the field. By applying a properly tuned radio frequency, protons will be tipped out of alignment with B_0. Upon removal of the radio wave, the protons tend to return to their equilibrium state in a process called relaxation. The relaxation causes variations in transverse magnetization vector that causes a small alteration in the induced electrical current in the receiver coil. The signal is quite sensitive to differences in proton content which is a distinctive characteristic of different types of tissue.

Each MR sequence is a combination of magnetic gradients and radio frequency waves. Frequency encoding gradient encodes nuclear magnetic resonance (NMR) signal spatially by assigning a unique frequency to the spins at different locations along its direction. Therefore, the time-varying NMR signal consists of a range of frequencies, each corresponding to a particular spatial location. The range of frequency precession ($\Delta\omega$) along the x-direction (Δx) where G_x is applied can be calculated according to:

$$\Delta\omega = \frac{\gamma}{2\pi} G_x \Delta x \qquad \text{(Eq. 2-2)}$$

where γ is the gyromagnetic ratio of the protons (42.56 MHz/T). A Fourier transform of the NMR signal reveals the density of spins at each frequency. A frequency-encoding gradient can be applied along any physical direction. It consists of two lobes; prephasing (or dephasing) lobe and readout (or rephasing) lobe. The prephasing lobe prepares the transverse magnetization so that an echo can be formed later in time. In spin echo (SE) sequences, the two lobes are separated by a 180° refocusing pulse. Since the refocusing pulse inverses the accumulated phase during the prephasing lobe, the readout lobe has the same polarity as the prephasing lobe (in order that the spins continue to accumulate phase in the same direction).

Due to the absence of a 180° refocusing pulse, in gradient echo (GRE) sequences the readout lobe is reversed to change the direction of the spin's phase accumulation. The gradient reversal refocuses only the spins dephased by the action of the pre-phasing gradient lobe. Therefore, as opposed to a SE, phase dispersions resulting from magnetic field inhomogeneities, chemical shifts or susceptibility gradients are not cancelled at the center of the GRE (figure 2-3). The time between the application of the radio frequency (RF) excitation pulse and the peak of the echo signal is known as echo time (TE). The time between the successive excitation pulses is known as repetition time (TR).

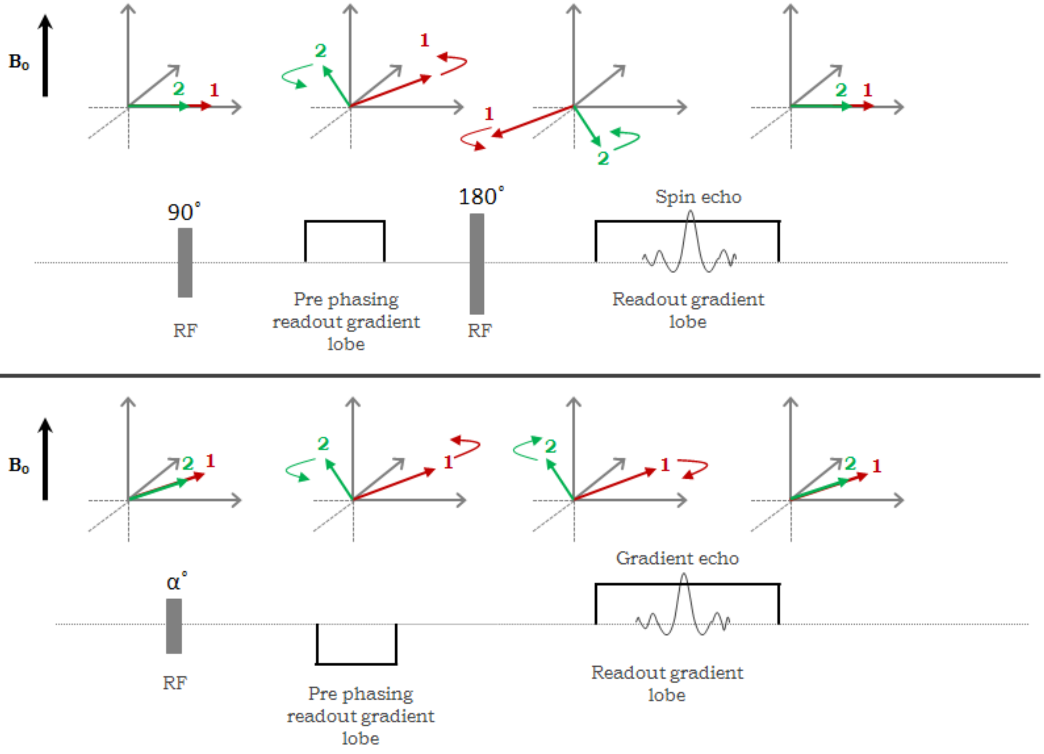

Figure 2-3: Rephasing mechanism in spin echo sequence (top) and gradient echo sequence (bottom) using RF pulses and magnetic gradients.

Peak of the gradient echo occurs when the area under the two opposing lobes is equal. Consequently, GRE images are weighted by a factor of $\exp\left(-TE/T_2^*\right)$ versus $\exp\left(-TE/T_2\right)$ in SE images. The parameter T_2^* is related to the intrinsic relaxation time of the tissue (T_2) by:

$$\frac{1}{T_2^*} = \frac{1}{T_2} + \frac{1}{T_2'} \qquad \text{(Eq. 2-3)}$$

where T'_2 is inversely proportional to the magnetic field inhomogeneity in each image voxel.

In-plane spatial localization necessitates the employment of both frequency and phase encoding gradients. Phase encoding gradient is typically applied orthogonal to the frequency encoding direction. It is applied when the magnetization is in the transverse plane and prior to the application of the readout gradient. The area under the phase encoding gradient varies at each TR to introduce different amount of phase variations to the spins along its direction.

In order to achieve a desired spatial location in a 3D volume, slice selection gradients are applied concurrently with the RF pulses. The slice selection gradient determines the direction perpendicular to the imaging plane (figure 2-4).

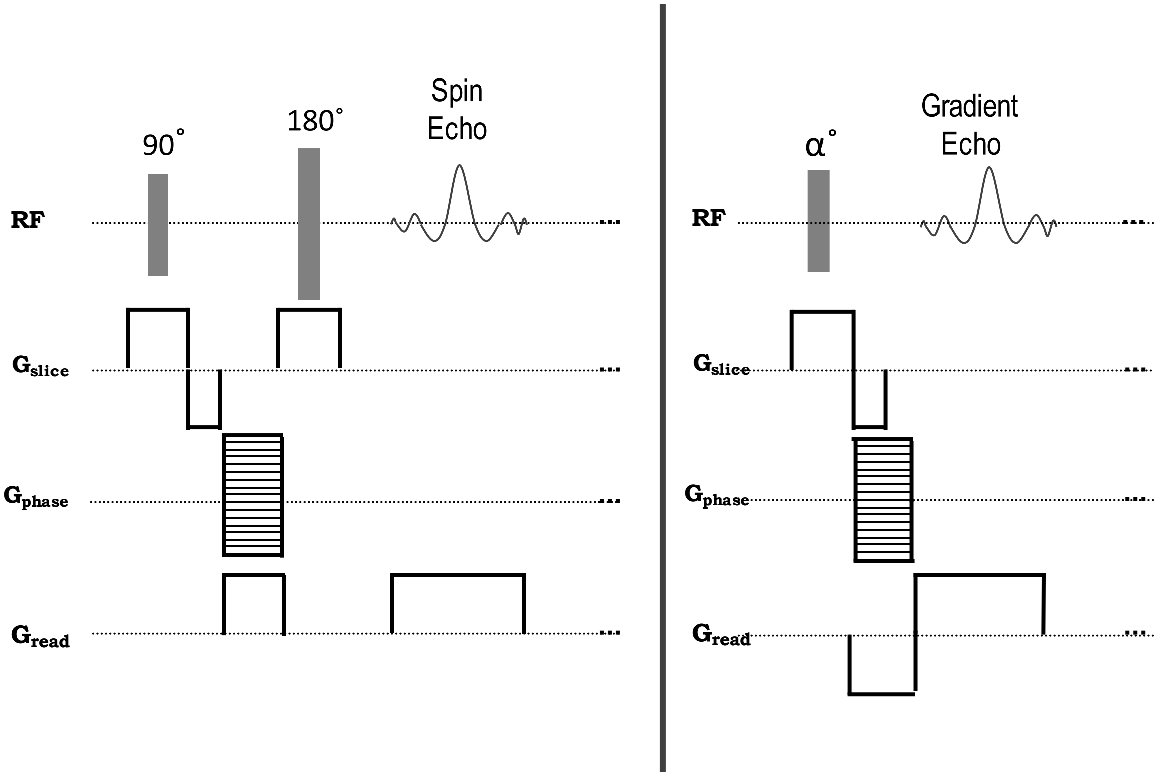

Figure 2-4: Spin echo sequence (left) versus gradient echo sequence (right).

GRE sequences can be fast as no refocusing pulse is present and subsequently no long-lasting T_1 recovery time is required.

2.2.1 Magnetic particles in MRI

Magnetic nanoparticles have been widely investigated in biomedical applications such as hyperthermia, targeted drug delivery and contrast agents in MRI and dual-modality imaging [22-27]. MRI provides an excellent soft tissue contrast whereas its inherent low sensitivity does not convene the visualization of the microstructures. To enhance its sensitivity, contrast agents are applied. Contrast agents are categorized into a) gadolinium-based paramagnetic agents and b) superparamagnetic nanoparticles. Due to a lower magnetization saturation, gadolinium-based contrast agents have a lower sensitivity compared to that of their superparamagnetic counterparts [28]. Free gadolinium ions have a toxic effect that can be nephritic [29, 30]. Iron oxide nanoparticles have shown a superior biocompatibility and biodegradability [31]. Injected iron oxide nanoparticles are cleared through the macrophage process in the reticuloendothelial system and subsequently degraded in the lysosomes.

2.2.1.1 Paramagnetism versus superparamagnetism

Paramagnetism is the characteristic of the atoms or ions with an unpaired number of electrons in their outer shell. As such, these individual atoms or ions possess intrinsic magnetic dipole moments. However, due to the random orientation of the individual magnetic dipole moments, an agglomeration of them does not reveal any magnetization property. Once subjected to an external magnetic field, individual atoms orient along the direction of the magnetic field. Upon removal of the applied magnetic field, all the individual atoms return to their original orientation. Due to thermal agitation, not all the individual paramagnetic atoms can be aligned with the magnetic field unless they are subjected to temperatures of near absolute zero (-273˚C). Gadolinium (Gd^{3+}) is one of the strongest paramagnetic substances widely used as MR contrast agents.

Unlike paramagnetism which is the property of the individual atoms and ions, ferromagnetism is the property of a group of atoms, ions or molecules in a solid crystal. Ferromagnetic materials possess multiple domains with random orientations due to which they do not show any magnetization property. Once subjected to an external magnetic field, all the individual domains orient parallel to the direction of the magnetic field. As opposed to paramagnetic materials, ferromagnetic materials can become fully magnetized at practically obtainable field strengths and room temperatures. Upon removal of the magnetic field, the individual domains maintain their orientation parallel to the magnetic field. This effect is due to the fact that parallel alignment is a preferred low-energy state and thus some energy is required to demagnetize the ferromagnetic materials. It is possible to obtain a single magnetic domain particle by decreasing size of the multi-domain particles to approximately that of the nanometer sized agents. These single-domain nanoparticles are called superparamagnetics having unique magnetic properties. Similar to the ferromagnetic particles, they can become magnetized to saturation even at a low magnetic field and like the paramagnetic particles they will not retain any net magnetization property in the absence of an external magnetic field. The size of the individual magnetic domains depends on the magnetic anisotropy and is in the order of tens of nanometers. A transition from multi domain structure to single domain structure occurs with the reduction of the particles size to ~ 40 nm. This transition is accompanied by a significant reduction in the saturation magnetization [32].

2.2.1.2 Superparamagnetic iron oxide nanoparticles

Superparamagnetic iron oxide (SPIO) contrast agents are based on water insoluble iron oxide crystals of Fe_3O_4 (magnetite) or γ-Fe_2O_3 (maghemite) with a core diameter in the range of 4 - 12 nm. However, the overall diameter of these particles is considerably larger than their core size (5 nm - 1µm). The iron oxide particles are coated with an organic polymer to prevent their aggregation [33, 34]. The principal effect of the SPIOs is on the T_2^* relaxation time. MR imaging of such nanoparticles is usually performed using the T_2^*/T_2-weighted imaging sequences. The T_1 relaxation time is also affected by the SPIOs enabling the T_1-weighted imaging with a less pronounced positive T_1- contrast [35]. Depending on the distribution of the particles' size and their overall diameter, iron oxide contrast agents are divided into three groups; a) standard SPIO agents, ultra small SPIOs (USPIO) and monocrystalline iron oxide nanoparticles (MION). Several parameters, such as size and coating and concentration of the particles within an imaging voxel, affect the relaxometric behavior of the SPIOs.

Standard SPIOs have a high T_2/T_1 relativity ratio and their overall size varies in the range of 60 -150 nm. They are composed of agglomerated iron oxide cores and in the presence of a magnetic field can get separated from the solution. Intravenously injected SPIOs are easily sequestered by the reticuloendothelial system (RES) cells in the liver, spleen and bone marrow (half-life, 3 days) [36].

The USPIOs have a smaller hydrodynamic diameter (10 – 50 nm) and a longer half-life. Owing to their small size, Brownian motion keeps them suspended in water in spite of their higher density. These agents can cross the capillary wall and spread to the tissue. Due to their long blood half-life, they can be used as blood pool contrast agents in the MR angiography [37, 38].

The MIONs are very small in size (2 – 9 nm) and are usually used for receptor-directed and magnetically labeled cell probe MR imaging [39, 40]. Their core contains one central Iron oxide particle only and due to their small size they easily pass through the capillary endothelium.

Contrast agents are used to enhance the sensitivity of the MRI through shortening the T_1 and T_2 relaxation times. The efficiency of a contrast agent is evaluated by the relaxivity (r_1, r_2 and r_2^*, inverse T_1, T_2 and T_2^* respectively). R_2^* relaxivity indicates an increase in the T_2 relaxation time in the GRE sequences due to a magnetic inhomogeneity called the susceptibility effect:

$$R_2^* = R_2 + \gamma B_s \qquad \text{(Eq. 2-4)}$$

where γB_s represents the relaxation induced by the magnetic inhomogeneity. The term susceptibility effect describes an increase in the T_2/T_2^* relaxation rates due to a difference in magnetization within a voxel. Non-homogeneous distribution of magnetic particles induces a local field gradient which causes the spins to lose coherence at an accelerating rate. The susceptibility-induced relaxation can affect the protons located much farther from the magnetic cores. On the other hand, a homogeneous or dispersed distribution of the magnetic particles results in another contrast mechanism where because of a free water access to the contrast agent sites, the proton relaxation is due to an interaction between each of the individual magnetic particles and water molecules (figure 2-5).

Two SPIO-based contrast agents are clinically approved: ferumoxides (Feridex in the USA, Endorem in Europe, diameter of 120 to 180 nm) and ferucarbotran (Resovist, diameter of 60 nm).

2.2.1.3 Clusters of magnetic nanoparticles

An assembly of magnetic nanoparticles can be used to further enhance the contrast. Agglomerations of magnetic nanoparticles significantly affect the transverse magnetization [27]. It was shown that the sensitivity of MRI is comparable to the one of PET in detecting single cells using an assembly of SPIO nanoparticles [41].

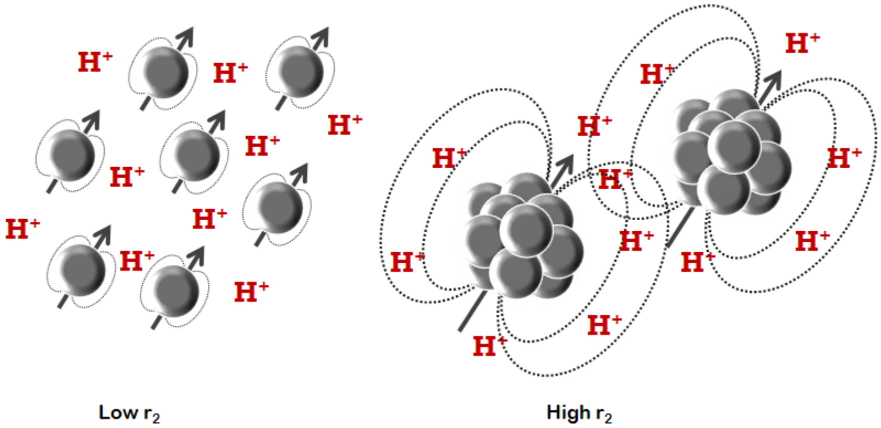

Figure 2-5: Dispersed distribution of magnetic particles compared to clusters of magnetic particles.

The R_2 relaxivity rate increases with the agglomeration's size, reaches a maximum and decreases subsequently. On the other hand, the r_1 relaxivity is only slightly affected by the size of the agglomerations [42-45]. Compared to the large agglomerations of the magnetic nanoparticles, free magnetic particles show a different contrast mechanism. Since diffusion of the magnetic particles is dependent on their size, different mechanisms can be defined based on the translation diffusion time around the nanoparticles agglomerations. The diffusion time is defined as:

$$\tau_D = \frac{r^2}{D} \qquad \text{(Eq. 2-5)}$$

where r is the radius of the nanoparticles or the agglomerations, and D is the diffusion coefficient of the water molecules. The diffusion time is the time for a water molecule to pass a hemisphere of a nanoparticle or an agglomeration.

There are two spin dephasing regimes: the motional averaging regime (MAR) where the water diffusion is the main factor in spin dephasing and the static dephasing regime (SDR) where the relaxation rate is independent of diffusion. For short diffusion times ($\tau_D << 1/\Delta w_r$ where Δw_r is the difference in the angular frequency experienced by a proton between the local fields) the particles are homogeneously dispersed in the solution. In MAR, the diffusion time is much smaller than the echo time and no difference is observed between the r_2 and r_2^* relaxation rates (figure 2-6). The r_2 and r_2^* increase as does the particle size [43, 46, 47].

In SDR, where $\tau_D > 1/\Delta w_r$, randomly distributed large agglomerations create an inhomogeneous magnetic field. If the particles or the size of the agglomerations are large enough, compared to the inter-particle distance, the diffusion of water is small and as such, it can be ignored. In this regime, r_2 decreases with particles' size and r_2^* reaches a constant value (figure 2-6) [43, 47]. The r_2 relaxivity tends to decrease in SDR regime due to the fact that the RF refocusing pulse becomes effective in rephasing the spins. Trend of the r_2/ r_2^* relaxivity changes according to the regime where the particles are in.

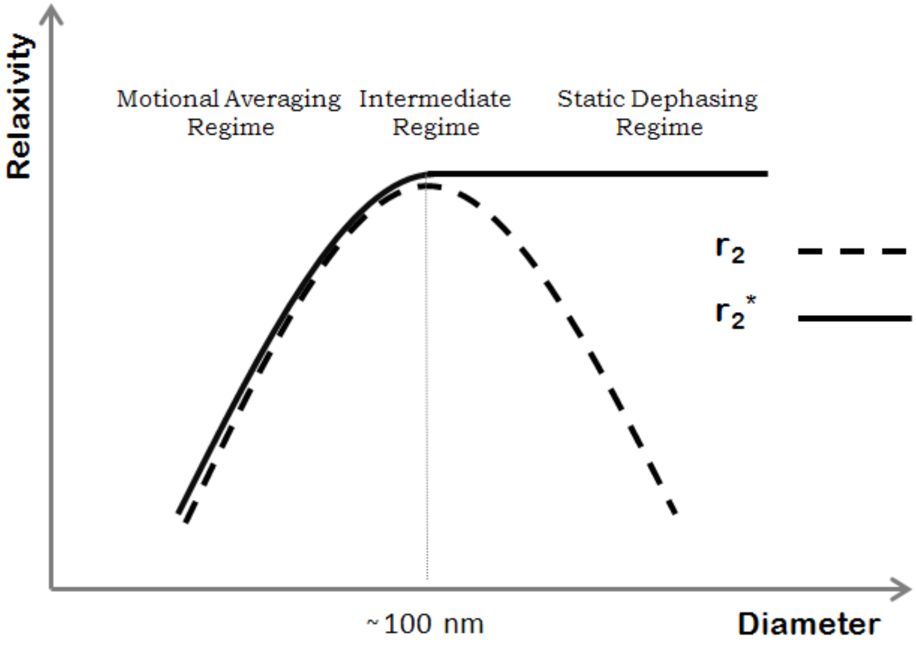

Figure 2-6: Sketch of the transverse relaxivity as a function of nanoparticle's diameter in different dephasing regimes. This curve is a representative sketch of the curve shown in Ref. [27, 43, 45].

Beyond the SDR, the induced magnetic field created by the magnetic particles is so strong that the adjacent protons are completely dephased. Accordingly, the surrounding water protons do not contribute to the MR signal [27]. Nanoparticle clusters and spherical-shaped particles demonstrate the same relaxivity behavior as their size varies. It was shown that nanoparticle cluster size was linearly related to the r_2 of clusters in the MAR [44], and inversely related to the r_2 of clusters in the SDR [48].

2.2.2 Susceptibility contrast in MR images

In this section, the susceptibility effect in MR images with a focus on the presence of magnetic particles in the region of interest is explained. According to the imaging sequence two types of artifacts (geometrical and intensity distortion) can occur in the images that are explained in details.

2.2.2.1 Susceptibility

A one to one relationship between a spin's position and the frequency at which it precesses is the basis of the spatial encoding in the MRI. An inhomogeneity in B_0 causes a variation in the precession frequency creating susceptibility artifacts in the MR images. Magnetic susceptibility is a dimensionless quantitative measure of the level of a material's ability to induce a local magnetic field inhomogeneity within an applied homogeneous magnetic field. Macroscopic field inhomogeneities give rise to two types of artifacts: geometrical distortion and intensity distortion (echo shifting). The first artifact causes a misregistration of the spin's location in the form of a shift in spins' position or a "shearing" effect on the image, depending on whether the background gradient is parallel or perpendicular to the read-out direction. The second artifact only affects the gradient echo imaging.

2.2.2.1.1 Geometrical distortion

If a background gradient (G'_x), parallel to the read-out gradient's (G_x) direction, is present during the echo acquisition, the phase evolution of the spins alters [49]:

$$\phi(t') = -2\pi\gamma\left(G_x x + G'_x x\right)t' \qquad \text{(Eq. 2-6)}$$

$$\phi(t') = -2\pi\gamma G_x t' x\left(1 + \frac{G'_x}{G_x}\right)t' \qquad \text{(Eq. 2-7)}$$

It is assumed that the read-out gradient is applied along the x-direction. As such, the spins residing at position x will be mapped to an apparent position x' and the reconstructed spin density spatially differs from the physical spin density:

$$x' = x\left(1 + \frac{G'_x}{G_x}\right) \qquad \text{(Eq. 2-8)}$$

The presence of the G'_x causes the spins to be shifted parallel to the read-out direction. Increasing the applied read-out gradient is the only way to minimize the distortion. If G'_x is known throughout the FOV, the distortion can be corrected through shimming.

Any background gradient during data recording will change the frequency at which the spins precess and lead to a misregistration of the spins' location. If G' is perpendicular to the read-out direction (G'_y or G'_z), the spins will be shifted along the x-direction as a function of their position in the z or y-direction. If the background gradient is in the y-direction, the phase behavior during the read-out varies as following:

$$\phi(t') = -2\pi\gamma\left(G_x x + G'_y\, y\right)t' \qquad \text{(Eq. 2-9)}$$

$$\phi(t') = -2\pi\gamma G_x\left(x + \frac{G'_y}{G_x}y\right)t' \qquad \text{(Eq. 2-10)}$$

$$x' = x + \frac{G'_y}{G_x}y \qquad \text{(Eq. 2-11)}$$

This effect distorts the square shape of the voxel and as a result the reconstructed voxels contain information from the adjacent spatial locations.

2.2.2.1.2 Intensity distortion

Due to the absence of the 180° refocusing pulse, intensity distortion pertains to the gradient echo sequences. In 2D Fourier transform (FT) the MR signal is given by [50, 51]:

$$s(n,m) = \int_{-\infty}^{\infty}\int_{-\infty}^{\infty}\int_{-\infty}^{\infty} M(x,y,z)e^{i\phi(x,y,z,n.m)}dxdydz \qquad \text{(Eq. 2-12)}$$

where n and m represent number of the time sample and that of the phase encoding step, respectively, and M represents the distribution of the magnetization right after the application of the RF excitation pulse.

In the absence of a background gradient with slice selection along z, phase encoding along y and frequency encoding along the x direction, phase evolution during the sampling period is given by [50, 51]:

$$\phi(x,y,z) = \gamma x G_x n\Delta t + \gamma y m \Delta G_y T_y \qquad \text{(Eq. 2-13)}$$

where Δt is the sampling interval, ΔG_y is the step size of the phase encoding and T_y is the duration of the phase encoding gradient.

The presence of field inhomogeneities perturbs the evolution of the phase in both SE and GRE sequences [50, 51]:

$$\phi'_{SE}(x,y,z) = \phi(x,y,z) + \gamma \Delta B(x,y,z) n\Delta t \qquad \text{(Eq. 2-14)}$$

$$\phi'_{GRE}(x,y,z) = \phi(x,y,z) + \gamma \Delta B(x,y,z) n\Delta t + \gamma TE \Delta B(x,y,z) \qquad \text{(Eq. 2-15)}$$

Here, ϕ' and ϕ indicate the perturbed and the unperturbed phase evolutions, respectively, and $\Delta B(x,y,z)$ indicates the induced inhomogeneity in B_0. The first added term ($\gamma \Delta B(x,y,z) n\Delta t$) causes a geometrical distortion in both the SE and GRE sequences. The term $\gamma TE \Delta B(x,y,z)$ occurs in GRE sequences only and it leads to a temporal shift in the echo during the signal acquisition period. Figure 2-7, illustrates how a background gradient shifts the echo to left or right within the sampling window. Peak of the gradient echo arises when the area under the two opposing read-out lobes is equal. A negative or a positive gradient during the application of the read-out gradients causes the gradient echo to take place later or earlier in time. As such, a loss of signal occurs in the voxels where the background gradient is present.

Background gradients in the slice-selection direction cause a shift in the origin of the k-space and therefore, the signal can be reduced significantly [52]. Although this effect can occur in both the SE and GRE images, the magnitude of the shift is greater in the GRE.

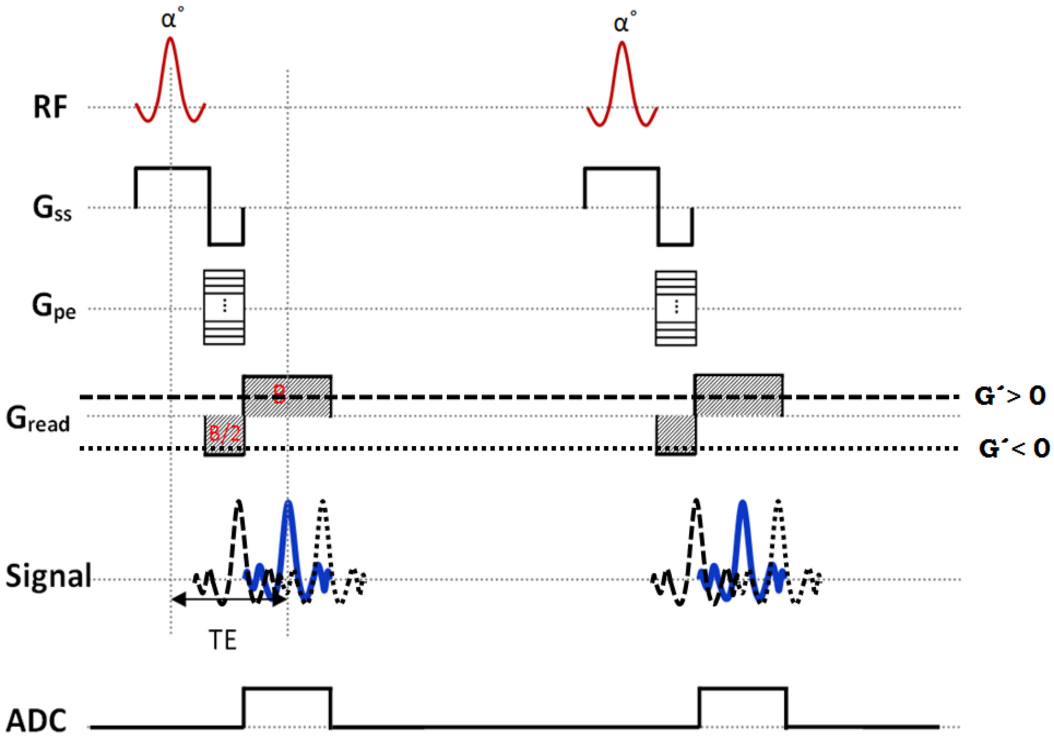

Figure 2-7: Effects of negative and positive background gradients during data acquisition on echo shifting in GRE-based sequences.

2.2.2.2 Magnetic particles in external fields

Ferromagnetic materials have a rather high susceptibility. A magnetic sphere of radius *a* and constant susceptibility surrounded by uniform space and subjected to a uniform magnetic field, such as B_0 creates a magnetic field corresponding to the field of a magnetic dipole given by [68]:

$$\vec{B}(\vec{r}) = B_0\hat{z} + \frac{\mu_0}{4\pi}\left(3\frac{(\vec{m}.\vec{r})\hat{r}}{r^5} - \frac{\vec{m}}{r^3}\right) \qquad \text{(Eq. 2-16)}$$

where $\mu_o = 4\pi \times 10^{-7}$ is the permeability of the free space, $\hat{r}$ is the *r*-directional unit vector, $\hat{z}$ is the unit vector in *z*-direction, B_0 is the external uniform magnetic field and $\vec{m}$ is the magnetic dipole moment calculated by:

$$\vec{m} = \frac{4}{3}\pi a^3 \vec{M}_{sat}\hat{z} \qquad \text{(Eq. 2-17)}$$

where $\vec{M}_{sat}$ and a correspond to the saturation magnetization and the radius of the sphere, respectively (figure 2-8).

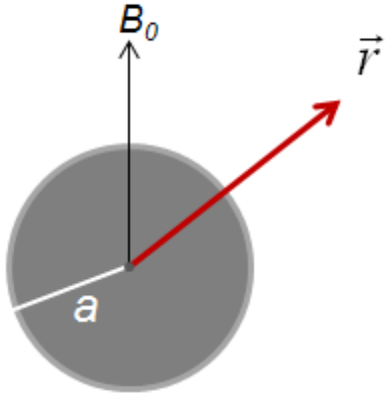

Figure 2-8: Presentation of magnetic field at position $\vec{r}$ outside of a magnetic sphere with radius a.

In the continuous boundary condition across the spherical sphere, change in the z-component of the magnetic field is (figure 2-9):

$$\Delta B_z = \frac{\mu_0}{4\pi}\left(3\frac{(\vec{m}.\vec{r})\hat{r}}{r^5} - \frac{\vec{m}}{r^3}\right) \qquad \text{(Eq. 2-18)}$$

The magnetic field introduces an inhomogeneity in the homogenous magnetic field of MRI. The inhomogeneity affects the MR signal by adding an additional phase term [49, 53]:

$$\Delta\phi = \gamma TE \Delta B_z \qquad \text{(Eq. 2-19)}$$

The phase term varies linearly with TE and is proportional to the induced magnetic field.

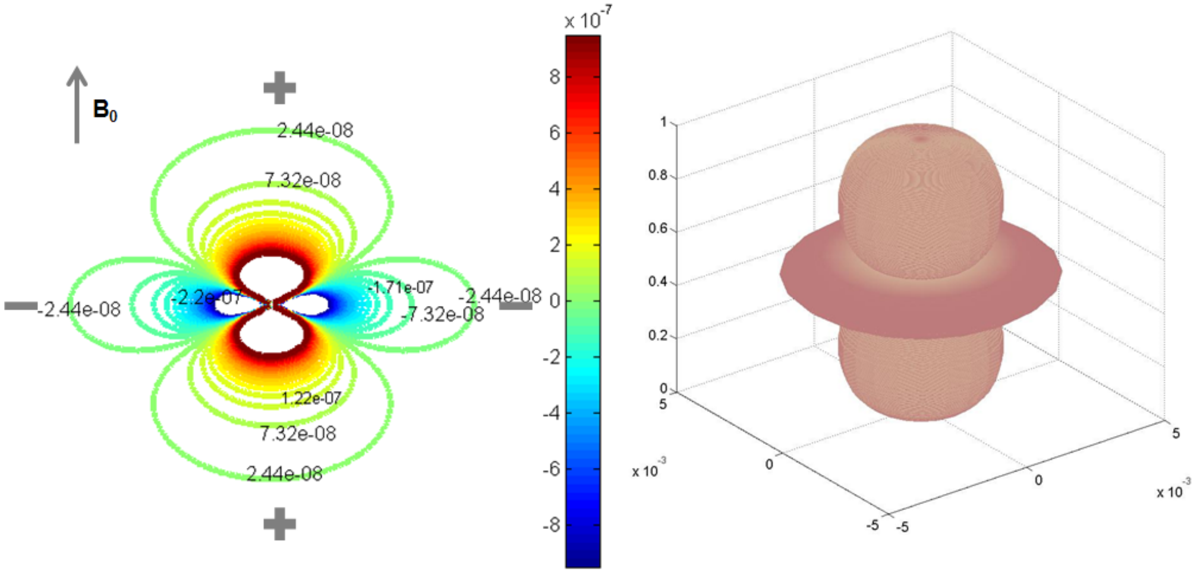

Figure 2-9: Simulated magnetic field lines (in Tesla) (left) and the dephased volume caused by a magnetic particle (see Equations. 2-18 and 2-19) (right).

As described in section 2.2.2.1.2, a magnetic gradient introduces an intensity distortion in the GRE images in the form of a signal loss. The time-dependent modification to the MR signal (*S*) caused by a magnetic particle is hence proportional to an integral over the precessing proton density within the volume of interest:

$$s = \int \rho(x, y, z) e^{-i\Delta\varphi} dz \qquad \text{(Eq. 2-20)}$$

The above equation can be used to simulate the signal loss artifact in the GRE images. It also allows studying the effects of TE and properties of the magnetic particle on the extent of the signal loss. However, the equation addresses the signal loss due to echo shifting effect only. Several studies have been conducted on the simulation of signal loss artifact in different MR sequences [50, 51, 54-59]. In [60], GRE imaging of individual magnetic particles was numerically simulated. A theoretical single-voxel was simulated a) based on both the geometrical distortion and the echo shifting and b) based on the echo shifting only (figure 2-10). The results showed a significant difference in the form and the extent of the simulated signals in the high resolution images (<100 µm). However, for image resolutions of more than 200 µm, no significant deviation was observed in the simulated signals. The results implied that the intensity distortion is the dominant effect over the geometrical distortion in the susceptibility-based artifacts in GRE sequences.

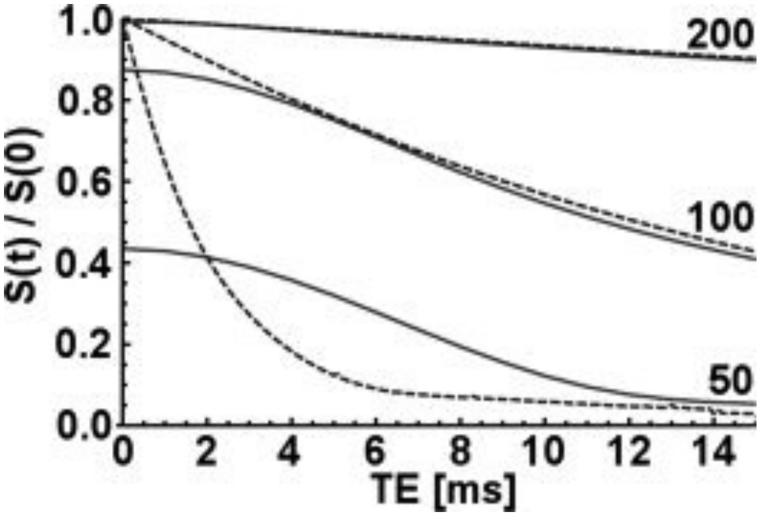

Figure 2-10: Reproduced from [60]. Comparison of voxel signals with and without geometrical distortion correction. Solid curves are numerical simulations including geometrical and intensity distortions. Dashed curves include only intensity distortion. Curve labels show image resolution in micrometers.

2.2.3 Real-time MR imaging techniques

Real-time resonance imaging refers to the continuous tracking of a moving organ or object within the FOV. It finds application in cardiovascular imaging, functional studies of joint kinetics, noninvasive monitoring of intervention procedures or contrast agents. In this section, GRE-based fast MR techniques are discussed.

2.2.3.1 Echo planar imaging

Echo planar imaging (EPI) is one of the fastest imaging sequences which find an application in dynamic studies and real time imaging such as diffusion imaging, perfusion imaging, cardiac imaging and neurofunctional brain mapping. In EPI a train of gradient echoes is produced in each TR. Each echo fills one k-space line. In a single-shot EPI all the k-space lines are filled during one TR. Following the excitation pulse and before the transverse magnetization decays away completely, a bipolar oscillating read-out gradient is applied to generate an echo train. Each gradient echo is then phase-encoded individually so that multiple k–space lines can be filled in a single excitation.

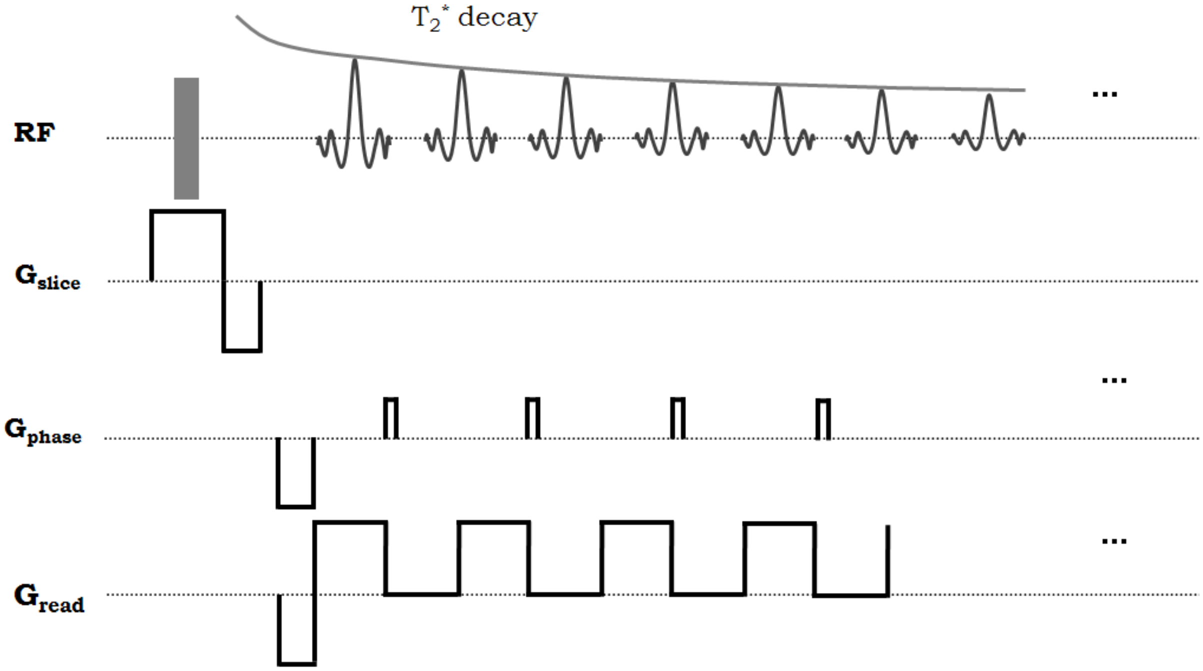

Figure 2-11: Gradient echo EPI acquisition.

The reversal of the readout gradient reverses the k-space trajectory for every other gradient echo. This effect should be corrected prior to reconstruction of the image. In gradient EPI, each k-space line is filled with a gradient echo acquired at a different TE the amplitude of which decays according to:

$$S(n) = S_0 e^{-TE(n)/T_2^*} \qquad \text{(Eq. 2-21)}$$

The TE corresponding to the central k-space line is known as the effective TE (TE_{eff}) and determines the image contrast. Position of the k-space central line can be controlled by the phase-encoding gradients. Single-shot EPI has an excellent temporal resolution (~ 100 ms) at the cost of low signal to noise ratio (SNR), a low spatial resolution and distinct artifacts.

Reduction of the acquisition time in EPI sequences has been carried out by decreasing the echo train time through either reducing the number of echoes or applying a faster gradient. These techniques are known as parallel imaging, partial Fourier, sparse sampling and gradient ramp sampling.

The speed of data acquisition depends on the speed of gradient encoding, which is controlled mainly by the switching rate of the gradient fields. Despite recent improvements in performance of the encoding gradients to satisfy the need for fast imaging, the switching rate is limited by neural stimulation in the patients. In order to solve this problem, alternative encoding methods such as parallel imaging have been proposed.

Parallel imaging is a technique developed for faster imaging, based on phased array coils. Multiple surface coils each having an intrinsic spatial sensitivity are used in this technique. The influence of the coil sensitivity is regarded as an encoding effect analogous to gradient encoding. The number of phase encoding steps is reduced by increasing the readout lines spacing. Reduction in the phase encoding steps results in a reduction in the field of view (FOV) and consequently the so-called aliasing (wrapping) effect. In the presence of one receiver coil the aliasing effect is irreversible. However, applying the multiple-coil acquisition approach allows for reconstruction of the FOV without the aliasing artifact. There are two main methods to remove aliasing in parallel imaging; sensitivity encoding (SENSE) [61] and simultaneous acquisition of spatial harmonics (SMASH) [62].

Depending on local coil sensitivities, aliasing occurs with different weighting in each individual image. In SENSE, to reconstruct an unfolded image, the images obtained from all coils are combined using coil sensitivity maps. The acquisition time is reduced by a factor known as the reduction factor that is determined by the number of k-space lines being reduced. Due to the coil sensitivities, the spatial weighting of the MR signal is analogous to the spatial weighting provided by the sinusoidal Fourier encoding functions. In SMASH, the linear combination of the coil sensitivities approximates the sinusoidal functions corresponding to the missing k-space phase-encoding lines.

EPI suffers from two major sources of artifacts; Nyquist ghosts and geometric distortions. As mentioned earlier, direction of the k-space lines for odd echoes is opposite to that of the even echoes, requiring correction prior to the Fourier reconstruction. To this end, the k-space data are time-reversed along the readout direction for the alternative k-space lines. This reversal results in an inconsistent phase accumulation in odd and even k-space lines ($\exp\left(\left(-1\right)^n i\varphi\right)$), which in the spatial domain causes a displacement of signal intensity halfway across the image in the phase encoding direction. A common way to correct this displacement is to acquire an EPI image, called calibration scan, while the phase encoding gradients are off. One dimensional Fourier transform of the k_y line determines the offset of the echo center for each k_y line [63, 64]. However, if a local B_0 inhomogeneity varies along the phase-encoding axis, the correction method becomes inadequate.

Presence of background inhomogeneity leads to misregistration of the spins in the images known as geometrical distortion. The degree to which spin positions are distorted is directly proportional to the intensity of the field inhomogeneity and inversely proportional to the magnitude of the encoding gradient. Due to the use of a series of blips with a very low bandwidth and magnitude in the phase encoding direction (figure 2-11), a considerable image distortion is observed in this direction in the EPI images. In addition, the presence of a field inhomogeneity, such as a magnetic particle, severely deteriorates the geometrical distortion.

Despite the excellent temporal resolution of the EPI scans which makes real-time and dynamic imaging feasible in many applications, the sequence is not efficient when there is a strong source of magnetic susceptibility in the FOV such as a magnetic particle.

2.2.3.2 Steady state imaging

Steady state is a condition in the GRE sequences achieved through the application of repetition times shorter than T_1 and T_2 of the tissue. As such, the value of the longitudinal magnetization at the corresponding points in adjacent TR intervals is equal. Since the TR is very short, there is not enough time for T_1 and T_2 to naturally decay. Therefore, both the longitudinal and the transversal magnetizations coexist. The transversal magnetization remaining at the end of each TR is called the residual transverse magnetization (RTM). Steady state sequences can be classified into two main categories based on the state of the RTM; whether it reaches zero (spoiled) or a non-zero steady value (steady state free precession) before the application of the next excitation pulse.

In order to remove the RTM, spoiler gradients may be applied at the end of the pulse sequence. Spoiler gradients dephase the transverse magnetization along the direction they are applied whereas the longitudinal magnetization experiences no effect. RF spoiling is another technique used to spoil the RTM. During this process a phase variant (Φ_j) excitation pulse is applied at each TR. The phases can vary randomly or according to a phase-cycling schedule such as

$\Phi_j = \Phi_{j-1} + j\Phi_0$ [65]. Therefore, the RTM has random phase at each TR and the phases do not accumulate to build up a residual magnetization.

According to the Bloch equations, the longitudinal magnetization at the end of the *j*th TR is:

$$Mz_j = Mz_{j-1} cos\theta e^{-TR/T_1} + M_0\left(1 - e^{-TR/T_1}\right) \qquad \text{(Eq. 2-22)}$$

Once the steady state condition is reached where;

$$Mz_j = Mz_{j-1} = Mz \qquad \text{(Eq. 2-23)}$$

The steady state longitudinal magnetization becomes equal to:

$$Mz = \frac{M_0\left(1 - e^{-TR/T_1}\right)}{\left(1 - cos\theta e^{-TR/T_1}\right)} \qquad \text{(Eq. 2-24)}$$

Rephasing of the FID at an echo time TE ($M_z Sin\theta e^{-TE/T_2^*}$) produces a signal in a spoiled GRE acquisition:

$$S_{spoil} = \frac{M_0 sin\theta\left(1 - e^{-TR/T_1}\right)}{\left(1 - cos\theta e^{-TR/T_1}\right)} e^{-TE/T_2^*} \qquad \text{(Eq. 2-25)}$$

S_{spoil} defines how the longitudinal magnetization responds to the first RF excitation pulse. If the longitudinal magnetization experiences *j* excitations ($j \geq 1$) the steady state expression for the spoiled GRE is:

$$S_j = M_0 sin\theta\left[\frac{Mz}{M_0} + \left(1 - \frac{Mz}{M_0}\right)\left(cos\theta e^{-TR/T_1}\right)^{j-1}\right] e^{-TE/T_2^*} \qquad \text{(Eq. 2-26)}$$

MRI sequences that are based on the steady-state free precession extract the FID either immediately after the RF; the echo signal preceding the next RF pulse or a coherent sum of both signals. Therefore, SSFP signal can be categorized to SSFP-FID and SSFP-echo (figure 2-12). To avoid spoiling the RTM, excitation pulses should have the same phase in the rotating frame and the transverse magnetization should also accumulate equal phases at each TR interval. The latter condition is attained when the gradient areas are identical at all TR intervals.

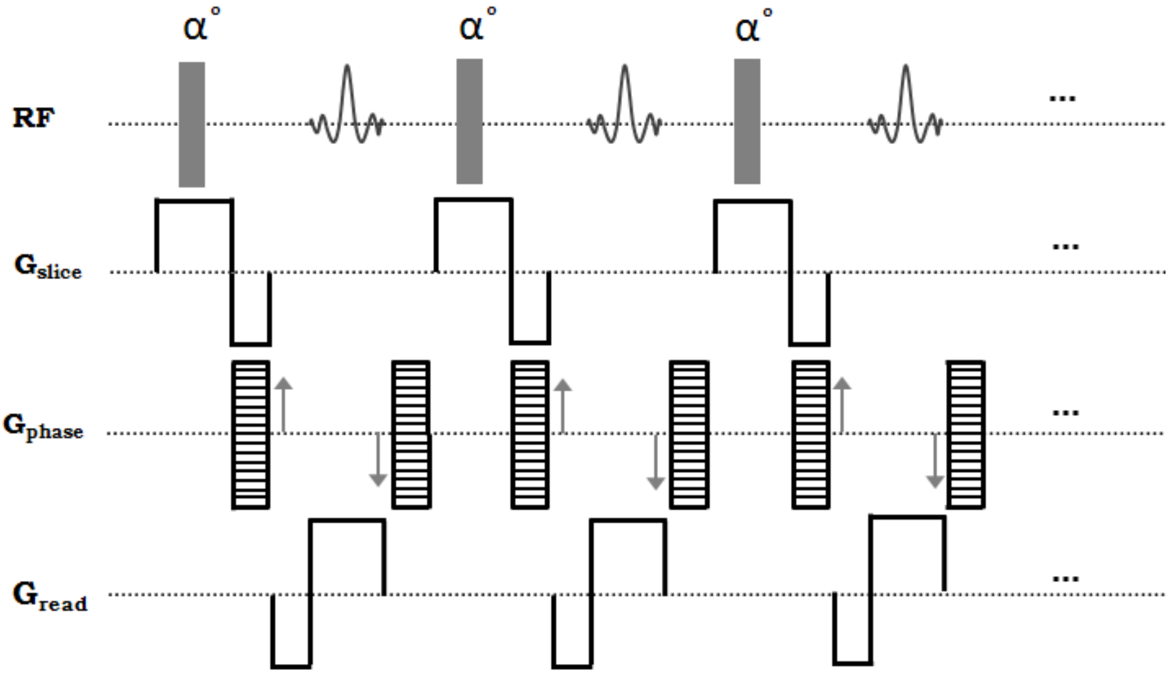

Figure 2-12: Steady-state gradient echo (SSFP-FID) sequence

If during each TR the total gradient area on all three axes is zero another form of steady state is reached where both the FID and the Echo signals superpose (balanced SSFP or True-FISP). The balanced gradients refocus both signals at the center of the TR interval as a single echo (figure 2-13).

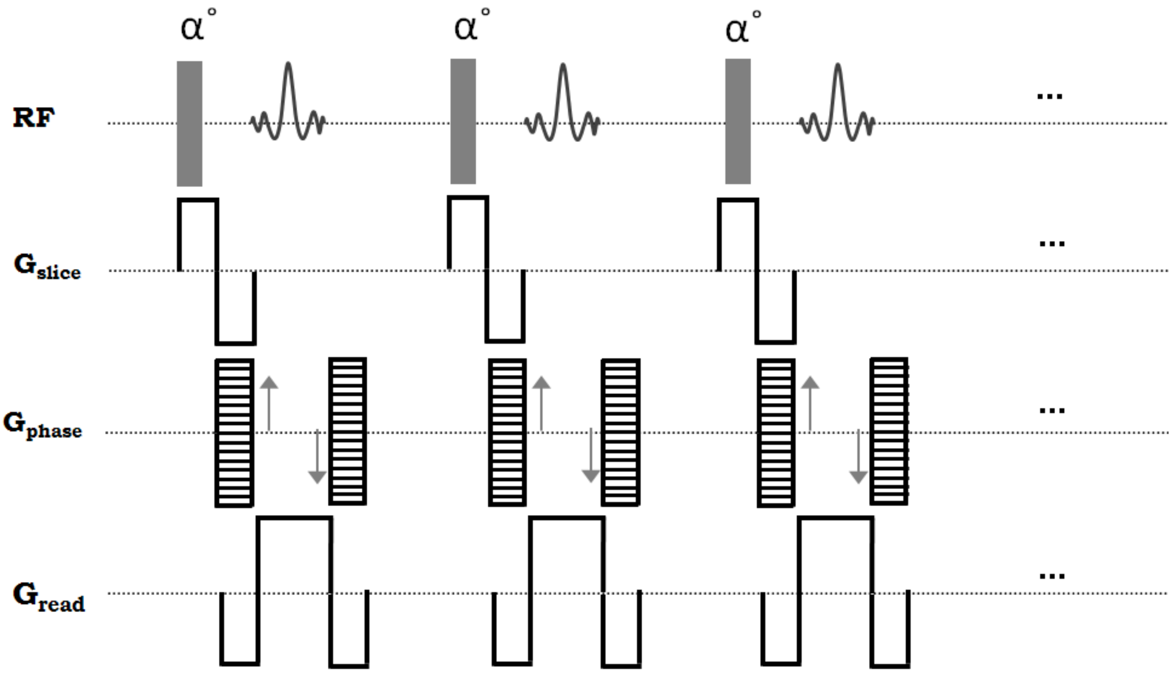

Figure 2-13: Balanced SSFP sequence.

The signal intensity for the balanced sequence is given by [66]:

$$S = M_0 \frac{\left(1 - e^{-TR/T_1}\right)\sin\alpha}{\left(1 - e^{-TR/T_1}\right)\cos\alpha - \left(e^{-TR/T_2}\right)\left(e^{-TR/T_1} - \cos\alpha\right)} e^{-TE/T_2*} \qquad \text{(Eq. 2-27)}$$

Where M_0 is the magnetization at equilibrium and α is the flip angle. In steady state, TR is nearly always much shorter than T_1 or T_2, consequently the equation reduces to:

$$S = M_0 \frac{\sin\alpha}{1 + \cos\alpha + (1 - \cos\alpha)(T_1/T_2)} e^{-TE/T_2} \qquad \text{(Eq. 2-28)}$$

When a signal is recorded at TE ≈ TR/2, in the final term T_2^*will be replaced by T_2. In [67], it was shown that a complete refocusing occurs at TE = TR/2. Therefore, once TE is set at TR/2, the steady state signal is weighted by $e^{-TE/T2}$ whereas other GRE sequences are weighted by $e^{-TE/T2*}$. According to Eq. 2-28, balanced SSFP has a T_2/T_1 contrast weighing. Tissues with equal T_1 and T_2 relaxation times (fluids and fat) produce a hyperintense signal and appear bright in the images. Table 2-1 shows the commercial names of steady state pulse sequences used by MR scanner vendors.

Table 2-1: Commercial names of steady state pulse sequences used by MR scanner vendors

Vendor	Spoiled GRE	SSFP-FID	SSFP-Echo	Balanced SSFF
Siemens	FLASH	FISP	PSIF	True FISP
General Electric	SPGR	GRASS	SSFP	FIESTA
Philips	T_1-FFE	FFE	T_2-FFE	Balanced FFE

2.3 Vascular imaging

Several techniques have been developed to visualize vascular networks. These techniques differ in accuracy, penetration depth, acquisition time, computational effort and provided information. A variety of visualization techniques including contrast-enhanced computerized tomography (CT) or MRI and post-processing analysis such as volume and surface rendering has been developed to display vascular structures and their surroundings more clearly. In this section, different angiography techniques and their ability in resolving microvasculatures are discussed.

2.3.1 Imaging modalities in angiography

The need to understand the vascular anatomy of a tissue has led to development of different imaging techniques helping to visualize small blood vessels in a 3D fashion. Digital subtraction angiography (DSA) is considered the reference imaging modality in the visualization of the vascular network, evaluation of intracranial aneurysm and analysis of the stenosis in arteries [68-71]. DSA provides a resolution of ~180 μm. However, the approach involves invasive intra-arterial insertion of a catheter and an iodinated contrast agent that is potentially nephrotoxic. On the other hand, the contrast level of the intravenously injected iodine drops rapidly, leaving not enough time for vasculature imaging [72]. Due to the invasive catheterization procedure involved in this procedure and the resultant 2D images, the application of DSA has been replaced by other noninvasive or less invasive 3D techniques such as Doppler ultrasonography, magnetic resonance angiography (MRA) and computed tomography angiography (CTA) [73, 74].

Color Doppler ultrasonography has a spatial resolution of 200 μm with a relatively poor penetration depth making the imaging limited to the superficial parts of the body. Acoustic angiography is a new technique that provides high resolution images of the superficial microvasculature [75, 76]. Low penetration depth, in the order of a few millimeters, is the main limitation of this technique.

CTA is an angiography technique that uses a narrow x-ray beam along with multiple detector arrays rotating around the region of interest to produce cross-sectional data. The cross-sectional data is then analyzed through reconstruction algorithms to generate angiograms. CTA can provide excellent details of the vascular tree in small arteries. A limitation of 3D-CTA is the inability to resolve blood vessels with a diameter less than 400 μm [77]. CTA also delivers a high dose of radiation which limits the number of examinations a patient can undergo due to the carcinogenic potential of x-ray exposure [78].

A lengthy imaging time has been considered a major drawback of the MRA compared to the CTA. However, the recent development of 32-channel coils and introduction of parallel imaging acceleration techniques have significantly reduced the imaging time [79]. Contrast-enhanced MRA methods require an injection of paramagnetic gadolinium-based Chelate agents through a peripheral vein. Blood relaxation times are shortened by the effect of paramagnetic agents. This effect causes blood to appear bright on T_1-weighted images. Pre- and post-injection images are then subtracted to remove the surrounding tissues, generating an image of the vascular network within the region of interest. Using this technique, vessels with a size of 300 μm in diameter can be detected in MR images of a clinical scanner [80].

Time of flight (TOF) and phase contrast (PC) are two techniques in MRA to depict the vasculature without administration of an intravenous contrast. In TOF, inflow of fully magnetized spins to the imaging volume results in an increase in the received signal while the outflow of the spins results in decreased signal intensity. In the PC, blood moving spins in the same direction as the magnetic field gradient accumulates a phase shift proportional to their velocity while stationary spins gain no phase shift after application of the gradients. This information is used to determine the velocity of the blood flow. Subtraction of the image obtained with the velocity encoding gradient from that without the velocity encoding gradient yields an angiogram. A greater signal to noise ratio can be achieved using high field MR scanners (3.0 T and 7.0 T). In

[81], it has been demonstrated that the above mentioned non-contrast enhanced MRA techniques can be used to visualize the first- and second-order intracerebral arteries branches with a spatial resolution of 0.57 mm and 0.43 mm at 3.0 T and 7.0 T, respectively. On the other hand, high field 7.0 T MR scanners have a very limited availability for clinical applications due to a high cost. Both techniques (TOF and PC) rely on the blood movement. Such motion dependence limits their application in areas of low or turbulent flow.

Vascular ultrasound is a non invasive method used to examine the blood circulation through reflection of transmitted high frequency sound waves. Micron-sized gas bubbles scatter sound waves significantly. They have been used as intravascular contrast agents in vascular ultrasonography. Tube phantoms with an internal diameter of 255 μm can be visualized through estimation of the individual micro bubbles [82, 83]. However, the technique is limited in penetration depth restraining their application in visualization of the superficial vasculature or the vascular network in small animals.

Optical coherence tomography (OCT) angiography is a non invasive method widely used in 3D visualization of retinal and choroid vasculature that has achieved micrometer-level axial resolution [84, 85]. However, the scanning depth and the field of view are both limited to a few millimeters [86]. Table 2-2 compares different imaging modalities in terms of the spatial and temporal resolution and the imaging depth.

Table 2-2: Summary of differences between imaging modalities

	Spatial resolution	**Time scale**	**Imaging depth**	**Primary contrast**
X-ray / CT	~ 0.2 mm	millisec to sec	No limit	x-ray absorption by tissues
SPECT [*]	~ 4 mm	min	No limit	radiolabel atoms decay in tissues
PET [**]	~ 2 mm	min	No limit	radiolabel atoms decay in tissues
MRI	~ 0.5 mm	sec	No limit	tissues proton density
Ultrasound	~ 50 µm	millisec	mm - cm	tissues impedance difference
OCT	~ 10 µm	sec to min	~ 1-3 mm	tissue’s characteristic in scattering light

[*] Single-photon emission computed tomography
[**] Positron emission tomography

2.3.2 Visualization of microstructures

Different techniques including microscopes, pre-clinical and clinical imaging modalities have attempted to visualize the microstructures in-vivo and in-vitro. In section 2.3.2.1 the techniques applied to visualize microvasculatures and their clinical limitations are reviewed. In the following section (2.3.2.2) the application of MR scanners in molecular and cellular imaging is presented.

2.3.2.1 Microangiography

Vascular imaging has several applications including creation of a map for the vascular architecture, measuring blood flow and vascular permeability and monitoring variations in the vessels’ wall. Visualization of the blood vessels in tumors allows for evaluation of the efficiency of applied treatments such as chemotherapy, radiation therapy and targeted therapy. Microscopic methods are useful tools for displaying the structural and functional changes in the vasculature supplying the tumors. They provide the highest image quality and spatial resolution. Confocal microscopy and multiphoton microscopy have a resolution of ~100 nm and electron microscopy provides an unsurpassed resolution of a few nanometers [87]. Most microscopy techniques rely on histological tissue sections. Optical frequency domain imaging (OFDI) is a microscopy imaging technique with the ability to depict microvasculature in vivo. Tumor angiogenesis in a mouse brain is imaged using OFDI at a resolution of 10 μm [88, 89].

Advanced clinical and preclinical imaging methods are available to localize angiogenesis sites and acquire functional data in animals and in the human. Magnetic resonance imaging, computed tomography, positron emission tomography, ultrasonography and optical imaging are noninvasive methods that provide functional and structural information on the angiogenesis. Current clinical angiography methods such as DSA are excellent tools for visualization of the larger arteries and veins but not the microvasculature in tumors. High field 7 T MR scanner has shown to have superior resolution to conventional angiography images including 1.5T and 3 T MRA, and even comparable to DSA (figure 2-14) [90]. However, the clinical application of such scanners remains to be approved.

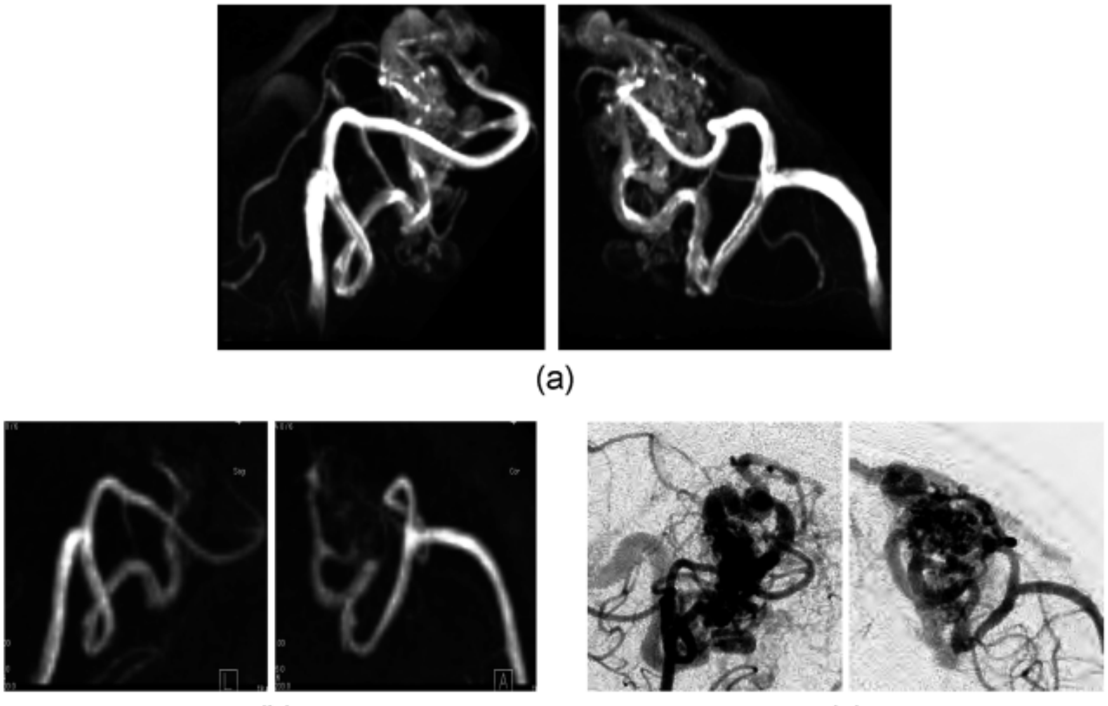

Figure 2-14: Reproduced from [90]. Angiography images acquire from a 7 T MR scanner (a), which was superior to 1.5 T images (b) and comparable to DSA (c).

Preclinical techniques such as microMRI and microCT provide a spatial resolution of ~20 µm in angiogenesis imaging in ex-vivo experiments and small animal models (figure 2-15) [91-93]. Long scanning time in the microCT involves large radiation exposures which can exceed the lethal dose limit in the animals.

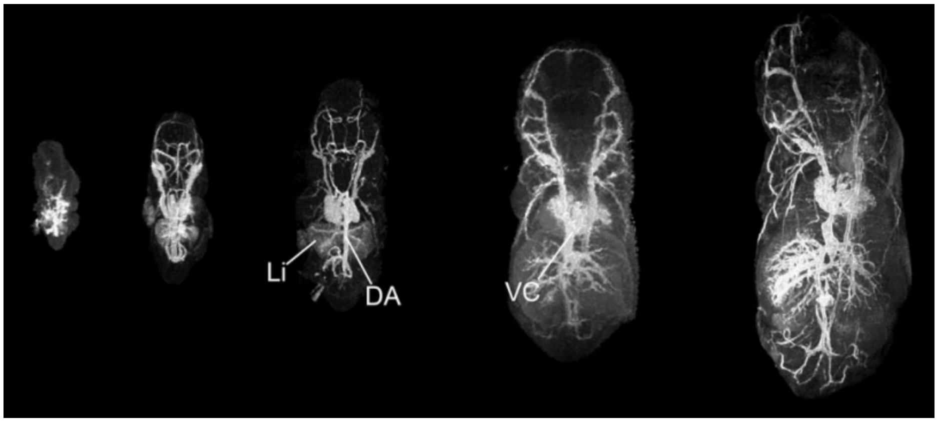

Figure 2-15: Reproduced from [93]. Contrast-enhanced microMRI images of the vasculature development acquired from a mouse embryo using a 7 T preclinical scanner.

Surface coils allow for high resolution imaging in the MRI. They consist of a single or double loop copper wire that is placed near the desired imaging area. However, due to the rapid signal uniformity decline while moving away from the center of the coil, their penetration depth is limited. Therefore, they have the highest SNR but a limited sensitive area.

Microvascular density is an indirect method for angiogenesis quantification providing number of the blood vessels per unit area of a section. In [94], an array of surface coils measuring 2 cm^2 in area was used to acquire high resolution fMRI images (0.55 mm) of human brain at 7 T originated from the neuronal-specific microvasculature. The penetration depth of the surface coils was limited to 3.5cm. Using dynamic contrast-enhanced echo-planar imaging, Gadolinium based contrast agents have also been used to estimate the microvessel intensity in the human brain [95].

The skin microvasculature can be imaged using the surface coils in the clinical MR scanners [96, 97]. Human calf skin microvasculature was imaged at 1.5 T using a high temperature superconducting surface coil with a mean diameter of 13 mm. The surface coils offer sufficient sensitivity to depict human calf vasculature at a resolution of 80 μm^3.

MR contrast is closely correlated with the tumor's microvessel intensity. The amount of contrast generated by a contrast agent is proportional to its magnetization saturation. Highly magnetic particles may be used to visualize tiny vasculatures in the MR images. Newly developed Fe-Cographitic carbon shell nanocrystals (FeCo/GC) showed to have the highest magnetization among all the magnetic materials allowing to obtain a very high sensitivity [98]. It was shown that microvessels as small as 100 μm can be resolved in the superficial circumflex iliac artery and branches of a rabbit model at 1.5 T MR using a custom designed surface coil (2.3 cm in diameter) (figure 2-16).

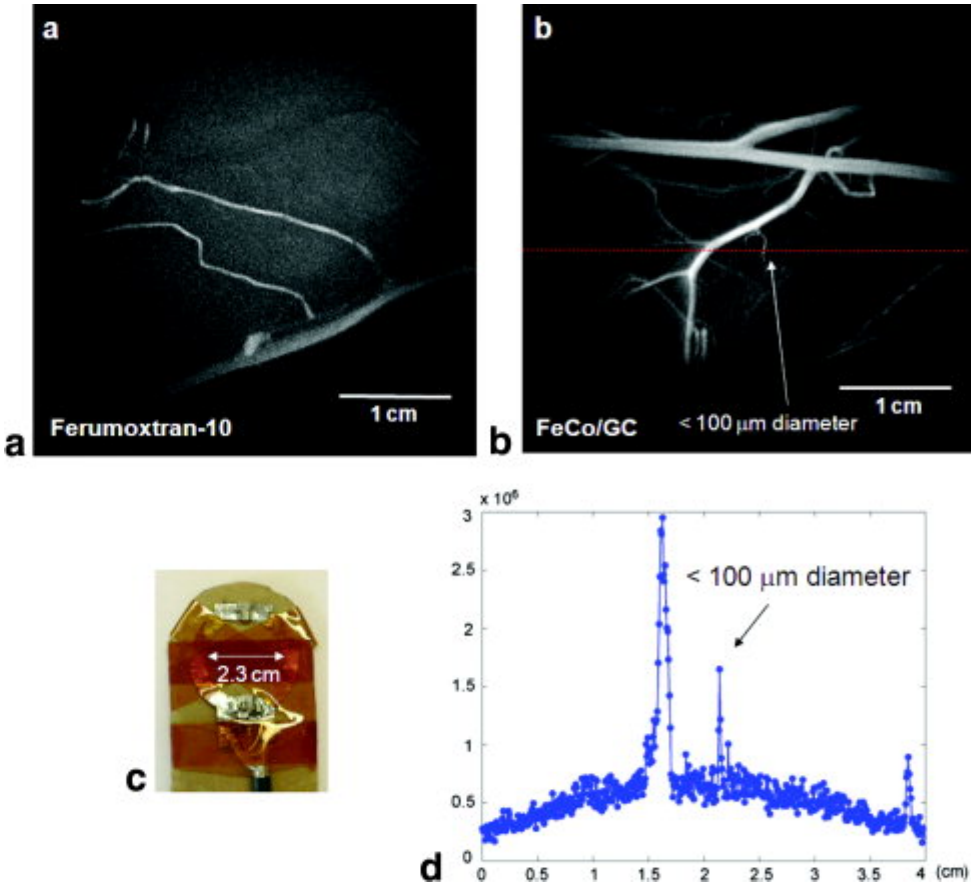

Figure 2-16: Reproduced from [98]. In vivo high-resolution MRI: **(a)** a vasculature MIP image enhanced by 1-mM blood pool concentration of ferumoxtran-10, **(b)** a vasculature MIP image enhanced by 0.2-mM blood pool concentration of FeCo/GC, **(c)** picture of 2.3 cm diameter

custom designed surface coil and **(d)** Cross-sectional signal intensity plot across a small vasculature.

2.3.2.2 Cellular and molecular imaging

Cellular scale resolution can be achieved by using clinical and preclinical MR scanners. Magnetized cells create a localized magnetic inhomogeneity in the MRI's uniform magnetic field and appear as a signal void artifact in the images. Susceptibility weighted imaging (T_2^* weighted gradient echo) provides a mean to detect the cells through the generated artifact [99]. Cellular scale resolution can be achieved by using clinical and preclinical MR scanners. Magnetized cells create a localized magnetic inhomogeneity in the MRI's uniform magnetic field and appear as a signal void artifact in the images. Susceptibility weighted imaging (T_2^*- weighted GRE) provides a mean to detect the cells through the generated artifact [100]. Vessels appear as hypersignal lines in the SE images and as hyposignals in the GRE images. However, hyposignals related to the labeled cells are not detectable in the SE images. Therefore, the difference of the two scans can reveal the hyposignal areas related to the presence of iron oxide nanoparticles. As opposed to the vasculature, signal voids have a focal nature that can be confirmed in 3D images. Hence, the exact correspondence of the signal void in the three imaging planes confirms that the hypointense signal is due to the labeled cell and not a microvessel [101].

As mentioned above, T_2^*-weighted GRE images are highly sensitive to all types of inhomogeneities. As such, they have a poor specificity to the SPIOs. T_1 and T_2-weighted spin echoes are less sensitive to the presence of the SPIOs than the T_2^* measurements. However, due to the refocusing of the background field inhomogeneities, they have a higher specificity to the presence of the SPIOs. Balanced steady state free precession (b-SSFP) is a gradient echo sequence where a coexistence of both longitudinal and transversal magnetizations is present. This condition is met when the TR is shorter than the T_1 and T_2 times of the tissue. As such, the images are weighted on the T_2/T_1 ratio. This sequence (known as FIESTA and True- FISP in GE and Siemens scanners, respectively) provides a high sensitivity to the presence of SPIOs [102, 103]. It has been shown that the True-FISP has the highest sensitivity among all the imaging sequences including GRE, EPI and SE for single cell detection in MRI [103].

Compared to the magnitude images, phase images are particularly sensitive to small deviations of the resonant frequency. However, these images are contaminated by the static field inhomogeneities as well as the phase wrapping. The static field inhomogeneity has a low frequency content that can be eliminated by the use of a high pass filter [104, 105]. Most of the studies on the in-vivo detection of the labeled cells using the MRI employ pre-clinical scanners with a high magnetic field strength (figure 2-17) [99, 100, 106-110]. In some studies, clinical 1.5 T scanners were used to detect individual labeled cells in a mice model [101, 111]. In these studies, high temperature superconducting coils or custom made gradient coils with a strength of several hundreds of millitesla per meter were employed to improve the spatial resolution

Visualization of the single cells in MR images using SPIO nanoparticles depends on the iron load in each of the labeled cells. Nanoparticles are generally internalized through a phagocytosis pathway. The particles primarily absorb on the membrane and subsequently form the nanoparticle-loaded vesicles. The vesicles then fuse with the endosomes within the cell's cytosol. During the division process the daughter cells share the magnetic endosomes in which case the iron load is halved. To overcome this problem, application of micron-sized iron oxide particles (MPIOs) is proposed [60]. Since each cell is labeled with a single magnetic particle, the daughter cell will always carry the label. MPIOs are endocytosed by a variety of cells making them an appropriate candidate for cell labeling [112].

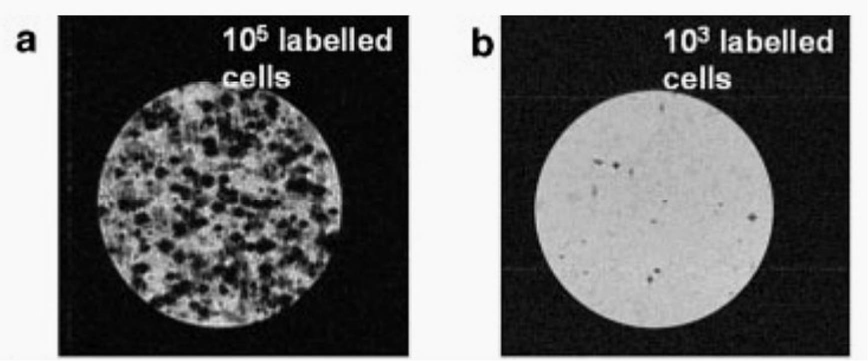

Figure 2-17: Reproduced from [109]. Detection of single cells using a 9.4 T MR scanner at an in-plane resolution of 23.5 μm. Slices of agarose gel containing 10^5 (a) and 10^3 (b) labeled cells.

2.4 Summary of the literature review

Magnetic resonance navigation was introduced as a new technique for controlled delivery of therapeutic agents to the cancer cells through application of magnetic gradients. One important step in this intervention is providing, in advance, a 3D map of the local vasculature leading to the tumor site.

Subsequently, the theory of MRI, and the application of superparamagnetic agents in the MRI were investigated in enhancing the image contrast. Superparamagnetic iron oxide particles were found to have a great potential in vascular imaging through application of the susceptibility effect. Susceptibility-based artifact is a way to amplify the effect of a magnetic particle, whereas its dimension is largely smaller than the spatial resolution of the system. Micron-sized magnetic particles act as imaging probes in the cellular and molecular imaging using preclinical MR scanner in the animal studies. Different types of artifacts and misregistrations in the MR images, caused by the presence of the magnetic materials, were studied to better understand how these particles alter the MR signal and to identify the potentials to control the extent of the magnetic particles' effect on the MR images.

Real-time MR imaging sequences and effects of magnetic particles' presence were investigated. It was found that, owing to their high specificity for detection of magnetite particles, the fast steady-state True-FISP MR sequences have a great potential for real-time tracking of the magnetic particles.

Finally, the current clinical imaging modalities and their capability in resolving the microvascular networks were studied. Poor spatial resolution and/or low penetration depth of the current clinical imaging modalities is the main limitation in resolving the microstructures including the capillaries and the arterioles.

CHAPTER 3 OBJECTIVES, HYPOTHESES AND GENERAL METHODOLOGY

Visualization of microstructures is beyond the capabilities of the current clinical imaging modalities, whereas it can be applied to many research areas such as the real-time drug delivery to tumor sites using an MRI system. MRI contrast agents (superparamagnetic) have been used in preclinical imaging modalities to visualize a single cell in small animals. We propose benefiting from the higher visibility of micron-sized magnetic particles in the microvessel blood streams to identify the vascular routes using clinical scanners.

Therefore, the research question can be defined as:

Does the application of micron-sized agglomerations of Iron Oxide nanoparticles in the MRI allow for identification of micrometric vascular routes, not detectable using current clinical imaging modalities?

In MRI, the susceptibility-based contrast provides a way to amplify the effects of a magnetic microparticle, whereas its volume is largely inferior to the spatial resolution of the system. This concept initiates an approach for visualization of microstructures such as microvessels by means of the susceptibility artifact. In the MRN, therapeutic microcarriers or contrast agents are injected through an infusion catheter which is advanced under a fluoroscopic guidance into an appropriate artery. However, the extremity of the catheter can only be advanced to the arterial level while the tumor is located at the capillary level. Therefore, upon release of the therapeutic microcarriers, magnetic gradients are applied to steer the magnetic microcarriers to the tumor site. Magnetic gradients are applied according to a predefined map of the local vasculature leading to the tumor site. Preparation of such a map is an essential step in the MRN intervention.

3.1 Objectives and hypotheses

The general objective of this study was to prepare a 3D map of the microvascular route starting from where the catheter tip is placed to the tumor site before the MRN intervention. More particularly, the envisaged steps in the identification of the vascular routes were:

i) Releasing “scout microparticles” in an unknown vascular network leading to the tumor site, *ii)* Tracking the "scout microparticles" through a real-time MR imaging,

iii) Positioning the "scout microparticles" through their susceptibility effect on the images,

iv) Assembling the calculated positions to identify the local vascular network.

The general objective of this project was fulfilled through four specific objectives.

Objectives 1 and 2 permit to evaluate the following research hypothesis:

> *Susceptibility artifact caused by the presence of a magnetic microparticle in the homogeneous magnetic field of a clinical MR scanner can reveal the presence and the position of the particle with a sub-pixel accuracy.*

Objective 1:

- Study the behavior of the susceptibility artifact created by the magnetic microparticles considering different MRI sequences and magnetic particles;
- Study the visibility limit of such particles in the clinical MR scanners through simulation and phantom studies.

Objective 2:

- Study the behavior of micron-sized agglomerations of iron oxide nanoparticles in the MR-images to replicate the susceptibility effect of the magnetic microparticle.

Objectives 3 and 4 permit to evaluate the following research hypothesis:

> *A micron-sized agglomeration of iron oxide nanoparticles can serve as a biocompatible, biodegradable contrast agent in the visualization of microstructures using a clinical MR scanner and a susceptibility-sensitive sequence. Real-time tracking of such microparticles leads to reconstruction of the microvasculature.*

Objective 3:

- Propose an algorithm for 3D reconstruction of the vascular network through which magnetic particles travel;
- Study the validation of the proposed technique through a simulation study.

Objective 4:

- Validate the proposed algorithm in 2D and 3D synthetic models in a micrometric scale.

3.2 General Methodology

In order to attain objectives 1 and 2, simulation studies and phantom experiments were performed to find out sensitivity of a clinical MR scanner in detecting magnetic microparticles. Knowing about the accuracy of magnetic particles' positioning through their susceptibility effect in the MR images was also an area of interest. Highly magnetic stainless steel beads of different diameters were used to evaluate the detection limit of the clinical MR systems using 1.5 T and 3T scanners and commercial head coils. The susceptibility signals were simulated according to the bead's dimension and their magnetic properties. The results showed that using a clinical MRI system, a single 15 μm microsphere is detectable in the GRE scans. The amount of the susceptibility artifact was found to be related to the scan parameters and the particles' size. The simulation results were subsequently compared to the MRI signal to estimate the accuracy of the simulation. The effect of imaging parameters was verified on the extent of the susceptibility artifact (Appendix A).

Shape and amount of the susceptibility artifact for various spacing and angulations between the microparticles were studied afterwards using simulations and phantom experiments. In an FOV, the particles are distributed in an unknown fashion. Since the susceptibility effect is much larger than the actual particle's size, if the spacing between the particles is smaller than a certain limit, the artifacts generated by the individual particles are almost entirely superimposed. We showed that for a pair of identical particles saturated in the MRI's magnetic field with a diameter of D, the signal loss starts to change when particles are separated ~15×D and they become fully distinguishable when their distance reaches ~ 40×D (Appendix B). This study helps to characterize the MR signal in the presence of several particles in the FOV. The obtained cutoff values (15×D and 40×D) are essential in the injection of microparticles as susceptibility effects from the individual particles may otherwise superimpose.

As it was discussed in the literature review, compared to the nanofabricated contrast agents, micrometer-sized agents can benefit from higher magnetic moments. Our first study demonstrated that, a single 15 μm diameter ferromagnetic microsphere with a high susceptibility is just visible in the T_2^*-weighted GRE images. However, ferromagnetic materials tend to maintain a high remanent magnetization, limiting their application in the MRI environment. On the other hand, superparamagnetic particles have unique properties, making them interesting candidates to be used as the MRI contrast agents discussed in Section 2.2.1.2. As the next step, the effects of microagglomerations composed of Fe_3O_4 nanoparticles were studied in the MR images. These agglomerations can resemble the signal loss behavior of microparticles in an image. In our first article (Chapter 4), we generated agglomerations of the Fe_3O_4 and studied their visibility in microchannels with internal diameters of 200 and 50 µm. These diameters fairly approximate sizes of a narrow artery or a large arteriole and a small arteriole, respectively. The size controlled micro-drops consisting of an oil-based microfluid of Fe_3O_4 were generated by 1) a T-junction microfluidic device and 2) suspension of oil in water in the presence of a surfactant. It was confirmed that the microagglomerations of nanoparticles are a promising candidate for reproduction of microparticles' effect in the MR images. It was also confirmed that the method is reproducible and accurate at the sub-pixel level.

In order to achieve our objectives 3 and 4, a synthetic microvascular network was dynamically mapped through the injection of Fe_3O_4 agglomerations and was scanned in real-time (Chapter 5). The vascular network was designed to have an inlet channel branching into eight smaller channels in a three-stage division with an inner diameter of 150 µm. The imaging was performed using a 1.5T MR scanner, a typical 8-channel head coil and over a relatively large FOV (16×16 cm^2). Particles were localized through "Center Of Gravity" (COG) of the artifacts which they generated in the images. The results of this study suggested the accuracy of the 2D reconstruction of the microvessels characterized by a measured average error of approximately half of a pixel's size. Limits of a 1.5 T scanner in detecting such microagglomerations were also investigated. We showed that the agglomerations measuring 50 µm in diameter are detectable in the MR images. In this study, we developed a reliable technique for generation of uniform magnetic boluses (microagglomerations of iron oxide nanoparticles) through a T-junction microfluidic device made of Plexiglas and treated with Silica to obtain a hydrophilic surface. With the applying of this technique, we were able to control size of the agglomerations as well as their spacing.

In the third article (Chapter 6), we proposed a method for 3D mapping of vascular networks through a fast multi-slice multi-acquisition MR sequence. A simulation study was performed to validate the feasibility of the proposed algorithm. A phantom study was then performed in a glass made artificial network using microagglomeration of Fe_3O_4 nanoparticles. The agglomerations were positioned in a 3D space and all the extracted *x*, *y* and *z* coordinates were assembled to build up a 3D distribution of the artificial vascular network.

For the phantom studies, micro channels were fabricated on Plexiglas. We also developed a technique to form agglomerations of oil-based ferrofluid in water through a T-junction geometry. In chapter 7, the fabrication process and the technique to generate oil in water droplets are explained and illustrated.

Our results confirmed the possibility of tracking trajectory path of the iron oxide microparticles injected in a vascular network using a susceptility-sensitive fast MRI sequence. An assembly of the trajectory maps can represent the local vasculature which is smaller than the spatial resolution of the MR scanner

CHAPTER 4 ARTICLE 1: MAGNETIC RESONANCE IMAGING OF MICROVESSELS USING IRON-OXIDE NANOPARTICLES

N. Olamaei[1,2], F. Cheriet[2] and S. Martel[1]

[1] Nanorobotics laboratory, École Polytechnique Montréal, Montreal, Canada

[2] Imaging and 4D Visualization laboratory, École Polytechnique Montréal, Montreal, Canada

4.1 Abstract

The visualization of microstructures including blood vessels with an inner overall cross-sectional area below approximately 200 µm, remains beyond the capabilities of current clinical imaging modalities. But with magnetic resonance imaging (MRI), magnetic entities cause susceptibility artifacts in the images by disrupting the homogeneous magnetic field in a much larger scale than their actual size. As validated in this paper through simulation and in-vitro experiments, these artifacts can serve as a source of contrast, enabling microvessels with an inner diameter below the spatial resolution of any medical imaging modalities to be visualized using a clinical MR scanner. For such experiments, micron-sized agglomerations of iron-oxide (Fe_3O_4) nanoparticles were injected in microchannels with internal diameters of 200 and 50 micrometers (µm) equivalent to a narrower artery or a larger arteriole, and down to a smaller arteriole respectively. The results show the feasibility of the proposed method for microparticle detection and the visualization of microvessels using a 1.5 T clinical MR scanner. It was confirmed that the method is reproducible and accurate at the sub-pixel level.

4.2 Introduction

X-ray angiography is considered the method of reference for vasculature visualization.[1,2] It is an invasive procedure that involves selective catheterization and contrast injection into blood vessels. This technique achieves a spatial resolution of ~200 µm. Although the technique provides the highest spatial resolution among all imaging techniques and modalities, it cannot be applied to the visualization of human arterioles with diameters smaller than ~200 µm.

MRI is a noninvasive technique that applies a radio frequency pulse to disturb the aligned nuclear spins and detects the resultant realignments following termination of the pulse. The spins reorientation is tissue-dependent and is the source of contrast in MR images. MRI offers several advantages including absence of ionizing radiation, excellent soft tissue contrast and a relatively high spatial resolution. Conventional MR scanners at 1.5 T provide a spatial resolution of ~0.8 mm. This value can be improved to ~0.5 mm for 3.0 T scanners.[3]

Preclinical imaging modalities have been shown to be able to produce resolutions required for resolving the microstructures of animal models. Yet, visualization of small human microstructures such as lymph nodes, cell clusters and microvascular networks remains beyond the resolution competence of the current clinical imaging modalities. Real-time drug delivery to tumor sites can benefit from microvasculature visualization through magnetic resonance imaging.[4] The technique is based on therapeutic magnetic microcarriers (TMMC) steered and tracked using an upgraded MRI system. Metabolism of tumors depends on their microenvironment. The vascular network provides them with nutrients and, from a therapeutic perspective, could also be used to deliver anticancer drugs. The microcarriers are released and steering gradients are applied to guide the microcarriers towards a selected entry site of a capillary network. Prior to the intervention, it is essential that a 3D map of the local microvasculature around the tumor supports identification of the arterial delivery path. Angiogenesis and microvascular imaging is performed through quantification of the blood volume map and the vascular volume fraction in the region of interest (ROI) using superparamagnetic agents.[5] This technique results in visualization of the microvessel density in the ROI. For specific detection (targeting) of macromolecules (in cellular imaging) and endothelial cells (in microvascular imaging), ligands such as antibodies, peptides and aptamers, are required to be conjugated to the MRI contrast agents to induce a hypo-intense signal in the vicinity of the non-targeted tissue.[6-8] Angiogenesis imaging using clinical MR scanners have shed light onto microstructure characterization; nonetheless it is not appropriate for delineation of the microvessels in detail and in a 3D representation.

Due to their high magnetic susceptibility, magnetic materials cause inhomogeneity in the local magnetic field of the MRI system to an extent much larger than their size. The inhomogeneity appears in T_2^*-weighted gradient echo images in the form of a signal loss (hypo-intense signal). The signal loss degrades the quality of the MR images. However, this artifact can serve as a source of contrast. The amount of the signal loss is directly proportional to the susceptibility, the total magnetic volume and the scan parameters. Therefore, susceptibility-based contrast provides a mean to visualize magnetic particles with volumes largely inferior to the spatial resolution of the imaging system.

The visualization of single particles through the susceptibility artifact has been applied to the cellular imaging. It has a large range of application in understanding the mammalian cell biology i.e., cell transplantation and for monitoring cell migration. Several studies have been performed to detect single cells using MRI.[9-12] In order to detect single cells, high resolution MR images at an in-plane resolution of about 100×100 μm is obtained by using either ultra high field pre-clinical MR scanners[10-12] or custom-built gradient coils.[13] But as far as we know, no techniques based on susceptibility artifacts have been applied for the visualization of smaller blood vessels.

In Ref 14, we showed that a single stainless steel sphere measuring 15 μm in diameter with a saturation magnetization of 207 emu g^{-1} can be detected in the images of a 1.5 T clinical MR scanner. It was shown that the disruptions of the magnetic field caused by the particle could be detected from a distance away at least as large as 70 times its own diameter.

Our objective is to visualize microchannels having diameters smaller than the spatial resolution of the system. A 1.5T MR scanner and conventional RF coil arrays were used to detect individual ferrofluid microagglomerations. Microagglomerations can resemble the signal loss behavior of microparticles in an image. Each microagglomeration was composed of superparamagnetic magnetite nanoparticles (MNPs) suspended in carrier oil. A T-junction microfluidic device was used to generate ferrofluid microagglomerations [15] with a size allowing sufficient magnitude of the magnetic dipole to be detectable at the boundaries of the MR scanner's voxel.

In our previous studies, we investigated the detectability of a magnetic micropparticle within the constraints of clinical MR scanners using in-vitro and simulation experiments.[14,16] Here, the application of the magnetic microagglomerations behaving like a microparticle in the visualization of the microvasculature is studied.

This article is organized as follows: The theory of the magnetic field created by the magnetic microagglomeration in the presence of an external field is described in section 4.3. Section 4.4.1 describes an algorithm for the 3D reconstruction of the microvessels based on the detection of the micro-aggregations. Section 4.4.2 is dedicated to the in-vitro experiments on the 2D microchannels prior to concluding remarks in Section 4.5.

4.3 Theory

Due to the field inhomogeneity caused by their elevated susceptibility, magnetic particles induce a distortion in the MR images. The induced field inhomogeneity creates two forms of artifact in the MR images; geometrical distortion and echo shifting.[17,18] Geometrical distortion is the misregistration of the spins' position caused by the field variations occurring during the frequency encoding. If G_x and G_x' represent the amplitude of the readout gradient and the background gradient caused by magnetic field inhomogeneity, respectively, spins residing at position x will be mapped to the apparent position x':

$$x' = x\left(1 + \frac{G_x'}{G_x}\right) \qquad \text{(Eq. 4-1)}$$

Additionally, the presence of an extra gradient along the read-out direction results in a time shift in the gradient echo (GE) relative to the sampling window. A GE that is not centered in the acquisition window causes signal loss in an MR image. Owing to their 180° refocusing pulse, the echo shifting artifact is mitigated in the spin echo (SE) scans. Data reconstruction is performed on the basis of ideal echo time (TE) being the origin in the k-space. Therefore, the echo shift leads to a phase shift across the voxel upon Fourier transformation:

$$\Delta\phi = \left|\gamma \Delta B_z(\vec{r}) TE\right| \qquad \text{(Eq. 4-2)}$$

where ΔB_z is the z-component of the field produced by the magnetic object and γ is the gyromagnetic ratio of the protons. If $\Delta\phi$ equals 2π, or a nonzero positive integer multiple of 2π, a complete dephasing occurs and the voxel signal vanishes entirely. The field distribution induced by the magnetic microparticle (microagglomeration) at position $\vec{r}$ can be approximated by the magnetic fields of a dipole [19]

$$\Delta B_z(\vec{r}) = \frac{\mu_0}{4\pi}\left(3\frac{(\vec{m}.\vec{r})\vec{r}}{r^5} - \frac{\vec{m}}{r^3}\right) \qquad \text{(Eq. 4-3)}$$

where the magnetic dipole moment of the microparticle or microagglomeration having radius a and saturation magnetization M_{sat} is:

$$\vec{m} = \frac{4}{3}\pi a^3 \vec{M}_{sat} \qquad \text{(Eq. 4-4)}$$

Since the MRI's homogeneous magnetic field (B_0) magnetizes ferromagnetic and superparamagnetic particles to saturation (or very close to saturation), neither B_0 nor the magnetic susceptibility difference is expressed in the magnetic field distribution equation. The normalized signal decay from a particle of homogeneous spin density (ρ) becomes:

$$\frac{s}{s_0} = \rho_0 \int_V e^{-i\Delta B_z(\vec{r})TE} d^3r \qquad \text{(Eq. 4-5)}$$

Equations 4-3 through 4-5 address the signal loss caused by the phase accumulation at the TE. However, GE images are influenced by both forms of artifacts. It has been shown that in GE images of conventional MR scanners echo shifting's impact dominates that of a geometrical distortion. In Ref 12, image simulation was performed based on: *i*) geometrical distortion and echo shifting and *ii*) echo shifting only. Major deviations were observed in the results obtained from the high-resolution images (< 100 µm) of the high field MR scanners. Nonetheless, no significant difference was observed for image resolutions of > 200 µm. The artifact's position is expected to reflect the exact position of the microparticle or ferrofluid microagglomeration for microvessels' imaging.

Lengthening the TE is an evident approach to pronounce the dephasing effect in the GE sequences (see Eq. 4-2). It has been shown that the signal loss in GE sequences is independent of the strength, in-plane resolution, and orientation of the readout gradient.[20]

4.4 Materials and Methods

4.4.1 Simulation experiment

To simulate microagglomerations' trajectory in microchannels, an algorithm was developed on the basis of the susceptibility artifact. The algorithm was then examined to understand its behavior in the absence of system nonlinearities. The echo shifting emerging from the phase accumulation at the TE (see Eq. 4-5) was used to simulate the susceptibility artifact. A 3D Y-shaped microchannels were generated using random spatial coordinates. The microchannels fit in a volume of 4×4×4 cm^3. The images were evaluated on a coronal and a transversal plane with a slice thickness of 4 mm and a pixel spacing of 0.5 mm which are typical parameters for a conventional MR scanner. The diameter of the particles and the TE were set to 50 µm and 30 ms, respectively. The diameter of the channels was considered to be the same as the particles' diameter. Microagglomerations were released, scanned and positioned along the trajectory. The position of the artifact reflects the exact position of the microagglomeration. The artifact has the shape of a four-leaf clover with two axes of symmetry in coronal and sagittal planes and is symmetric around the *z* axis (direction of B_0) (FIG. 4-1A). As such, the position of the particle was determined by spotting the center of the artifact. The pixel representing the center (P) was calculated based on the weighted average of the pixels' positions (X_k) in the region of interest (ROI). The intensity (I_k) of each pixel was used as the weight factor (Eq. 4-6). The result of this equation is known as the ''center of mass''.[21] When the particle fills more than one pixel, this equation provides an estimate of the particles position with sub-pixel accuracy.

$$P = \sum_k X_k I_k \Big/ \sum_k I_k \qquad \text{(Eq. 4-6)}$$

In the presence of a number of particles in the field of view (FOV), the shape of the susceptibility artifact varies based on the distance between the particles. In order to associate the position of a particle to the center of the produced artifact in the image, each signal void must represent a single microparticle. To meet this requirement, a minimum distance needs to be maintained between the particles. The shape and the amount of the susceptibility artifact for various spacing between the particles were studied in Ref. 16. The results implied that for a pair of identical particles with diameter *d*, the shape of the susceptibility artifact change when the particles are separated by more than 15×*d* and they become completely distinguishable when their distance reaches 40×*d*. However, for distances < 15×*d* the susceptibility artifacts generated by the two particles are nearly superimposed and the shape of the signal void is similar to that of a single particle. It was also shown that the obtained cut-off values are independent of the particle's diameter and the image resolution. Therefore, in the current simulation a distance of 30×*d* was used for particles spacing. This distance ensures visibility of individual particles.

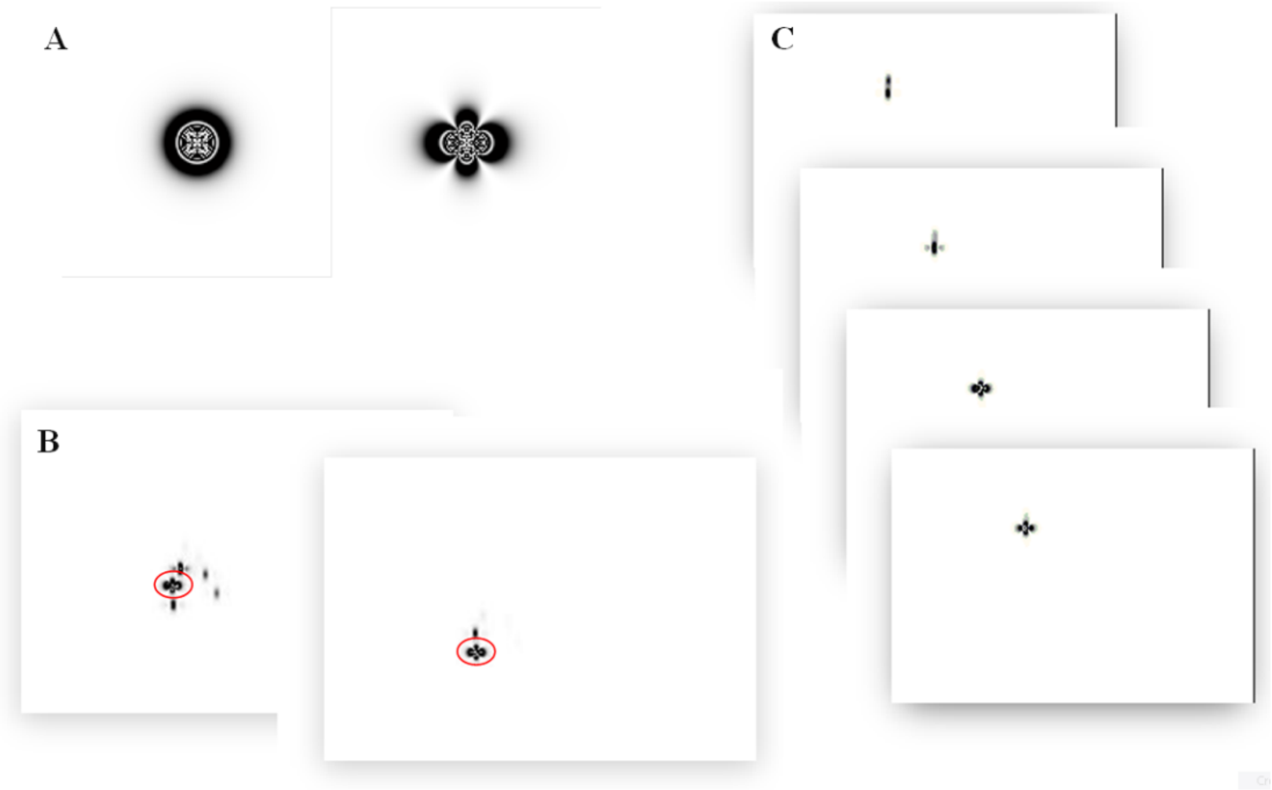

Figure 4-1: Simulated transversal (left) and coronal (right) gradient echo images for a magnetic particle (A). Two different slices are shown in (B) Circled areas show complete signal loss which indicates the presence of a particle in each of the slices. Several slices were scanned within the volume of interest and scans were repeated for a number of times to ensure all of the particles are captured in the collected images. The third image from the top shows a complete signal loss indicating the presence of a particle in the image (C).

Temporal resolution for tracking was set to the value used in a fast single slice GE sequence (~2 s). In an arteriole of 10 to 100 μm in inner diameter, the blood flow is approximately 1 mm/s.[22] Considering an acquisition time of 2 s., particles were displaced about 2 mm at the scan intervals. Several slices were scanned within the volume of interest and the scans were repeated for a number of times to ensure that all particles were captured in the collected images (FIG. 4-1C). To position the particles, the artifacts with a complete signal loss (circled areas in FIG. 4-1B were selected from the collected images of each slice. Position of a particle along the third dimension is defined by the position of the scanned slice.

Figure 4-2 depicts the sagittal images obtained from the scans at different slices. At each scan, the coordinate of the particle was calculated as formerly described in Section 4.4.1. Figure 4-3 illustrates the points reconstructed by using the transversal and the sagittal scans. The reconstructed points were compared with the original generated spatial coordinates to calculate the positioning error (Table 4-1). The obtained error values were averaged and expressed in the number of pixels. The error on the perpendicular axis of a particular plane was measured to be double the error calculated on the plane itself; axis z and x in transversal and sagittal planes, respectively. As the signal to noise ratio (SNR) decreases with a reduction of the slice thickness, the imaging voxel on the third dimension is always constrained by a minimum acceptable value.

Figure 4-2: Images obtained from the scans at different slices. At each slice a complete signal loss indicates the presence of a particle.

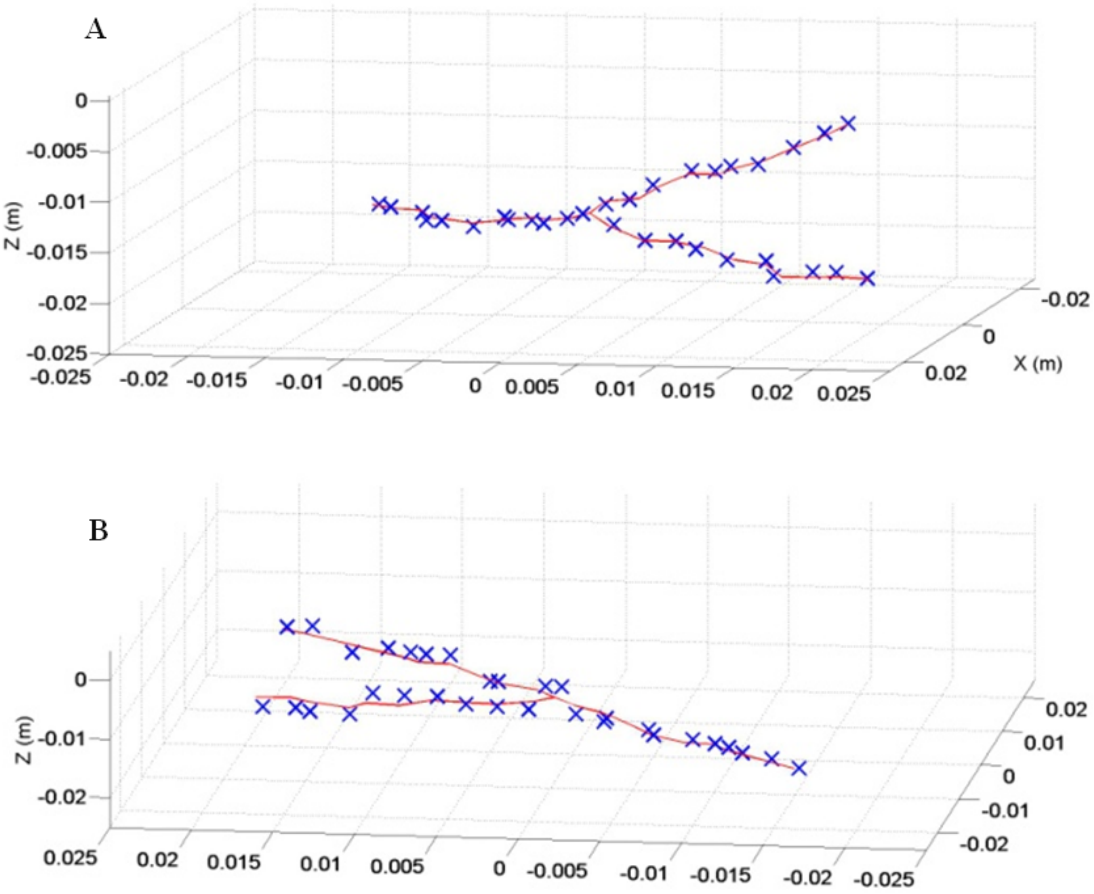

Figure 4-3: Simulated 3D channel (solid line) and reconstructed points (×) using sagittal (A) and transversal (B) scans.

Table 4-1: Mean positioning errors expressed in the number of pixels (pixel size=0.5 *mm*) in reconstructed channels using sagittal and coronal scans.

Imaging plane	*X*	*Y*	*Z*
Sagittal	2.02 ± 0.05	1.05 ± 0.06	1.07 ± 0.05
Transversal	1.20 ± 0.06	1.3 ± 0.09	2.4 ± 0.11

4.4.2 In-vitro experiments

An oil-based ferrofluid (Ferrotec) was used to generate susceptibility-based contrast in MR images. The ferrofluid contained 10 % magnetite nanoparticles (MNP: Fe_3O_4) measuring 10 nm in diameter, 10 % oil soluble dispersant and 80% oil-based carrier liquid. Magnetic properties of the particles were measured with a Vibrating Sample Magnetometer (VSM) **(**EV9, Microsense**)** at room temperature. The saturation magnetization was measured at 68 emu g^{-1} and it was confirmed through the hysteresis curve that the particles were saturated at 1.5 T.

In order for the nanoparticles to create sufficient disruption in the magnetic field and become detectable in MR images, oil-in-water micro-drops were used. The size-controlled micro-drops consisting of microagglomerations of MNPs were generated by a) a T-junction microfluidic device and b) suspenstion of oil in water in the presence of a surfactant. The microagglomerations generated by method *a* were injected in a 2D Y-shaped microchannel of 200 µm in diameter and those produced by method *b* were injected in a capillary of 50 µm in diameter.

A 2D microfluidic chip was created from poly-methylmethacrylate (PMMA) fabricated by micro-milling (LPKF Protomat) and high-pressure thermal sealing technique. The microfluidic included a T-junction and a Y-shaped channel of 200 µm in diameter (FIG. 4-4A). The T-junction was used to generate microagglomerations of MNP based on the cross flowing rupture technique [15] and the Y-shaped part was used for imaging purposes. The continuous phase (water + surfactant) was introduced from the vertical channel and the dispersed phase (oil-based ferrofluid) was introduced from the perpendicular channel. Sodium Dodecyl Sulfate (SDS) of 0.1 *wt%* was added into the water phase to control the interfacial tension between the two phases. The size and the distance of the droplets were controlled by the flow rate of the two introduced phases. To obtain droplets of ~ 200 µm in diameter distanced apart at ~ 6 mm, flow rates were fine tuned at 30 µL/min and 1 µL/min for the continuous and the dispersed phases, respectively (FIG. 4-4B).

The other method opted to generate micrometer-sized ferrofluid microagglomerations, was based on the formation of water-oil micro-emulsions. The technique involves dissolving an aqueous phase into an oil phase in the presence of a surfactant to stabilize the suspension. As such, an emulsion of ferrofluid droplets was suspended in water in the presence of 0.1 *wt*% SDS.

The average size of obtained emulsion spherical droplets was measuring at 50 µm ± 20 (FIG. 4-5A).

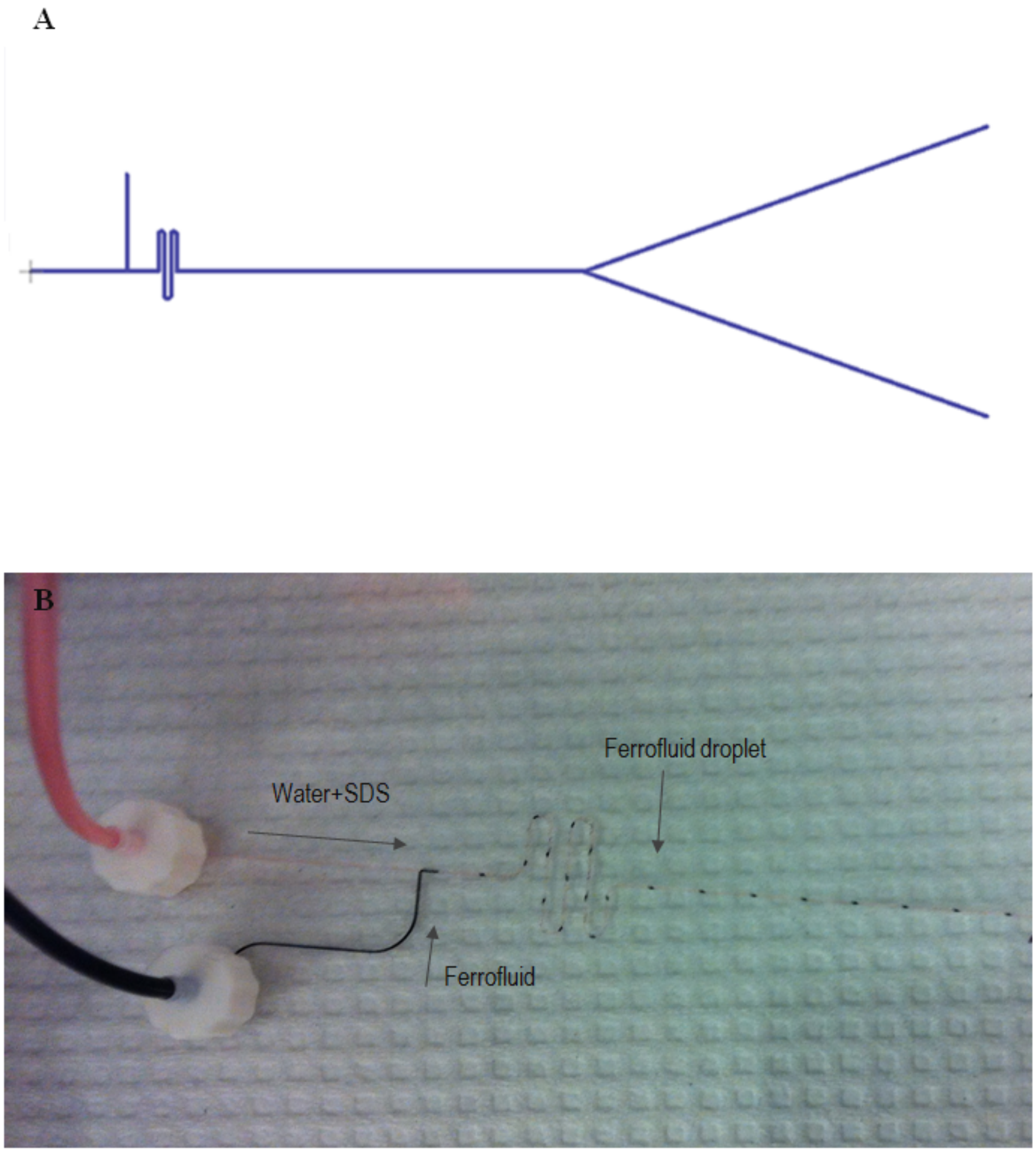

Figure 4-4: 2D microfluidic chip made of PMMA included a T-junction for micro-drop generation and a Y-shaped channel of 200 µm in diameter for imaging purposes (A). The T-junction was used to generate microagglomerations of nanoparticles based on the cross flowing rupture technique (B).

The particles were injected in a capillary of 50 µm in diameter (FIG. 4-5B). To mimic the human body relaxation times, both the microfluidic and the capillary were suspended in the middle of a solution made of gelatin and Sodium Chloride. The extremities of the chip were kept out of the gelatin to minimize the susceptibility artifact in the images caused by the accumulation of particles in the outlets and the inlets. The capillary was suspended in the gelatin in a 3D U-shape.

The MR imaging was performed using a 1.5T (Magnetom Siemens) MRI system. Images were acquired with the standard 8 channel head coil. The injection was paused during the imaging process. Two different MRI sequences were used; gradient echo (GE) (TR = 500 ms, TE = 10 ms, slice thickness=4mm, resolution = 256^2 and pixel spacing = 0.6 × 0.6 mm) and balanced gradient echo (TrueFISP) (TR = 4.7 ms, TE = 2.6 ms, slice thickness = 4 mm, resolution = 256^2 and pixel spacing = 0.6 × 0.6 mm). The former provides the maximum delectability for magnetic particles by pronouncing the signal loss and the latter provides a rapid acquisition time allowing for real-time imaging.

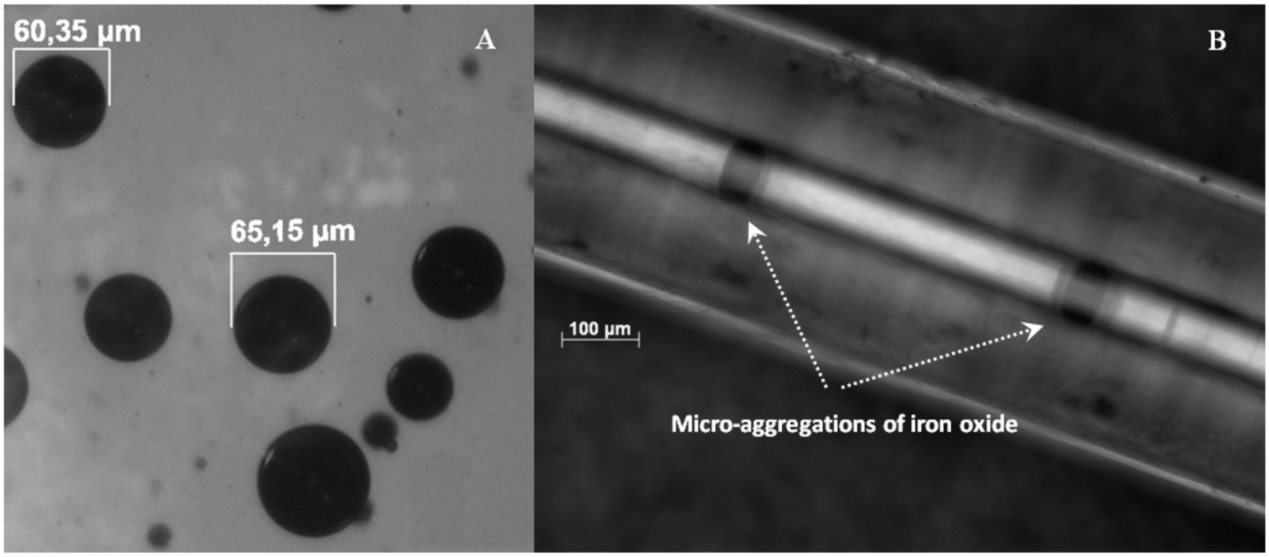

Figure 4-5: Emulsions of ferrofluid droplets were suspended in water in the presence of 0.1 wt% SDS to generate stabilized droplets. The average size of obtained emulsion spherical droplets was measured at 50 µm ± 20 (C) (A) Oil-based ferrofluid microagglomerations injected in a capillary tube measured 50 µm in diameter (B).

Figure 4-6 shows the MR images of the 200 μm channels with GE (A) and TrueFISP (B) sequences. The microagglomerations measured 200 μm in diameter. The acquisition times for coronal images (4mm thick, 256×256) were 176 and 2.1 seconds for GE and TrueFSIP sequences, respectively. The susceptibility artifacts were detected in the channels and the shape of the artifact corresponds to the theory.

The MR imaging was executed at several different time instants. At each iteration center of the artifacts, points (x), were measured (FIG. 4-7A) and compared to the actual values (FIG. 4-7B). Absolute errors (x_{real}-x_{measured}) are expressed in the number of pixels in Table 4-2. Repeated measures analysis of variance (two-way ANOVA) suggested good reproducibility across the iterations ($F(14,84)=0.4997, P=0.9272$), and also good repeatability within each data set ($F(6,84)=1.449$, $P=0.2058$).

The visibility of the 50 μm capillary was investigated in the experiments as shown in FIG. 4-8. The capillary was injected with microagglomerations measuring 50±20 μm in diameter (see FIG. 4-5A). Figures 4- 8.A through 4-8.D show images captured with the GE sequence, multi slice scan with an acquisition time of 174 sec, and FIG. 4-8.E shows the image captured with the TrueFISP sequence and an acquisition time of 2.1 sec. The echo time of the GE scans for the 200 μm channel was set to 10 ms. This value was changed to 50 ms for 50 μm capillary scans to increase the size of the artifact in the images and thus to improve their visibility. However, the particles are hardly visible in the TrueFISP images. The capillary was reconstructed based on the proposed algorithm. At each slice the coordinates of the artifacts' centers were calculated and collected to build a 3D distribution of the capillary. The reconstructed image is shown in Figure 4-9.

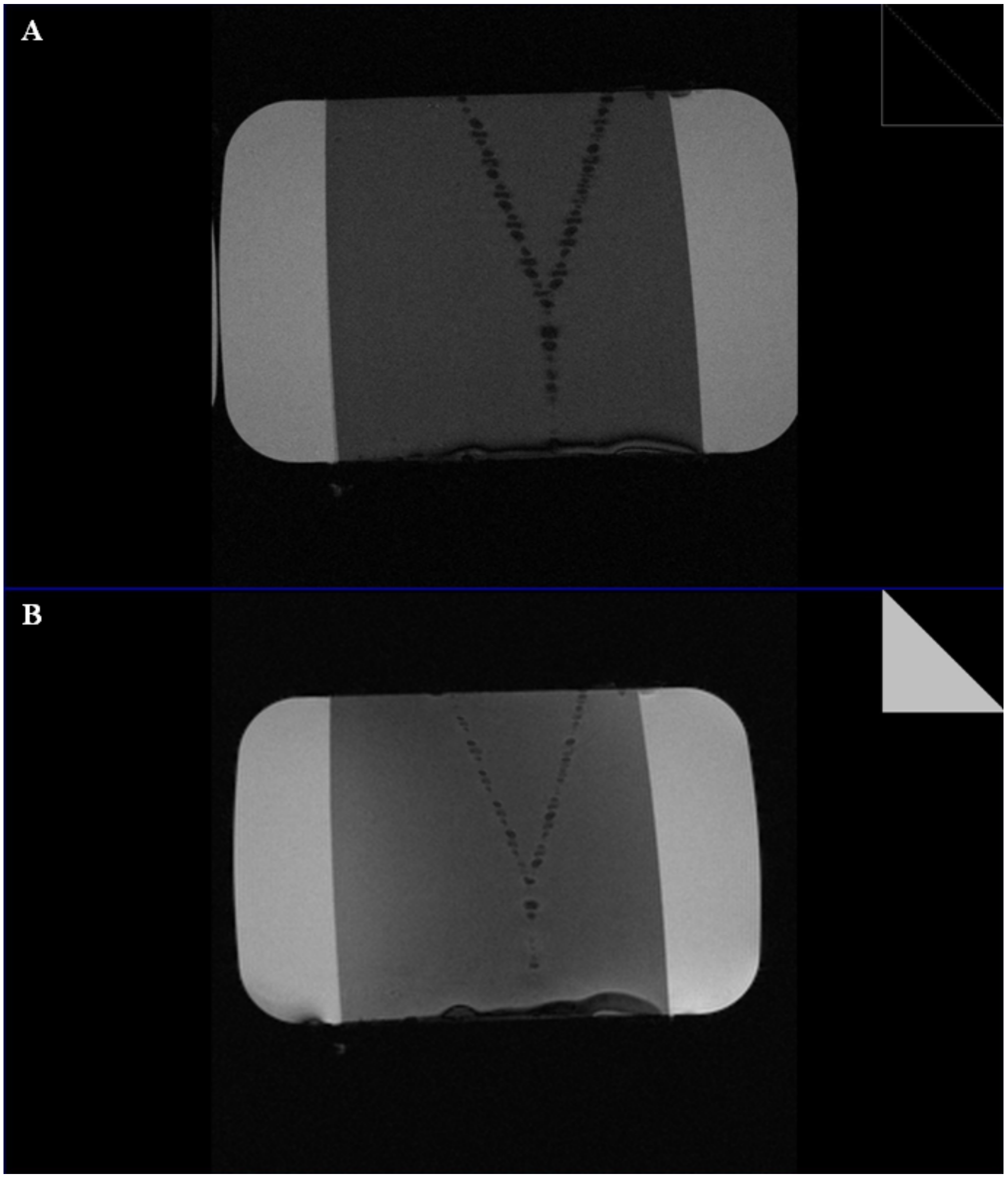

Figure 4-6: Images of the 200 μm channels imaged by a 1.5 T clinical MR scanner using a GE sequence (A) with the following imaging parameters: TR=500ms, TE=10 ms, slice thickness=4 mm, resolution = 256×256, pixel spacing =0.6×0.6 mm^2 (A) and a TrueFISP sequence (B) with the following imaging parameters: TR=4.7ms, TE=2.6 ms, slice thickness=4 mm, resolution = 256×256, pixel spacing =0.6×0.6 mm^2.

Table 4-2: Absolute errors expressed in the number of pixels for reconstructed points from the MR scans acquired at seven different time instants.

Repetition No.	**1**	**2**	**3**	**4**	**5**	**6**	**7**
Positioning error of the reconstructed points (n=15) expressed in the number of the pixel	1.028	1.043	0.311	0.904	0.756	0.569	0.024
	1.249	0.866	0.100	0.507	0.311	1.115	0.321
	0.928	0.344	0.134	0.679	0.435	0.469	0.536
	0.493	0.493	0.579	0.091	0.684	0.053	1.225
	0.432	0.244	0.455	0.392	0.870	0.029	0.636
	1.021	0.144	0.144	0.129	0.512	0.120	0.517
	0.823	0.627	0.297	1.063	0.823	0.067	0.067
	0.962	0.038	0.014	0.234	0.277	1.133	0.588
	0.966	0.655	0.411	0.287	0.799	0.780	0.694
	0.718	0.072	0.387	0.411	0.966	0.804	0.172
	0.344	0.636	1.220	0.995	0.225	0.282	0.383
	0.239	0.488	0.679	0.239	1.138	0.828	0.076
	0.244	1.406	0.679	0.698	1.076	0.579	0.301
	0.550	1.258	0.462	0.488	0.182	0.330	0.268
	0.88	0.262	0.862	0.277	0.713	1.421	0.231
Mean	0.725	0.572	0.449	0.493	0.651	0.572	0.403
Standard deviation	0.319	0.421	0.320	0.311	0.311	0.437	0.312

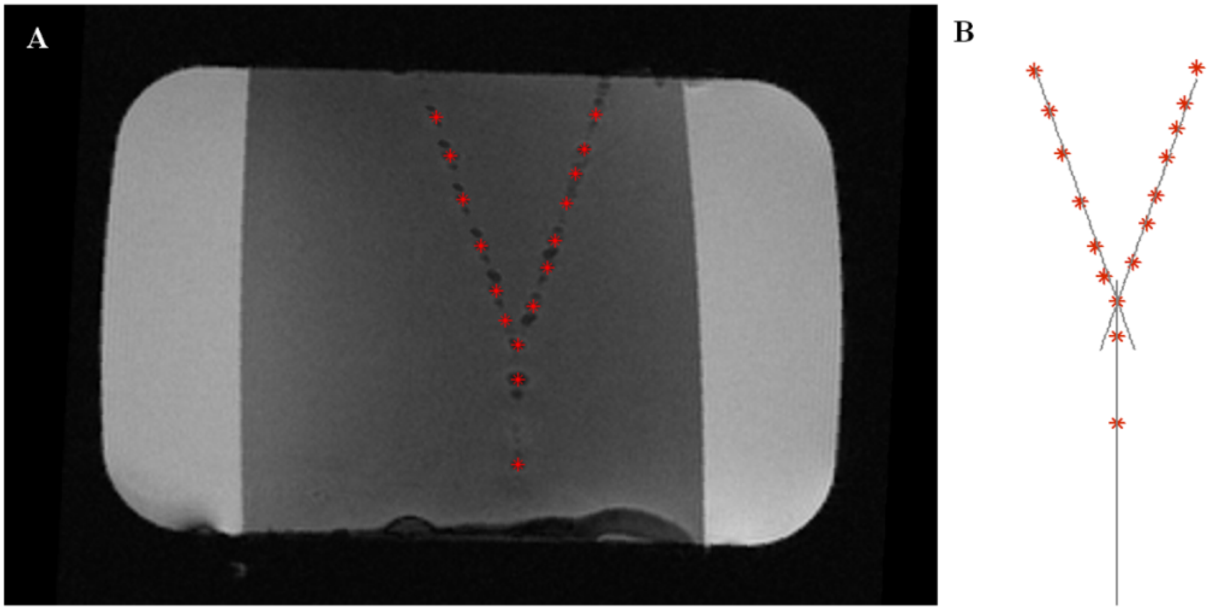

Figure 4-7: The measured points shown as * determined from the center of the artifacts (A) are compared to the real values shown as solid lines (B) to calculate the absolute measurement errors (Table 4-2).

4.5 Discussion

The simulation results proposed promising accuracy in 3D reconstruction of the microchannels. Combining the reconstructed points generated by the scans of two different planes ex. transversal and coronal can compensate for the error difference on the third dimension.

The 50 μm capillary injected with the microagglomerations is hardly visible in the TrueFISP image. FIG.4-6E displays the limitation of a 1.5 T clinical MR scanner in real-time visualization of iron oxide microagglomerations. The results shown in figures 4-5 and 4-6 demonstrate the feasibility of the proposed method in microagglomerations positioning. The average error was less than a pixel for all the seven trials (standard deviation=0.155). The results confirm a high reproducibility and repeatability across the repetitions and within each group.

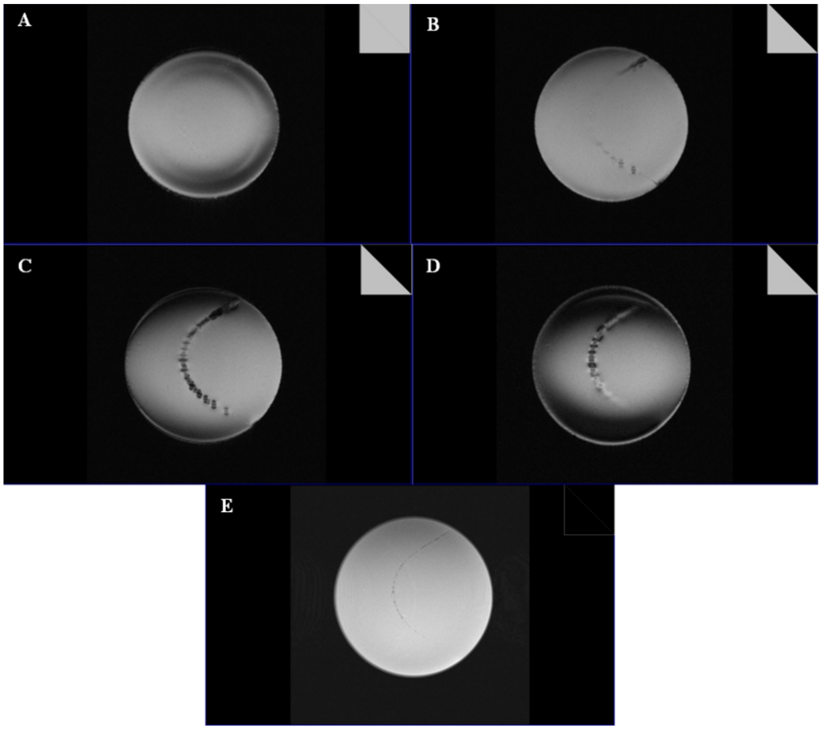

Figure 4-8: Images of the 50 μm capillary imaged at different slices (A-D) by a 1.5 T MR scanner using a GE sequence (A) with the following imaging parameters: TR=500ms, TE=50 ms, slice thickness=4 mm, resolution = 256×256, pixel spacing =0.6×0.6 mm^2 (A) and a TrueFISP sequence (E) with the following imaging parameters: TR=5.2ms, TE=2.6 ms, slice thickness=4 mm, resolution = 256×256, pixel spacing =0.6×0.6 mm^2.

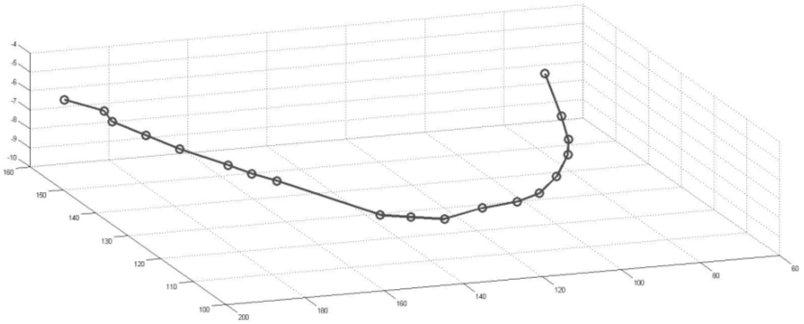

Figure 4-9: The reconstructed capillary is shown by positioning signal voids in different slices shown in FIG. 4-6. At each slice the coordinates of the artifacts' centers were calculated and collected to build a 3D distribution of the capillary.

4.5.1 Iron-oxide nanoparticles

Susceptibility-based negative contrast provides a mean to amplify the effect of a particle in the MR images whereas its volume is largely inferior to the spatial resolution of the system. In this study, the application of the susceptibility artifact is suggested to map the microchannels, the limited resolution of which falls beyond the adequate ranges of the clinical imaging modalities. Contrast agents have been widely used in MRI to improve blood vessel visualization. Paramagnetic agents (ex. gadolinium ion) produce positive contrast by accelerating spin-lattice relaxation. Superparamagnetic agents such as iron-oxide nanocrystals (SPIO) produce negative contrast by accelerating spin-spin relaxation. SPIOs have a number of attractive qualities that make them a promising alternative to gadolinium-based contrast agents. Depending on their size and coating, they benefit from biocompatibility, long circulating half-life and the possibility of clearance from the blood circulation through the reticuloendothelial system.[23] Due to their unique properties, they have been widely investigated for biomedical applications such as angiogenesis imaging in tumors and molecular-cellular imaging.[24,25] Clinical MR scanners can image density of the microvessels through quantification of the blood volume map and vascular volume fraction in the region of interest. However, the images are not capable of providing a detailed 3D map of the microvessels.

4.5.2 Microagglomerations of nanoparticles

In this study, the application of microagglomerations composed of nanoparticles is suggested for microstructures' visualization. Magnetic moment of a micrometer-sized particle is a function of the saturation magnetization and the volume of the particle. The advantage of using microagglomerations is the concentrated mass of a magnetic material in a small micro-volumetric space. Consequently, microagglomerations can resemble the signal loss behavior of microparticles in an image. The symmetric property of the microagglomerations' signal loss can be used to track them along a trajectory. Jointly, the biocompatibility and biodegradability characteristics of the iron-oxide nanoparticles enhance their application. To our knowledge, oil-based ferrofluid has never been used experimentally as a MRI contrast agent. However, water in oil emulsions composed of iodized oil and an aqueous solution carrying anti-cancer drugs is widely used for treatment of the hepatic tumors.[26,27]

4.5.3 Droplet generation

Emulsions contain droplets with varying diameters. Microfluidic devices are widely used to generate monodisperse population of micro-drops. One of the most frequently applied microfluidic devices for droplet generation are ‘T-junctions’. The droplet formation is based on the breakup of a continuous phase of one liquid caused by shear from the cross flow of a second immiscible phase. The advantage of using a microfluidic device is the precise control over the formation of the immiscible fluid segments. The size of the droplets and their spacing depend on the geometrical dimension of the channels as well as the flow rates of the dispersed and continuous flows.[28,29] As described before, the size of the artifact varies as a function of the droplet diameter. If the distance between the droplets drops below ~15 times their diameter, the artifact generated by the individual particles are almost entirely superimposed and the shape of the signal loss resembles that of a single particle. In the presence of several particles in the FOV with a spacing < 15×d, the artifact in the images will be a large continuous signal loss through which, positioning of the particles is impossible. Therefore, it is essential to keep a minimum distance between the particles. Injection of monodisperse equidistant microagglomerations can be performed using a microfluidic device.

Magnetic particles have a strong tendency to agglomerate in the presence of the MRI magnetic field. This makes their injection with a controlled spacing challenging. Encapsulating the particles with degradable polymers prevents them from being agglomerated. However, a relatively large shell is needed to maintain the minimum distance between the particles. This results in larger particles incapable of reaching the microvasculature system. To overcome this problem, we generated the droplets in a microfluidic device inside the MRI bore where there is a homogeneous magnetic field and no magnetic force is exerted on the particles. However, the in-vitro experiment could not follow the proposed algorithm in reproducing the blood flow rate.

In the simulation model, the flow rate in the arterioles (1 mm/sec) was used. However, limitations of the injection system in the in-vitro experiments prevented us from reproducing the flow rate of 1 mm/sec in the channels. The injection pumps were placed at the extremity of the MRI bed to avoid interaction between the MRI’s magnetic field and the metallic parts of the pumps. Therefore, tubes required to deliver the ferrofluid and the water, were extended along the MRI bed towards the center of the bore where the microchannels were located. A relatively high-pressure gradient produced along the tubes limited the lower value of the flow in the channels. To cope up with this, the injection was paused during the imaging sequences. This pause prevented from the observation and study of the motion artifact resulted from movement of the particles in the images.

Signal void is used as an indication of the presence of iron oxide microagglomerations. Nevertheless, the presence of different sources of negative contrast in the human body encumbers the distinction of the negative contrast associated with the magnetic particles. Application of positive contrast approaches based on modified pulse sequences or post-processing methods [30,31] can improve the visibility of the magnetic particles in the human body.

At the capillary level, multiple vessels are located within a single voxel. Consequently, visualization of the capillary networks applying the proposed technique becomes more challenging. In Ref 12, the possibility of subvoxel tracking is demonstrated. This technique may be applied to find the relative position of the detected particle within a voxel.

4.6 Conclusion and future work

A method is proposed to map microchannels using a clinical MR scanner. The method is based on real-time tracking of the magnetic microagglomerations. In the proposed technique, the information of time discrete scans is extracted and assembled to build a 3D distribution of the microchannels. Microagglomerations of iron-oxide nanoparticles proved to be a promising candidate for reproduction of the microparticles' effect and improvement of their visibility in the MR images.

The variation analysis of the results confirmed the reproducibility of the method and proved the accuracy of the point reconstruction of the susceptibility artifacts to be at the sub-pixel level. As the next step, we intend to validate our method by mimicking the microvasculature blood flow in the channels. To avoid using extended tubes along the MRI bore and to deliver the immiscible liquids, a new microfluidic design with a built-in reservoir may be applied. Properly spaced droplets will be accumulated in this reservoir before positioning the setup in the MRI bore. The signal loss induced by the droplets shall open numerous future possibilities for the application of clinical MR scanners in the microstructure and microvessel imaging.

Acknowledgment

The project is supported in part by the National Science and Engineering Research Council of Canada (NSERC) and Fonds Québécois de la Recherche sur la Nature et les Technologies (FQRNT). The authors would like to thank Mahmoud Mohammadi for his assistance with the generation of microagglomerations.

References:

[1] R. J. Nijenhuis et al., "MR angiography of the great anterior radiculomedullary artery (Adamkiewicz artery) validated by digital subtraction angiography," AJNR Am. J. Neuroradiol. 27, 1565–1572 (2006).

[2] H. M. Silvennoinen et al., "CT angiographic analysis of carotid artery stenosis: comparison of manual assessment, semiautomatic vessel analysis, and digital subtraction angiography," AJNR Am. J. Neuroradiol. 28, 97–103 (2007).

[3] I. M. Thomas Wittlinger, A. Moritz, and S. Romanzetti, "Evaluation of the spatial resolution with1.5–4 Tesla in a Stenosis Model," Asian Cardiovasc. Thorac. Ann. 15, 387–393 (2006).

[4] P. Pouponneau et al., "Magnetic nanoparticles encapsulated into biodegradable microparticles steered with an upgraded magnetic resonance imaging system for tumor chemoembolization," Biomaterials 30, 6327–6332 (2009).

[5] Y. Tang et al., "In vivo assessment of RAS-dependent maintenance of tumor angiogenesis by real-time magnetic resonance imaging," Cancer Res. 65, 8324–8330 (2005).

[6] A. R. Guimaraes et al., "MRI with magnetic nanoparticles monitors downstream anti-angiogenic effects of mTOR inhibition," Mol. Imaging Biol. 13(2), 314–320 (2011).

[7] J. R. McCarthy et al., "Targeted nanoagents for the detection of cancers," Mol. Oncol. 4(6), 511–528 (2010).

[8] J. R. McCarthy and R. Weissleder, "Multifunctional magnetic nanoparticles for targeted imaging and therapy," Adv. Drug Deliv. Rev. 60, 1241–1251 (2008).

[9] E. M. Shapiro et al., "In vivo detection of single cells by MRI," Magn. Reson. Med. 55, 242–249 (2006).

[10]E. M. Shapiro et al., “Sizing it up: Cellular MRI using micron-sized iron oxide particles,” Magn. Reson. Med. 53, 329–338 (2005).

[11]E. M. Shapiro et al., “MRI detection of single particles for cellular imaging,” Proc. Natl. Acad. Sci. U.S.A. 101, 10901–10906 (2004).

[12]G. Zabow et al., “Microfabricated high-moment micrometer-sized MRI contrast agents,” Magn. Reson. Med. 65(3), 645–655 (2010).

[13]P. Foster-Gareau et al., “Imaging single mammalian cells with a 1.5 T clinical MRI scanner,” Magn. Reson. Med. 49, 968–971 (2003).

[14]N. Olamaei et al., “MRI visualization of a single 15 micron navigable imaging agent and future microrobot,” Conf. Proc. IEEE Eng. Med. Biol. Soc. 2010, 4355–4358.

[15]J. H. Xu et al., “Preparation of highly monodisperse droplet in a T-junction microfluidic device,” AIChE J. 52, 3005–3010 (2006).

[16]N. Olamaei et al., “Accurate positioning of magnetic microparticles beyond the spatial resolution of clinical MRI scanners using susceptibility artifacts,” in 2011 Annual International Conference of the IEEE Engineering in Medicine and Biology Society (Embc), (2011), pp. 2800–2803.

[17]J. R. Reichenbach et al., “Theory and application of static field inhomogeneity effects in gradient-echo imaging,” J. Magn. Reson. Imaging 7, 266–279 (1997).

[18]D. A. Yablonskiy and E. M. Haacke, “Theory of NMR signal behavior in magnetically inhomogeneous tissues—The static dephasing regime,” Magn. Reson. Med. 32, 749–763 (1994).

[19]E. M. Haacke, Magnetic Resonance Imaging: Physical Principles and Sequence Design (Wiley, New York, 1999).

[20]C. Bos et al., “On the artifact of a subvoxel susceptibility deviation in spoiled gradient-echo imaging,” Magn. Reson. Med. 50, 400–404 (2003).

[21]Y. Ivanov and A. Melzer, “Particle positioning techniques for dusty plasma experiments,” Rev. Sci. Instrum. 78, 033506 (2007).

[22]R. Klabunde, Cardiovascular Physiology Concepts (Lippincott Williams & Wilkins, 2005).

[23]J. S. Weinstein et al., "Superparamagnetic iron oxide nanoparticles: Diagnostic magnetic resonance imaging and potential therapeutic applications in neurooncology and central nervous system inflammatory pathologies, a review," J. Cereb. Blood Flow Metab. 30, 15–35 (2010).

[24]A. K. Gupta and M. Gupta, "Synthesis and surface engineering of iron oxide nanoparticles for biomedical applications," Biomaterials 26, 3995–4021 (2005).

[25]A. S. Arbab et al., "Characterization of biophysical and metabolic properties of cells labeled with superparamagnetic iron oxide nanoparticles and transfection agent for cellular MR imaging," Radiology 229, 838–846 (2003).

[26]H. Demachi et al., "Simulation model based on non-Newtonian fluid mechanics applied to the evaluation of the embolic effect of emulsions of iodized oil and anticancer drug," Cardiovasc. Intervent. Radiol. 23, 285–290 (2000).

[27]T. de Baere et al., "Modification of arterial and portal hemodynamics after injection of iodized oils and different emulsions of iodized oils in the hepatic artery: An experimental study," J. Vasc. Interv. Radiol. 9, 305–310 (1998).

[28]R. Seemann et al., "Droplet based microfluidics," Rep. Prog. Phys. 75, 016601 (2012).

[29]C. X. Zhao and A. P. J. Middelberg, "Two-phase microfluidic flows," Chem. Eng. Sci. 66, 1394–1411 (2011).

[30]M. Stuber et al., "Positive contrast visualization of iron oxide-labeled stem cells using inversion-recovery with ON-Resonant water suppression (IRON)," Magn. Reson. Med. 58, 1072–1077 (2007).

[31]C. H. Cunningham et al., "Positive contrast magnetic resonance imaging of cells labeled with magnetic nanoparticles," Magn. Reson. Med. 53, 999–1005 (2005).

CHAPTER 5 ARTICLE 2: DYNAMIC TRACKING OF MAGNETIC NANOPARTICLES FOR MAPPING MICROVASCULAR NETWORKS USING A CLINICAL 1.5 T MAGNETIC RESONANCE SCANNER

N. Olamaei[1,2], F. Cheriet[2] , Sylvain Deschênes[3] and S. Martel[1]

[1]NanoRobotics Laboratory, Ecole Polytechnique Montréal, 2500 chemin de Polytechnique, H3T 1J4 Montreal, Canada

[2]Imaging and 4D Visualization Laboratory, Ecole Polytechnique Montréal, 2500 chemin de Polytechnique, H3T 1J4 Montreal, Canada

[3]Department of Medical Imaging, Centre Hospitalier Universitaire Sainte-Justine, 3175 Chemin de la Côte Sainte-Catherine, H3T 1C5 Montreal, Canada

5.1 Abstract

Being able to visualize blood vessels with an inner diameter of less than 150 µm is the present limit of modern medical imaging modalities and it becomes an important issue to advance state-of-the-art medical imaging, diagnostics, surgery, and targeted interventions. In cancer therapy, such capability would provide the information required for new delivery methods such as Magnetic Resonance Navigation (MRN) to navigate therapeutic agents along a planned trajectory deeper in the vasculature and hence, closer to the region to be treated for enhancing the therapeutic index. To demonstrate the possibility of gathering images of microvascular networks dynamically and beyond the limitation of medical imaging modalities, the susceptibility artifact was used as the contrast mechanism in MRI to detect magnetic microagglomerations of iron-oxide nanoparticles (150 ± 20 µm in diameter) as they were injected in a 2D synthetic microvascular network. Magnetic entities cause susceptibility artifacts in the images by disrupting the MRI's homogeneous magnetic field (B_0) in a much larger scale than their actual size. The position of the artifact reflects the position of the aggregations in the vascular system. The calculated positions of discrete-time scans were extracted and assembled to build up the distribution of the vascular network. The results suggest that this method could be used to gather images of blood vessels beyond the spatial resolution of clinical medical imaging modalities with

a measured average error confirmed on a 2D reconstruction of the microvessels of approximately half of a pixel's size.

5.2 Introduction

The visualization of vascular networks is of prime importance for several medical interventions including but not limited to Magnetic Resonance Navigation (MRN).[1-3] In this technique an upgraded clinical MRI scanner is used to navigate untethered therapeutic microcarriers along a pre-planned trajectory. The technique allows the delivery of a higher dose of therapeutics to the targeted region while decreasing the level of toxicity by minimizing systemic circulation of the drug. To take full advantage of MRN, the navigable therapeutic agents must be able to transit through thinner blood vessels which increases the demand for medical imaging modalities with higher spatial resolution. The structure of the local vascular network determines the proper MR-navigation sequences to achieve the best therapeutic outcomes.

X-ray angiography is considered the method of reference in vasculature visualization with a spatial resolution of ~0.15 mm.[4] Conventional 1.5 T clinical MRI scanners can provide a spatial resolution of approximately 0.8 mm, improving to 0.5 mm using 3 T clinical scanners.[5] Current clinical medical technologies are not yet suitable to visualize arterioles with a typical inner diameter varying from approximately 150 μm down to 50 μm. But in MRI, susceptibility-based negative contrast provides a mean to amplify the effect of a magnetic particle, whereas its dimension is significantly inferior to the spatial resolution of the system. In the presence of the MRI's homogeneous high strength magnetic field, particles become magnetized and as a result, an inhomogeneity is induced in the B_0 field. The inhomogeneity appears as a signal loss artifact in T_2^*-weighted Gradient Recalled Echo (GRE) images. The artifact can serve as a source of contrast by depicting the presence and the location of a magnetic volume in a micrometric scale.

A large number of studies have been carried out to produce high resolution images of microvessels. Application of images in the 100 μm range resolution, generated by preclinical scanners has now become a routine in small animals, cellular and molecular imaging.[6-9] Clinical scanners can identify microvessels through quantification of the blood volume map and vascular volume fraction in the region of interest.[10-12] In some other studies,[13-15] upgraded custom receiving coils have been designed to image micro-structures over a relatively small region (2-5 cm^2). However, clear and detailed imaging of arterioles in the order of 50 to 200 μm using clinical scanners remains to be further developed.

In an earlier study, we showed that using a clinical 1.5 T MRI scanner, a single ferromagnetic particle measuring 15 μm in diameter could be detected in T_2^*-weighted GRE images.[16] The high magnetic susceptibility of the ferromagnetic materials creates a high inhomogeneity in the MRI's main magnetic field and consequently, these particles become duly traceable in MR images. Adversely, ferromagnetic materials tend to maintain a high remanent magnetization, limiting their clinical applications. On the contrary, superparamagnetic particles have unique properties, making them interesting options to be used as MRI contrast agents. They do not retain the net magnetization upon the removal of the magnetic field. Furthermore, their small size (5-20 nm) helps them to easily pass through the body's capillary network and be cleared from the circulation through the phagocytic function of the reticuloendothelial system.[17]

In a previous study, we showed the application and limitations of microagglomerations of iron-oxide nanoparticles to gather images of micro-channels having internal diameters of 200 and 50 μm. However, due to a strong interaction between the magnetic nanoparticles and B_0, that is present outside the MRI bore, we failed to reproduce the blood flow rate inside the channels.[18] Thus, the injection was paused during the imaging sequence and this pause prevented us to study the accuracy of the technique in positioning moving particles.

The purpose of this study is to improve the technique by mapping a synthetic microvascular network dynamically instead of statically through the injection of iron-oxide nanoparticle agglomerations and to subsequently scan them in real-time using a rapid MRI sequence. The position of the artifact reflects the position of the agglomerations in the vascular system. The calculated positions of discrete-time scans are extracted and assembled to build up the distribution of the vascular network.

5.3 Materials and Methods

5.3.1 Distorted patterns of magnetic materials in MRI

In MRI, the spatial encoding is performed by applying a magnetic gradient field that varies linearly in space. The magnetic gradient assigns a unique precession frequency at several locations along its direction.

In GRE images, due to the absence of the 180° refocusing pulse, an echo shifting effect should also be taken into account. Therefore, the influence of a position dependent phase term ($\Delta\varphi = -\gamma.\Delta B.TE$) is added to determine the position of the spins. The normalized signal decay due to a magnetic particle of homogeneous spin density ρ is given by:

$$\frac{s}{s_0} = \rho_0 \int_V e^{-i\Delta B(\vec{r})TE} d^3 r \qquad \text{(Eq. 5-1)}$$

The additional dephasing dampens the echo signal which in turn can lead to a complete signal loss in the images. As the result of the rephasing pulse, this effect is mitigated in Spin Echo (SE) sequences. GRE artifacts are generally much more pronounced than SE artifacts.

The dephased volume resulting from the presence of a magnetic particle in B_0 is shown in Figure 5-1. The magnetic field induced by a particle was simulated by that of a dipole:

$$\Delta B_z(\vec{r}) = \frac{\mu_0}{4\pi}\left(3\frac{(\vec{m}.\vec{r})\vec{r}}{r^5} - \frac{\vec{m}}{r^3}\right) \text{ where } \vec{m} = \frac{4}{3}\pi a^3 \vec{M}_{sat} \qquad \text{(Eq. 5-2)}$$

where $\mu_0 = 4\pi \times 10^{-7}$ is the permeability of the free space, $\vec{r}$ is the position vector, and $\vec{m}$ is the magnetic dipole moment of the microparticle or microagglomerations of radius a and saturation magnetization of $\vec{M}_{sat}$. The MR images of a magnetic particle are similar to the projections of the dephased volume.

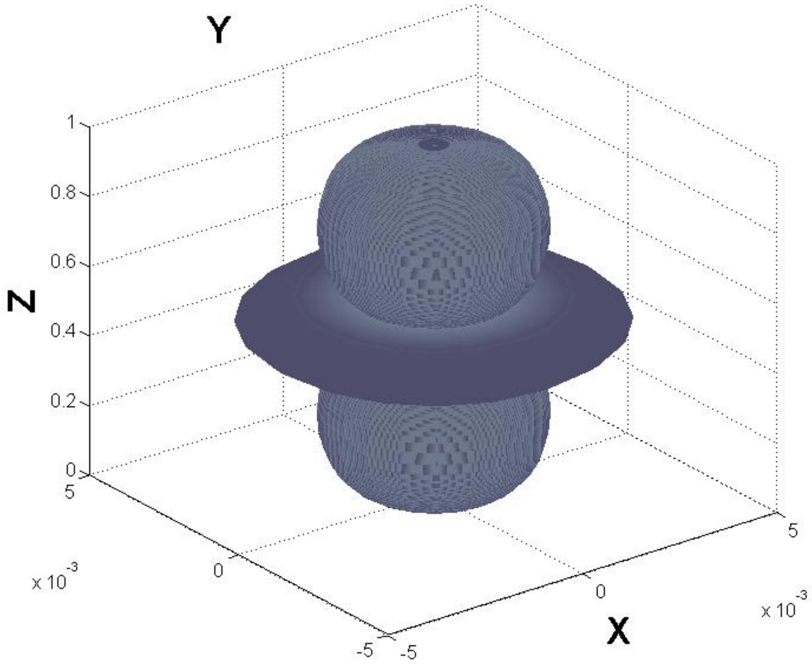

Figure 5-1: simulated dephased volume caused by a magnetic particle (see equation 2).

5.3.2 Synthetic vascular network

A mirofluidic chip with a 2D vascular network was created from polymthylmethacrylate (PMMA) using a micro-milling machine (*LPKF Protomat*). The chip was sealed using high-pressure thermal sealing technique (*LPKF Multipress II*). The vascular network was designed to have an inlet channel branching into eight smaller channels in a three-stage division (Figure 5-2a). The branching structure in mammalian vascular networks is evolved with an optimum arrangement for blood flow. At each bifurcation the diameter of the branching segment is reduced in size. The relationship between the diameter of the parent vessel (d_0) and that of the daughter's (d_1) is known as Murray's law ($d_0^3 = 2d_1^3$).[19] In our experiment, the diameter of the smallest segment was set to 150μm in diameter.

Blood vessels are hydrophilic on the surface. Conversely, PMMA is strongly hydrophobic. In order to mimic the wetting property of a blood vessel, the surface of the channels was coated with a thin layer of Silicone Dioxide (SiO_2) (~250 nm). Figure 5-2b depicts the effect of SiO_2 coating on the wetting property of the surface.

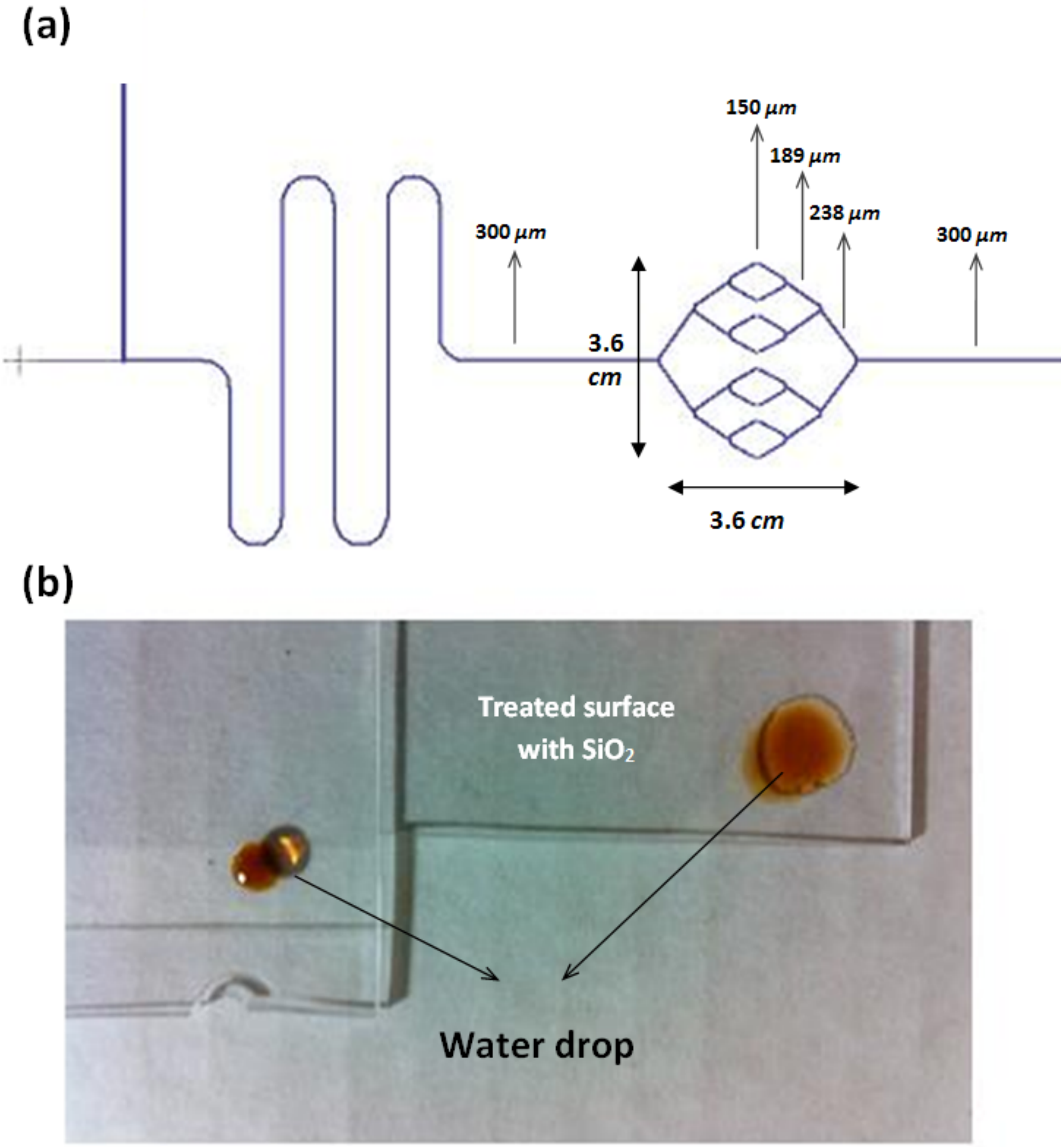

Figure 5-2: (a) Schematic illustration of the T-junction, built-in reservoir and the delivery artery pattern. The dimension of the vascular network and the diameter of the branching segments are shown. (b) The effect of the surface treatment using SiO_2 on the wetting property of PMMA.

5.3.3 Microagglomeration of iron-oxide nanoparticles

An oil-based ferrofluid (*Ferrotec*) comprising of iron oxide (Fe_3O_4) nanoparticles measuring 10 ± 2nm in diameter was used to generate susceptibility based contrast in MR images. The ferrofluid contained 10% Fe_3O_4 particles, 10% oil soluble dispersant and 80% oil based carrier liquid. Magnetic moments of the particles were measured using a Vibrating Sample Magnetometer (VSM) (*EV9, Microsense*). The saturation magnetization was measured at 68 emu/gr and through the hysteresis curve it was confirmed that the particles were saturated at 1.5 T. Oil in water droplets were generated to produce a concentrated mass of magnetic particles (microagglomerations) in a small micro-volumetric space. A T-junction geometry was included at the entry of the vascular network to generate the microagglomerations. The continuous phase (water + surfactant) was introduced from the vertical channel. Sodium Dodecyl Sulfate (0.1 wt %) was added into the water phase to lower the interfacial energy and to stabilize the formed droplets. A microliter syringe (*Hamilton Company, Model 7000.5*) with a total volume of 0.5 µL was used to inject very small quantities of ferrofluid (~0.01 µL) through the perpendicular channel (Figure 5-2a). The breakup of the continuous phase is caused by the shear from the immiscible oil-based cross flow.[20-22]

Magnetic particles have a strong tendency to agglomerate in the presence of B_0. As such, a minimum distance between the generated microagglomeration should be maintained to avoid the dipole-dipole interaction. The minimum value of the spacing depends on the volume and the saturation magnetization of the particles. A simulation model was developed to identify the minimum distance between the microagglomeration of iron-oxide nanoparticles based on their magnetic and geometric characteristics (see equation (1)). As shown in the figure 5-3, a microagglomeration pair identical in diameter (D) and saturation magnetization starts to appear separated when their distance reaches 30D. 0.01 µL of ferrofluid in volume forms a sphere of ~ 250 µm in diameters. Therefore, to avoid dipole-dipole interactions, a minimum distance of ~ 7.5 mm should be maintained between the aggregations. Figure 5-3 presents the signal intensity of the simulated image of particles of different diameters at different spacing varying from 1D to 90D. As the artifact's shape begins to change, the signal intensity grows in size. At distances of 30D and higher, the signal remains nearly constant implying the absence of an interaction between the particles and thus the visibility of individual particles in MR images.

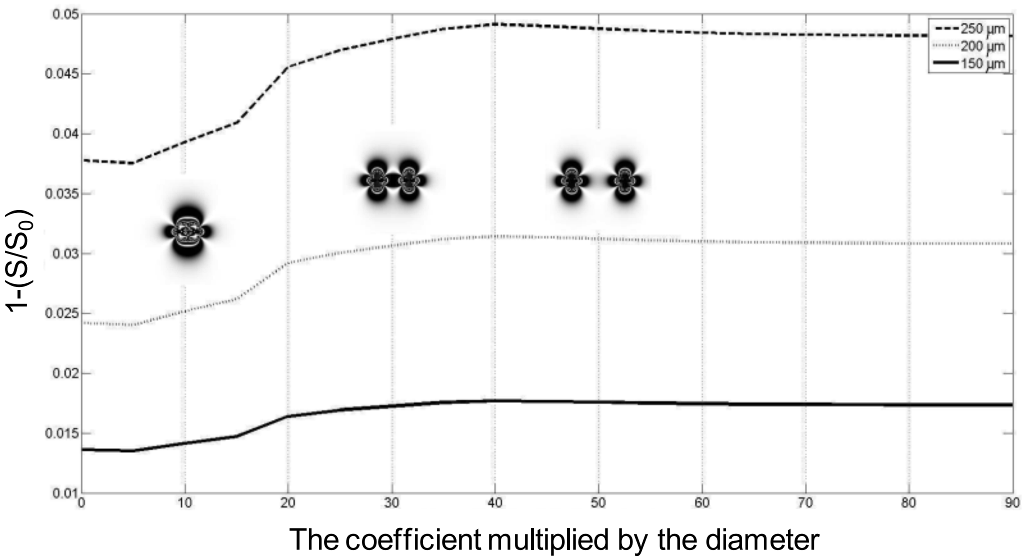

Figure 5-3: Simulated GRE signal intensity as a function of the distance between the particles on the coronal plane. The distance is labeled by multiples of the particles' diameter (D). The curve labels represent the diameter of the particles in micrometers. The simulated coronal images of two identical iron-oxide microagglomerations with a saturation magnetization of 68 emu/gr and a diameter of 150 µm are shown.

A built-in tortuous reservoir was added next to the T-junction and prior to the vascular network to collect the entire microagglomeration generated (Figure 5-2a). The aggregations were pushed forward inside the vascular network by injecting water and surfactant solution throughout the imaging sequence.

5.3.4 MR imaging

The microfluidic was suspended inside a solution comprised of gelatin and sodium chloride to mimic the relaxation times of the human body. The extremities of the microfluidic were kept out of the solution for an easy access to the injection site and to minimize the susceptibility artifact in the images caused by the accumulation of nanoparticles in the microfluidic's outlet (Figure 5-4).

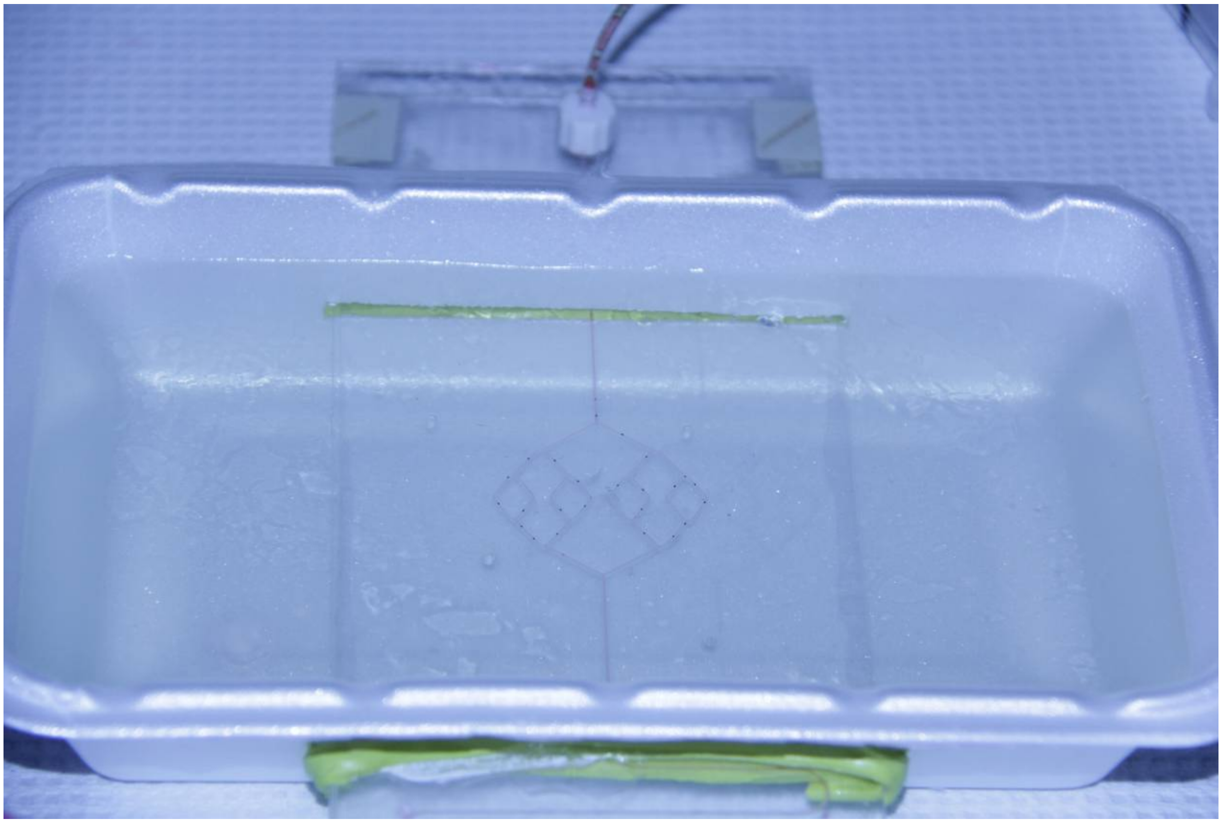

Figure 5-4: The suspended microfluidic solution comprised of gelatin and sodium chloride with the injected microagglomerations.

5.3.5 Image processing

In order to transform the different sets of data obtained from the several repetitions of the experiment into a single coordinate system, three small holes with known coordinates were added on the microfluidic chip. The known coordinates were also used to align the theoretical model on the MR images and to estimate the measurement error.

The position of the artifact represents the position of the microagglomerations. Susceptibility artifact in gradient recalled echo images creates a four-leaf clover shape on the sagittal and coronal planes and a circle shape on the transversal planes (Figure 5-1).

Particles were localized based on "Center Of Gravity" (COG) of the artifacts. COG is a sub-pixel precession estimate of the object's center.[23,24] The coordinates representing the center were calculated based on the weighted average of the pixel's positions (X_k) in the field of view, whereas, the intensity of each pixel (I_k) was used as the weight factor ($\sum_k X_k I_k \Big/ \sum_k I_k$).

The artifacts center points were determined and compared to the actual positions. Accordingly, the absolute measurement error was calculated.

5.4 Results and Discussion

The experiment was repeated twice. At each replication, multiple images were acquired while injecting the microagglomeration into the vascular network using a multi-shot True FISP sequence with the following imaging parameters: TR = 4.23 ms, TE = 2.12 ms, pixel spacing = 0.83 ×0.83 mm^2, imaging matrix = 192×192 and slice thickness = 8 mm. The scanning time for a single image was 1.01 s. The first and the second trials yielded 70 and 114 images, respectively. The signal voids of the images were visually identified and for each void the center of gravity was calculated. Particles were localized using coordinates of the center of gravity. 251 and 320 coordinate pairs were obtained from the first and the second trials, respectively. Figure 5-5 shows a number of consecutive images obtained from the second trial. The actual pattern of the vascular network used in the experiment is superposed on the images to facilitate comparison. To accurately superpose the pattern, reference points were placed on the microfluidic chip to apply rigid registration. Figure 5-6a shows the measured points from the first and second trials superposed on the vascular network's pattern. The data at each segment were fit based on a first-degree polynomial equation and the estimated vascular network was obtained (Figure 5-6b).

The calculated coordinates were compared with the actual pattern to estimate the positioning error. Mean positioning errors for the first and the second trials are presented in Table 5-1.

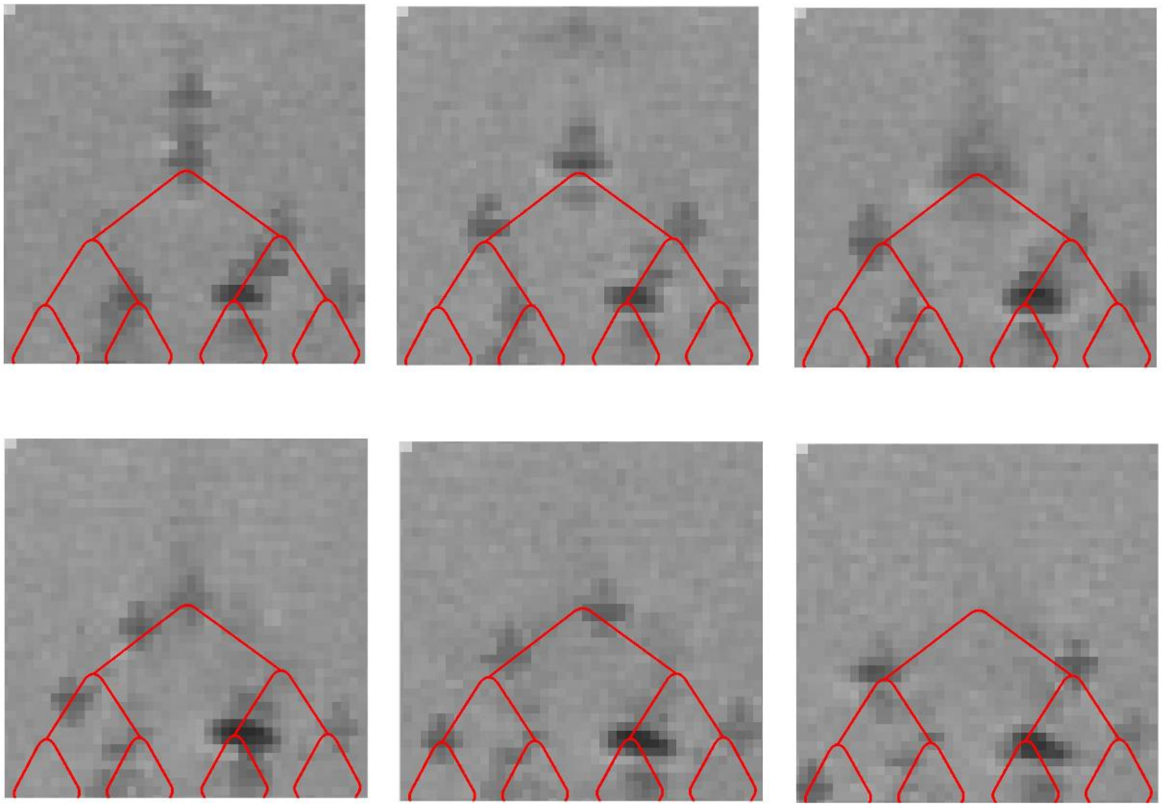

Figure 5-5: Consecutive images obtained from the second trial. The actual pattern of the vascular network is superposed on the images by applying rigid registration to facilitate the comparison.

Table 5-1: Mean measurement errors of the first and second trials

Positioning error	**Trial #1**	**Trial #2**
Mean (*mm*)	0.394	0.492
Standard deviation	0.227	0.254

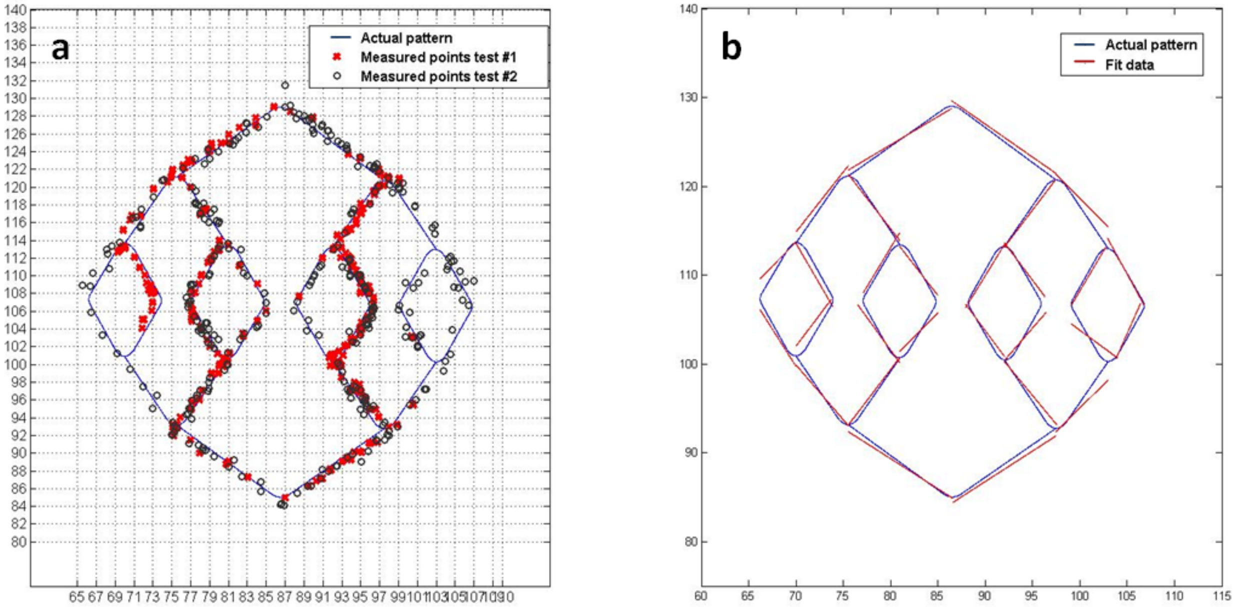

Figure 5-6: The measured points from the first (×) and second (o) trials superposed on the vascular network's pattern. (b) The acquired data at each segment were fit based on a first-degree polynomial equation and the estimated vascular network was obtained.

This paper discusses and verifies the accuracy of a method proposed for visualization of microvessels (150 µm in diameter) using a clinical 1.5 T MRI scanner and a standard 8-channel head coil. The susceptibility artifact was used as the contrast mechanism to detect magnetic microagglomerations of iron-oxide nanoparticles. GRE sequences are effective as the contrast is the result of the dephasing water near the aggregations. The fast imaging with steady-state free precession (true FISP) based on gradient recalled echo is a fast sequence that achieves a scanning time of 1 sec per slice with a high signal to noise ratio and a high sensitivity to field inhomogeneity. These characteristics of the sequence make it a proper choice for dynamic tracking of magnetic particles. Here, we are showing the possibility of visualization of a microvascular network spread over an area of 3.6×3.6 cm^2. Imaging is performed over an approximately 16×16 cm^2 FOV, using typical imaging parameters such as a pixel size of 0.83×0.83 mm^2. The results suggest an accuracy of the 2D reconstruction of the microvessels characterized by a measured average error of approximately half of a pixel's size. The calculated positioning error implies that two adjacent vessels distanced at 0.44 mm are distinguishable in MR images using the proposed technique.

Figure 5-6 presents the distribution of the measured coordinates ensemble superposed on the actual pattern. As shown, the distribution is not uniform implying non identical pressure gradients across the different branches. At the micrometric scale, a small difference in the geometry of the symmetric channels leads to a considerable imbalance in the pressure gradient inside the channels. The lack of a uniform distribution of the measured points can be caused by the imperfections in the fabrication process.

A method is proposed to map microvascular network in real-time using a clinical MR scanner and a standard receiver coil. The results proved the accuracy of the reconstruction of a 2D synthetic microvascular model to be at the sub-pixel level. To our best knowledge, it is the first time that micrometric magnetic volumes are being used as a contrasting mechanism to map microvasculature in real-time. A next potential step of this study would be to validate the technique in a 3D microvascular model.

Acknowledgment

The project is supported in part by Chaire de Recherche de l'Ecole Polytechnique (CREP) and Fonds Québécois de la Recherche sur la Nature et les Technologies (FQRNT). The authors would like to thank Oleg Zabeida from the department of Engineering Physics of Ecole Polytechnique de Montreal for his assistance with the surface treatment of the microfluidic device.

References

[1] P. Pouponneau, J. C. Leroux, and S. Martel, Biomaterials 30(31), 6327 (2009).

[2] P. Pouponneau, J. C. Leroux, G. Soulez, L. Gaboury, and S. Martel, Biomaterials 32(13), 3481 (2011).

[3] P. Pouponneau, V. Segura, O. Savadogo, J. C. Leroux, and S. Martel, J. Nanopart. Res. 14(12), 1307 (2012).

[4] M. Spahn, Nucl. Instrum. Methods Phys. Res., Sect. A 731, 57 (2013).

[5] T. Wittlinger, I. Martinovic, A. Moritz, and S. Romanzetti, Asian Cardiovasc. Thorac. Ann. 14(5), 387 (2006).

[6]E. M. Shapiro, K. Sharer, S. Skrtic, and A. P. Koretsky, Magn. Reson. Med. 55(2), 242 (2006).

[7]E. M. Shapiro, S. Skrtic, and A. P. Koretsky, Magn. Reson. Med. 53(2), 329 (2005).

[8]E. M. Shapiro, S. Skrtic, K. Sharer, J. M. Hill, C. E. Dunbar, and A. P. Koretsky, Proc. Natl. Acad. Sci. U. S. A. 101(30), 10901 (2004).

[9]G. Zabow, S. J. Dodd, E. Shapiro, J. Moreland, and A. P. Koretsky, Magn. Reson. Med. 65(3), 645 (2011).

[10]G. A. Christoforidis, J. C. Grecula, H. B. Newton, A. Kangarlu, A. M. Abduljalil, P. Schmalbrock, and D. W. Chakeres, Am. J. Neuroradiology 23(9), 1553 (2002).

[11]R. Jansen, B. Kunze, H. Reichenbach, and G. Hofle, Liebigs Ann. 1996(2), 285.

[12]Y. Tang, M. Kim, D. Carrasco, A. L. Kung, L. Chin, and R. Weissleder, Cancer Res. 65(18), 8324 (2005).

[13]P. Foster-Gareau, C. Heyn, A. Alejski, and B. K. Rutt, Magn. Reson. Med. 49(5), 968 (2003).

[14]J. C. Ginefri, M. Poirier-Quinot, P. Robert, and L. Darrasse, Magn. Reson. Imaging 23(2), 239 (2005).

[15]J. H. Lee, S. P. Sherlock, M. Terashima, H. Kosuge, Y. Suzuki, A. Goodwin, J. Robinson, W. S. Seo, Z. Liu, R. Luong, M. V. McConnell, D. G. Nishimura, and H. J. Dai, Magn. Reson. Med. 62(6), 1497 (2009).

[16]N. Olamaei, F. Cheriet, G. Beaudoin, and S. Martel, 2010 Annual International Conference of the IEEE Engineering in Medicine and Biology Society (EMBC) (IEEE, 2010), p. 4355.

[17]J. S. Weinstein, C. G. Varallyay, E. Dosa, S. Gahramanov, B. Hamilton, W. D. Rooney, L. L. Muldoon, and E. A. Neuwelt, J. Cerebr. Blood Flow Metab. 30(1), 15 (2010).

[18]N. Olamaei, F. Cheriet, and S. Martel, J. Appl. Phys. 113(12), 124701 (2013).

[19]D. R. Emerson, K. Cieslicki, X. J. Gu, and R. W. Barber, Lab Chip 6(3), 447 (2006).

[20]R. Seemann, M. Brinkmann, T. Pfohl, and S. Herminghaus, Rep. Prog. Phys. 75(1), 16601 (2012).

[21]J. H. Xu, S. W. Li, J. Tan, Y. J. Wang, and G. S. Luo, AIChE J. 52(9), 3005 (2006).

[22] C. X. Zhao and A. P. J. Middelberg, Chem. Eng. Sci. 66(7), 1394 (2011).

[23] Y. Feng, J. Goree, and B. Liu, Rev. Sci. Instrum. 78(5), 53704 (2007).

[24] Y. Ivanov and A. Melzer, Rev. Sci. Instrum. 78(3), 33506 (2007).

CHAPTER 6 ARTICLE 3: THREE DIMENSIONAL RECONSTRUCTION OF A VASCULAR NETWORK BY DYNAMIC TRACKING OF MAGNETITE NANOPARTICLES

Nina Olamaei[12], Farida Cheriet[2], Sylvain Deschênes[3], Azadeh Sharafi[1] and Sylvain Martel[1]

[1]NanoRobotics Laboratory, Ecole Polytechnique Montréal, 2500 chemin de Polytechnique, H3T 1J4 Montreal, Canada

[2]Imaging and 4D Visualization Laboratory, Ecole Polytechnique Montréal, 2500 chemin de Polytechnique, H3T 1J4 Montreal, Canada

[3]Department of Medical Imaging, Centre Hospitalier Universitaire Sainte-Justine, 3175 Chemin de la Côte Sainte-Catherine, H3T 1C5 Montreal, Canada

6.1 Abstract

Visualization of small blood vessels feeding tumor sites provides important information on the tumors and their microenvironment. This information plays an important role in targeted drug therapies using magnetic gradients. However, complex microvascular networks cannot be resolved using current clinical imaging modalities. To solve this problem, a method is presented for 3D mapping of vascular networks based on the magnetic susceptibility artifact. Micron-sized agglomerations of Magnetite nanoparticles were injected in a 3D phantom vascular network and a fast multi-slice multi-acquisition MR sequence was applied to track the agglomerations along their trajectories. The susceptibility artifact in the images indicates the presence and the position of the agglomerations. The calculated positions through multiple images were assembled to build up the 3D distribution of the vascular network. The results suggest that the technique can be used for reconstruction of blood vessels beyond the spatial resolution of clinical medical imaging modalities at sub-pixel accuracy.

Index Term—MRI, Magnetic susceptibility contrast, Magnetite nanoparticles, 3D reconstruction.

6.2 Introduction

Visualization of the vascular network leading to tumoral sites offers the potential to significantly improve targeting of agents loaded with magnetic nanoparticles and therapeutics that can be navigated using a method known as magnetic resonance navigation (MRN). MRN relies on magnetic resonance imaging (MRI) to induce a steering force on the magnetic nanoparticles, magnetized to saturation in the presence of the strong homogeneous magnetic field (B_0) of the MRI scanner, to direct them toward a targeted area such as a tumor site with high efficacy [1-3]. Subsequently, the magnetic gradient coils of the scanner are used to induce a steering directional force on the microcarriers. The direction and the time at which the gradients are applied are determined based on the ability to determine the local vasculature leading to the targeted physiological area. However, the navigation in thinner vessels is limited by the spatial resolution of medical imaging modalities.

Indeed, poor spatial resolution and/or low penetration depth of the current clinical imaging modalities are the major limitations in resolving microvascular networks. Amongst all clinical imaging techniques, digital subtraction angiography provides the highest spatial resolution of ~ 180 µm and is considered as the reference method in angiography [4, 5]. However, the approach provides 2D images and it involves the application of an iodinated contrast agent which is potentially nephrotoxic. Color vascular ultrasonography together with micron-sized bubble contrast agents provides a spatial resolution of ~ 200 µm with a relatively poor penetration [6]. This limits the application of ultrasound imaging to superficial microvasculatures. Computerized tomography angiography can provide details of the vascular tree in small arteries in a 3D fashion. It has a limit of approximately 400 µm for vessel detection [7].

MRI is a noninvasive imaging technique with the ability to visualize soft tissues of the human's body at any depth using typical birdcage receiver coils. Clinical scanners (1.5 and 3.0 T) provide an in-plane resolution of ~ 400 µm [8]. Custom designed coils can be used to improve the spatial resolution of the MR images. Microvessels as small as 100 µm in diameter can be resolved using home-built surface coils [9, 10]. However, the penetration depth of such coils is limited due to a quick drop in the signal uniformity, restraining their applicability to small animals or skin microvasculature [11,12].

All these approaches fail at providing a means to map vascular networks beyond the resolution of clinical medical imaging. As such, to compensate for a lack of spatial resolution, the signal generated by contrast agents could be amplified to a level sufficient to be detected by the imaging system. Magnetic volumes disrupt the B_0 field of a clinical MRI scanner in a much larger scale than their actual size. In [13], we showed that the disruption of the magnetic field caused by a magnetic particle saturated in B_0 could be detected from a distance of as far as 70 times its own diameter. This disturbance appears in the form of a signal void in MR images reflecting the presence and the location of the magnetic particle.

Compared to the nanofabricated contrast agents (superparamagnetic particles) used in MRI, micrometer-sized agents can benefit from higher magnetic moments. Based on an equivalent amount of magnetic material, micrometer-sized particles have up to 50% higher relaxivity [14], creating a significantly higher visibility in MR images. The signal loss caused by magnetic microparticles forms a four-leaf clover in coronal and sagittal planes, and a circle in the transversal plane [15, 16]. Their distinct shape makes them distinguishable from their surroundings in the MR images. However, clinical applications of micron-sized magnetic particles are limited since both their size and the remanent magnetization once the magnetic field is removed would prevent to achieve the required colloidal stability.

In a previous study we showed that a micron-sized agglomeration of superparamagnetic nanoparticles can resemble the effect of a microparticle in the form of a generated signal loss and can be detected and positioned in MR images [17]. We also investigated the limit of a 1.5 T scanner in detecting these micro-agglomerations. We showed that using a typical head receiver coil, agglomerations measuring 50 μm in diameter are detectable in the images of a clinical MR scanner (Figure 6-1). Furthermore, we reconstructed a 2D synthetic microvascular network through injection of micro-agglomerations of magnetite nanoparticles and tracked them in real-time using a fast MR imaging sequence [18].

Our previous studies were limited to the reconstruction of a 2D model. In this paper, a method is proposed to expand the previous approach to allow the reconstruction of a 3D vascular network through the fast tracking of magnetic particles in MR images. Phantom experiments are used to validate the proposed technique in a 3D microvascular model.

6.3 Materials and Methods

6.3.1 Simulation study

The susceptibility artifact generated by the magnetic agents was simulated based on the echo shifting effect in gradient echo images caused by the phase accumulation at the echo time (TE). The measured signal in the presence of a background ΔB gradient in gradient recalled echo at position $\vec{r}$ is [19]:

$$S(\vec{r},t)=\int_{v}\rho(\vec{r})e^{-i2\pi\gamma G\vec{r}t-i2\pi\gamma\Delta B(\vec{r})t}dv \qquad \text{(Eq. 6-1)}$$

The proton density (ρ) was assumed to be constant. The major effect of the additional gradient is a phase shift in the spinning protons due to the term $-2\pi\gamma\Delta BTE$. ΔB is the field distribution induced by a magnetic particle that can be approximated by the magnetic field of a dipole at position $\vec{r}$:

$$\Delta B(\vec{r})=\frac{\mu_0}{4\pi}\left(3\frac{(\vec{m}.\vec{r})\hat{r}}{r^5}-\frac{\vec{m}}{r^3}\right) \qquad \text{(Eq. 6-2)}$$

where $\vec{m}$ is the magnetic moment of the particle. The presence of a background gradient is the source of two types of artifacts in MR images; echo shifting and geometrical distortion. The latter is reflected on the both gradient echo (GRE) and spin echo (SE) sequences. In our simulation model, the geometrical distortion was ignored due to its non significant effect for image resolutions higher than 200 μm [16].

The images were calculated for a coronal plane with a slice thickness of 5 mm and a pixel spacing of 0.5 mm. Echo time was set to 2.6 ms. Particles' diameter was set to 150 μm. Based on the typical magnetization curve of Magnetite particles, it was assumed that the microparticles were saturated at the magnetic field strength of 1.5 T.

A 3D vascular network was arbitrarily created using random spatial coordinates. The generated network fit in a field of view of 4×4×4 cm^3 and included three levels of bifurcations and two branches at each bifurcation level (Figure 6-2C). A multi-slice multi-acquisition experiment was performed.

Six random coordinates were generated within the vascular network as the positions of the magnetic particles. According to the equations 1 and 2, the artifact volumes were simulated at the random generated coordinates in a 3D space. The volumes represented the magnetic field inhomogeneity caused by magnetic particles when subjected to B_0.

Subsequently, coronal slices spaced at 5 mm within the FOV were considered. The intersection of a slicing plane and 3D volume(s) correspond to the form of the artifact in MR images. A complete signal loss having the shape of a four-leaf-clover indicates the presence of a particle in the imaging plane. Figure 6-2A shows the particles randomly distributed over the vascular network and the intersection of a coronal slice within the vascular network. The form of the artifacts on the corresponding slice as they appear in MR images of a GRE sequence is shown in figure 6-2B.

The position of the artifact reflects the exact position of the magnetic particles. Center Of Gravity (COG) is an estimate of the center of a moving object with a sub-pixel precision [20].The in-plane locations of the particles were determined based on the COG of the artifacts. The coordinates representing the particles' positions were calculated based on the weighted average of the pixel's position (X_k) in the field of view, whereas, the intensity of each pixel (I_k) was used as the weighting factor ($\sum_k X_k I_k \Big/ \sum_k I_k$). The location of the slice including the artifact represents the position of the particle on the third dimension perpendicular to the imaging plane. The experiment was repeated 10 times and at each time the particles were randomly distributed within the vascular network (multi-acquisition). The particles at each acquisition were positioned through 8 slices within the FOV (multi-slice).

The reconstructed points were compared with the generated vascular network to calculate the measurement error (Figure 6-2C). Figure 6-3 depicts a diagram of the steps performed by the algorithm. The mean measurement error on all axes was 0.425 ± 0.061 mm. It was found that the positioning error on the third dimension (axis perpendicular to the imaging slice) was nearly twice as high as on the imaging plane axes. The difference is due to the limitation in setting the slice thickness less than a certain limit as a result of a significant drop in the signal to noise ratio. The slice thickness is a trade-off between the imaging resolution and the signal to noise ratio.

6.3.2 Phantom experiments and results

A 3D vascular network was fabricated from glass using the glassblowing technique. The outer and inner diameters of the channels were 4 and 2 mm, respectively. The vascular network was designed to have an inlet channel branching into eight smaller channels in a three-stage division. The dimension of the network was 7×7×3 cm^3 (Figure 6-4).

Nanometer-sized magnetic particles do not generate a distinct signal loss with an identified form (a four-leaf clover in coronal and sagittal planes and a circle in transversal planes) in MR images due to their low magnetic moments. In order for the nanoparticles to create sufficient disruption in the magnetic field and become detectable in MR images, micrometer-sized agglomerations (~200 µm) of Magnetite (Fe_3O_4) nanoparticles were generated. Iron-oxide nanoparticles are of great interests for MR imaging owing to their superior biocompatibility and greater sensitivity in nanomolar range compared to gadolinium complexes which make them interesting T_2 contrast agents [21]. The surface of these particles can be modified by organic materials such as polymers for different treatments or prognosis applications [22].

An oil-based ferrofluid (*Ferrotec*) solution made of Magnetite nanoparticles was used to generate small magnetic entities. The ferrofluid contained 10% Magnetite, 10% oil soluble dispersant and 80% oil-based carrier fluid. The magnetic moment of the particles was measured using a vibrating sample magnetometer (*EV9, Microsense*). The saturation magnetization was measured at 68 emu/g and the hysteresis curve confirmed that the particles were saturated at 1.5 T. Ferrofluid droplets were generated through a T-junction geometry included at the entry of the network. Oil in water emulsion consists of oil phase droplets dispersed in an external aqueous continuous phase. The continuous phase consisted of water, Sodium Dodecyl Sulfate (SDS) (0.1 wt %) to stabilize the formed droplets [23] and Glycerol (39 wt %) to mimic the blood viscosity [24]. The continuous phase was injected at 300µL/min using a syringe pump (*Harvard Apparatus, Holliston, MA, model PHD 2000*). The dispersed phase was injected through a plastic needle and a 1mL capacity syringe while the MRI sequence was running. The flow velocity in the 2 mm channels was at 0.21 cm/s.

Imaging was performed using a 1.5 T scanner (*Magnetom Avanto, Siemens, Erlangen, Germany*) and an 8-channel standard head coil. The injected micro-agglomerations of Magnetite particles were tracked in real-time in the vascular network using a fast imaging sequence with steady-state precession (True FISP). Parameters were set as: imaging matrix = 256×256, pixel spacing = 0.78×0.78 mm^2, TR = 4.32 ms, TE = 2.16 ms, slice thickness = 3.6 mm, flip angle = 70°, number of slices = 17, number of measurements = 16.

In order to compensate for the lack of resolution on the axis perpendicular to the imaging plane, observed in the simulation study, the experiment was performed twice for two different imaging planes: coronal and transversal. Considering the MRI's world coordinate system, stacks of coronal and transversal images lack resolution on the y and z axis, respectively, for the 3D reconstruction of a vascular network. Addition of the coordinates obtained from the two stacks can complete the missing information.

A T_1- weighted GRE sequence (flash 3D) was performed to obtain a 3D representation of the vascular network to serve as the reference image. The 3D image was used to calculate the measurement error of the 3D reconstruction. The parameters of the sequence were set as follows: voxel dimension = 256×512×128, pixel spacing = 0.39 × 0.39 × 0.80 mm^3, TR = 22 ms, TE = 9.2 ms and flip angle = 30°.

The COGs of the artifacts were used to position the particles in each image. Figure 6-5A shows the susceptibility artifacts within multiple coronal slices at different time instants. Only a complete signal loss was considered to resemble the presence of a particle within a slice (Figure 6-5B). The acquisition sequence was repeated 16 times and at each acquisition, 17 slices were imaged. The total duration of the scan was 165.92 s (0.61 s for each slice).

All the extracted x, y and z coordinates were assembled to build up a 3D distribution of the artificial vascular network. Figure 6-6A shows the assembled data. At each segment, the points were fitted based on a 3D polynomial regression model.

The bifurcation points in the vascular network were used as a baseline to align the reconstructed vascular network onto the 3D reference image through the application of a rigid-body transformation (Figure 6-6B). The calculated points were compared with the centerline of the channels, extracted from the 3D reference image, to determine the absolute measurement error (x_{real} - $x_{measured}$).

As shown in figure 6-7A, the vascular network was divided into 20 segments and the measurement errors were calculated separately for each segment. Figure 6-7B presents the average error at each segment.

In the next step, a new set of coordinates using transversal images were calculated based on the above technique and were added to the coronal slices data. Figure 6-8 shows the combined imaging planes and 3D extracted coordinates. The combined extracted coordinates were assembled to build up a 3D distribution of the artificial vascular network. Figure 6-9A shows the fitted curves calculated based on two different datasets: 1) combined coronal and transversal data and 2) coronal data only. The root mean squared errors of the fits were calculated to be 0.35 mm for the combined data versus 0.76 mm for the coronal data. The average error at each segment was recalculated based on the combined data reconstruction (Figure 6-9B).

6.4 Discussion and conclusion

The results show that the positioning errors using the images of the coronal slices are relatively higher in some particular segments (number 7, 11 and 12). The distance between two adjacent slices is limited by the signal to noise ratio (SNR). In our experiment, the slice thickness was set to 3.5 mm. As mentioned earlier, only one complete signal loss is accounted for each ferrofluid droplet expected to be present within a slice. However, when a segment or a part of it lies between two adjacent slices (segments number 2, 7, 11 and 12), it becomes challenging to visually decide whether the signal loss is complete. In order to compensate for the lack of resolution on the axis perpendicular to the coronal plane, a combination of coordinates, extracted from coronal and transversal imaging slices, was used to build up the 3D vascular network. As it is shown in figures 6-7B and 6-9B, the combination of the coordinates led to a decrease in the mean measurement error at each segment. The decrease was more significant in the segments where a relatively high positioning error was observed using the coronal data only. The fitted data using a combination of the coronal and transversal data showed to have a higher goodness-of-fit value than the ones using the coronal data only.

The positioning error can also be reduced by the injection of uniform droplets of ferrofluid. In this case, prior to the experiment, a template of a complete signal loss shall be prepared based on the dimension of the droplets. Accordingly, only the signal losses having a high correlation with the template are to be taken into account [25].

We generated micron-sized drops of oil-based ferrofluid in water by injecting the ferrofluid in a water-based continuous flow in the presence of surfactant. Through their known shape of signal loss, ferrofluid drops were discreetly detectable in the images. Ferrofluid was hand-injected during the imaging sequence through a plastic needle. As a result, the generated drops were non-uniform in size and the size of the artifacts varied in the images. Positioning precision is higher for smaller artifacts [26]. Therefore, the size of the particles is a trade-off between the visibility of the signal loss and the positioning accuracy.

Balanced steady-state gradient recalled echo (True FISP) is a fast sequence that achieves a scanning time of ~0.5 s per image with a high SNR and a high sensitivity to field inhomogeneity. This sequence was exploited in our experiment as it has the highest specificity for detection of Magnetite particles as well as a high temporal resolution. Unlike GRE sequences, True FISP is not sensitive to the background field inhomogeneities induced by poor shimming, presence of blood, etc. This advantage of True FISP is owing to the refocusing of the background resulting in a SE- like insensitivity to the background gradient field inhomogeneity [27, 28].

In our previous study, dynamic tracking of the micro-agglomerations of Magnetite nanoparticles, measuring 10 ± 2 nm in diameter, was used to reconstruct a 2D vascular network of 150 μm in diameter [18]. Nevertheless, the glass blowing technique used did not support 3D fabrication of a vascular network at such similar scale and therefore, the proposed algorithm was validated in a 3D vascular network at an altered millimeter scale.

Water in oil emulsions composed of iodized oil and an aqueous solution carrying anticancer medications are wildly used in the treatment of the hepatic tumors [29]. Oil-based ferrofluid has never been tested in-vivo as a contrast agent and its clinical applicability remains to be validated.

SPIOs have several characteristics turning them to interesting contrast agents; they benefit from biocompatibility, they have a long circulating half-life and they are easily cleared from the blood circulation through the reticuloendothelial system [30]. However, they do not possess the highest saturation magnetization among the superpamagnetic nanoparticles. The size of the signal void created as a result of presence of a magnetic particle is directly proportional to the saturation magnetization of the particles. Iron-cobalt nanocrystals with graphitic carbon have the highest magnetization among all magnetic materials making them an interesting alternative to SPIOs [9]. Owing to superior magnetic properties, the application of these particles to the proposed technique can lead to visualization of smaller vessels. Nevertheless, due to the easy oxidation and the potential toxicity, their clinical applications remain to be confirmed.

In arterioles of 10 to 200 μm in diameter, blood velocity varies between 0.1 and 0.5 cm/s. We tried to reproduce a velocity of a similar magnitude in the channels (~0.21 cm/s). Form of the signal void derived from a moving particle at this relatively low velocity is not significantly altered. The blood velocity in the human body reaches 5 cm/s in small arteries and 10 cm/s in the larger ones. Shape of the signal loss obtained from a particle traveling at higher velocities could be completely distorted. In order to track the particles at the arterial level, the blood velocity can be reduced using a temporary balloon occlusion.

In conclusion, a method for 3D reconstruction of a microvascular network using a clinical MR scanner, typical head coil and sequence parameters, was proposed. The technique was tested in a phantom model. It was shown that the elevated positioning error on the third dimension can be compensated by combining the reconstructed points generated by the scans of at least two different spatial planes. The results suggest that the method can be used for the reconstruction of vascular networks beyond the spatial resolution of the scanner.

Acknowledgment

The project was supported in part by the National Science and Engineering Research Council of Canada (NSERC) and Fonds Québécois de la Recherche sur la Nature et les Technologies (FQRNT), and in part by the Research Chair of Polytechnique Montréal in Nanorobotics. The authors would like to thank Cédric Ginart for the fabrication of the glass made vascular network.

References

[1] S. Martel*, et al.*, "Automatic navigation of an untethered device in the artery of a living animal using a conventional clinical magnetic resonance imaging system," *Applied Physics Letters,* vol. 90, Mar 12 2007.

[2] P. Pouponneau, J.C. Leroux, G. Soulez, L. Gaboury, S. Martel, "Co-encapsulation of magnetic nanoparticles and doxorubicin into biodegradable microcarriers for deep tissue targeting by vascular MRI navigation," *Biomaterials,* vol. 32, p. 3481, May 2011.

[3] P. Pouponneau, G. Soulez, G. Beaudoin, J.C. Leroux, S. Martel, "MR Imaging of Therapeutic Magnetic Microcarriers Guided by Magnetic Resonance Navigation for Targeted Liver Chemoembolization," *Cardiovascular and Interventional Radiology,* vol. 37, pp. 784-790, Jun 2014.

[4] M. Spahn, "X-ray detectors in medical imaging," *Nuclear Instruments & Methods in Physics Research Section a-Accelerators Spectrometers Detectors and Associated Equipment,* vol. 731, p. 57, Dec 11 2013.

[5] A. Bozzao,R. Floris, M. Pocek, F. Fasoli, F. G. Garaci, G. Simonetti, "[Non-invasive assessment of epiaortic vessels. Comparison of magnetic resonance angiography with gadolinium, spiral computerized tomography angiography, and digital angiography]," *Radiol Med,* vol. 101, pp. 48-53, Jan-Feb 2001.

[6] M. A. O'Reilly and K. Hynynen, "A super-resolution ultrasound method for brain vascular mapping," *Medical Physics,* vol. 40, Nov 2013.

[7] A. P. Tregaskiss, A. N. Goodwin, L. D. Bright, C. H. Ziegler, R. D Acland, "Three-dimensional CT angiography: A new technique for imaging microvascular anatomy," *Clinical Anatomy,* vol. 20, pp. 116-123, Mar 2007.

[8] T. Wittlinger, I. Martinovic, A. Moritz, S. Romanzetti,"Evaluation of the spatial resolution with 1.5-4 tesla in a stenosis model," *Asian Cardiovasc Thorac Ann,* vol. 14, pp. 387-93, Oct 2006.

[9] J. H. Lee, "High-Contrast In Vivo Visualization of Microvessels Using Novel FeCo/GC Magnetic Nanocrystals (vol 62, pg 1497, 2009)," *Magnetic Resonance in Medicine,* vol. 63, pp. 1723-1723, Jun 2010.

[10] N. Petridou, et al., "Pushing the limits of high-resolution functional MRI using a simple high-density multi-element coil design," Nmr in Biomedicine, vol. 26, pp. 65-73, Jan 2013.

[11] E. Laistler, Poirier-Quinot M, Ginefri JC, Lambert S, Dubuisson RM, and M. E. Boriasse E,

Darrasse L, "Sub-nanoliter microscopic MR imaging of the human skin in vivo using a 12 mm superconducting surface coil at 1.5 Tesla. P," *ISMRM, Honolulu, USA,* p. 4758, 2009.

[12] E. Laistler, R. Loewe, E. Moser, "Magnetic resonance microimaging of human skin vasculature in vivo at 3 Tesla," *Magn Reson Med,* vol. 65, pp. 1718-23, Jun 2011.

[13] N. Olamaei, F. Cheriet, G. Beaudoin, S. Martel, "MRI visualization of a single 15 mu m navigable imaging agent and future microrobot," *2010 Annual International Conference of the Ieee Engineering in Medicine and Biology Society (EMBC),* p. 4355, 2010.

[14] K. A. Hinds*, et al.*, "Highly efficient endosomal labeling of progenitor and stem cells with large magnetic particles allows magnetic resonance imaging of single cells," *Blood,* vol. 102, pp. 867-72, Aug 1 2003.

[15] E. M. Shapiro, S. Skrtic, K. Sharer, J. M. Hill, C. E. Dunbar, A. P. Koretsky, "MRI detection of single particles for cellular imaging," *Proceedings of the National Academy of Sciences of the United States of America,* vol. 101, p. 10901, Jul 27 2004.

[16] G. Zabow, S. J. Dodd, E. Shapiro, J. Moreland, A. P. Koretsky, "Microfabricated high-moment micrometer-sized MRI contrast agents," *Magnetic Resonance in Medicine,* vol. 65, pp. 645-55, Mar 2011.

[17] N. Olamaei, F. Cheriet, S. Martel, "Magnetic resonance imaging of microvessels using iron-oxide nanoparticles," *Journal of Applied Physics,* vol. 113, p. 124701, Mar 28 2013.

[18] N. Olamaei, F. Cheriet, S. Deschênes, S. Martel, "Dynamic tracking of magnetic nanoparticles for mapping microvascular networks using a clinical 1.5 T magnetic resonance scanner," *Applied Physics Letters,* vol. 104, May 26 2014.

[19] B. R. W. Haacke E.M, Thompson M. R and Venkatesan R, "Magnetic Resonance Imaging " 1999 1999.

[20] Y. Ivanov and A. Melzer, "Particle positioning techniques for dusty plasma experiments," *Review of Scientific Instruments,* vol. 78, p. 33506, Mar 2007.

[21] J. W. M. Bulte and D. L. Kraitchman, "Iron oxide MR contrast agents for molecular and cellular imaging," *Nmr in Biomedicine,* vol. 17, pp. 484-499, Nov 2004.

[22] W. Wu, Q. G. He, C. Z. Jiang, "Magnetic Iron Oxide Nanoparticles: Synthesis and Surface

Functionalization Strategies," *Nanoscale Research Letters,* vol. 3, pp. 397-415, Nov 2008.

[23] J. H. Xu, S. W. Li, J. Tan, Y. J. Wang, G. S. Luo, "Preparation of highly monodisperse droplet in a T-junction microfluidic device," *Aiche Journal,* vol. 52, p. 3005, Sep 2006.

[24] M. Y. Yousif*, et al.*, "A blood-mimicking fluid for particle image velocimetry with silicone vascular models," *Experiments in Fluids,* vol. 50, pp. 769-774, Mar 2011.

[25] K. Belharet, et al., "MRI-based microrobotic system for the propulsion and navigation of ferromagnetic microcapsules," *Minimally Invasive Therapy & Allied Technologies*, vol. 19, pp. 157-169, Jun-Aug 2010.

[26] N. Olamaei, et al., "Accurate positioning of magnetic microparticles beyond the spatial resolution of clinical MRI scanners using susceptibility artifacts," *2011 Annual International Conference of the Ieee Engineering in Medicine and Biology Society* (Embc), pp. 2800-2803, 2011.

[27] R. M. Lebel*,* D. W. Holdsworth, T. L. Poepping, "Relaxometry model of strong dipolar perturbers for balanced-SSFP: application to quantification of SPIO loaded cells," *Magn Reson Med,* vol. 55, pp. 583-91, Mar 2006.

[28] A. R. Mohammadi-Nejad*,* G. A. Hossein-zadeh, H, Soltanian-zadeh, "Quantitative evaluation of optimal imaging parameters for single-cell detection in MRI using simulation," *Magn Reson Imaging,* vol. 28, pp. 408-17, Apr 2010.

[29] H. Demachi*,* O. Matsui, H. Abo, H.Tatsu, "Simulation model based on non-newtonian fluid mechanics applied to the evaluation of the embolic effect of emulsions of iodized oil and anticancer drug," *Cardiovasc Intervent Radiol,* vol. 23, pp. 285-90, Jul-Aug 2000.

[30] T. K. Jain*,* M. K. Reddy, M. A. Morales, D. L. Leslie-Pelecky, V. Labhasetwar, "Biodistribution, clearance, and biocompatibility of iron oxide magnetic nanoparticles in rats," *Molecular Pharmaceutics,* vol. 5, pp. 316-327, Mar-Apr 2008.

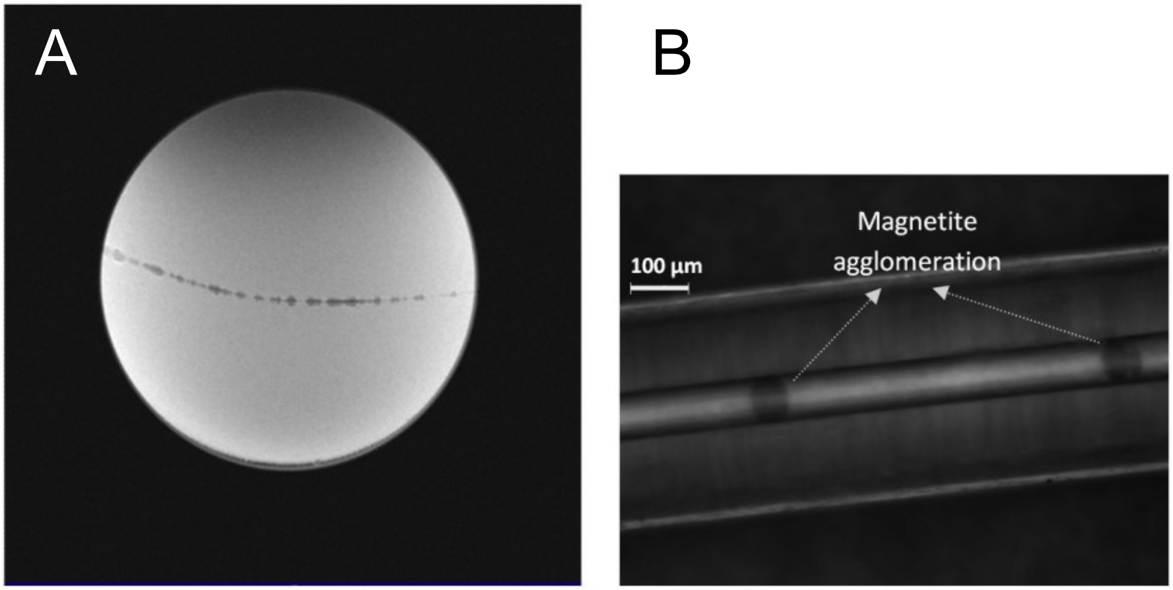

Figure 6-1: Clinical MRI (left) and microscopic (right) images of a capillary with an inner diameter of 50 µm injected by agglomerations of Magnetite particles.

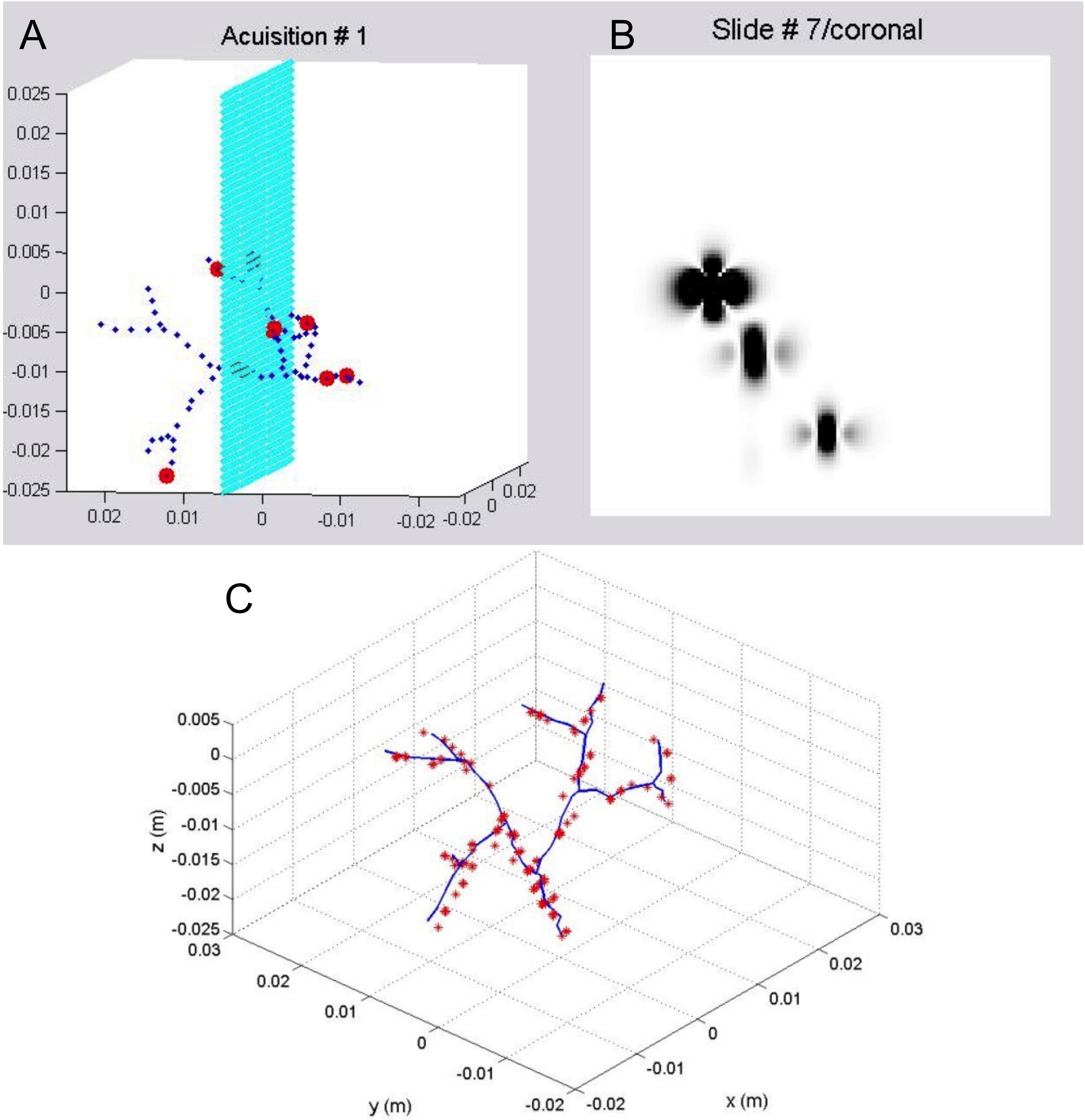

Figure 6-2: Random distribution of the magnetic particles (circles) on the vascular network (dotted lines) and their intersection with a coronal slice (A), form of the artifacts on the corresponding slice as they appear in MR images of a GRE sequence (B). Reconstructed points (×) and the simulated vascular network using coronal slices (C).

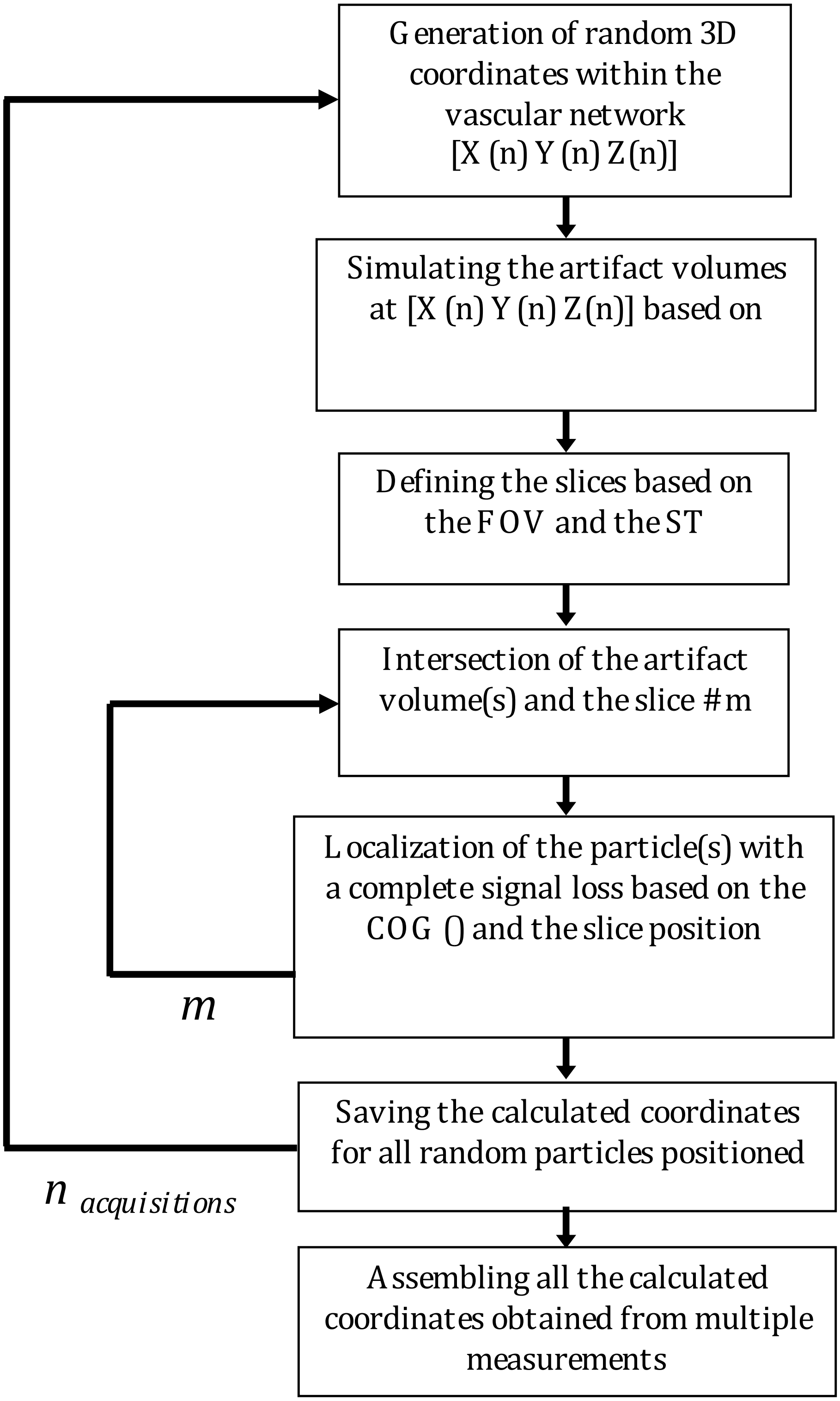

Figure 6-3: Diagram of the steps performed in the simulation of a multi-slice, multi-acquisition MR imaging of a vascular network.

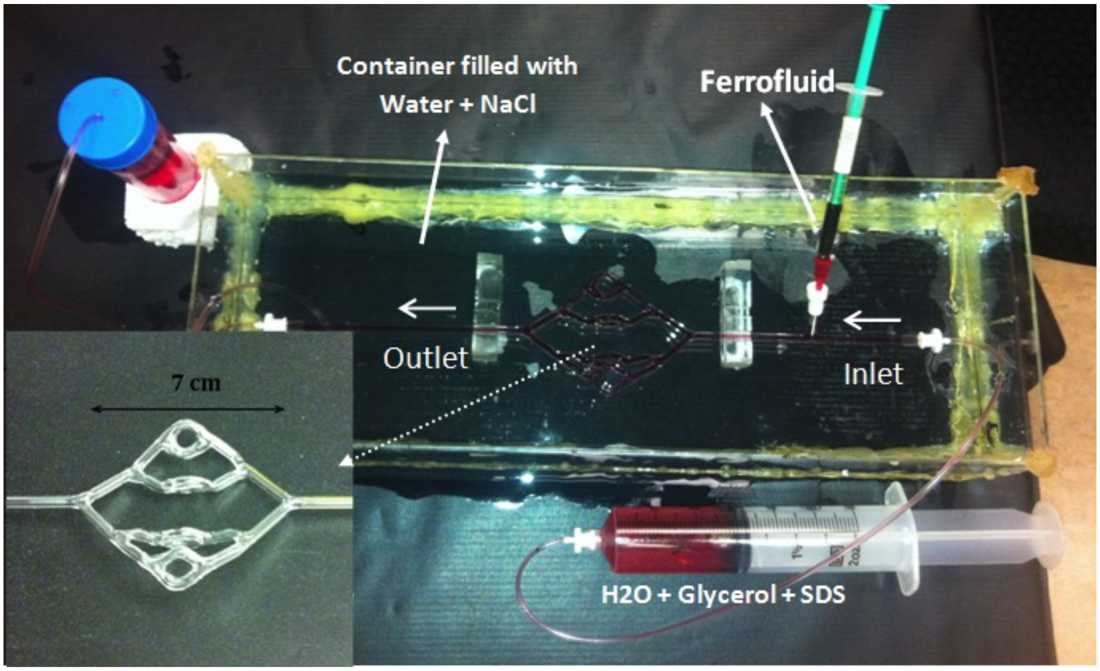

Figure 6-4: Experiments setup; suspended vascular network in a container filled with water and Sodium Chloride. The continuous phase (water, Glycerol and SDS) and ferrofluid are injected through the T-junction prior to the network's inlet.

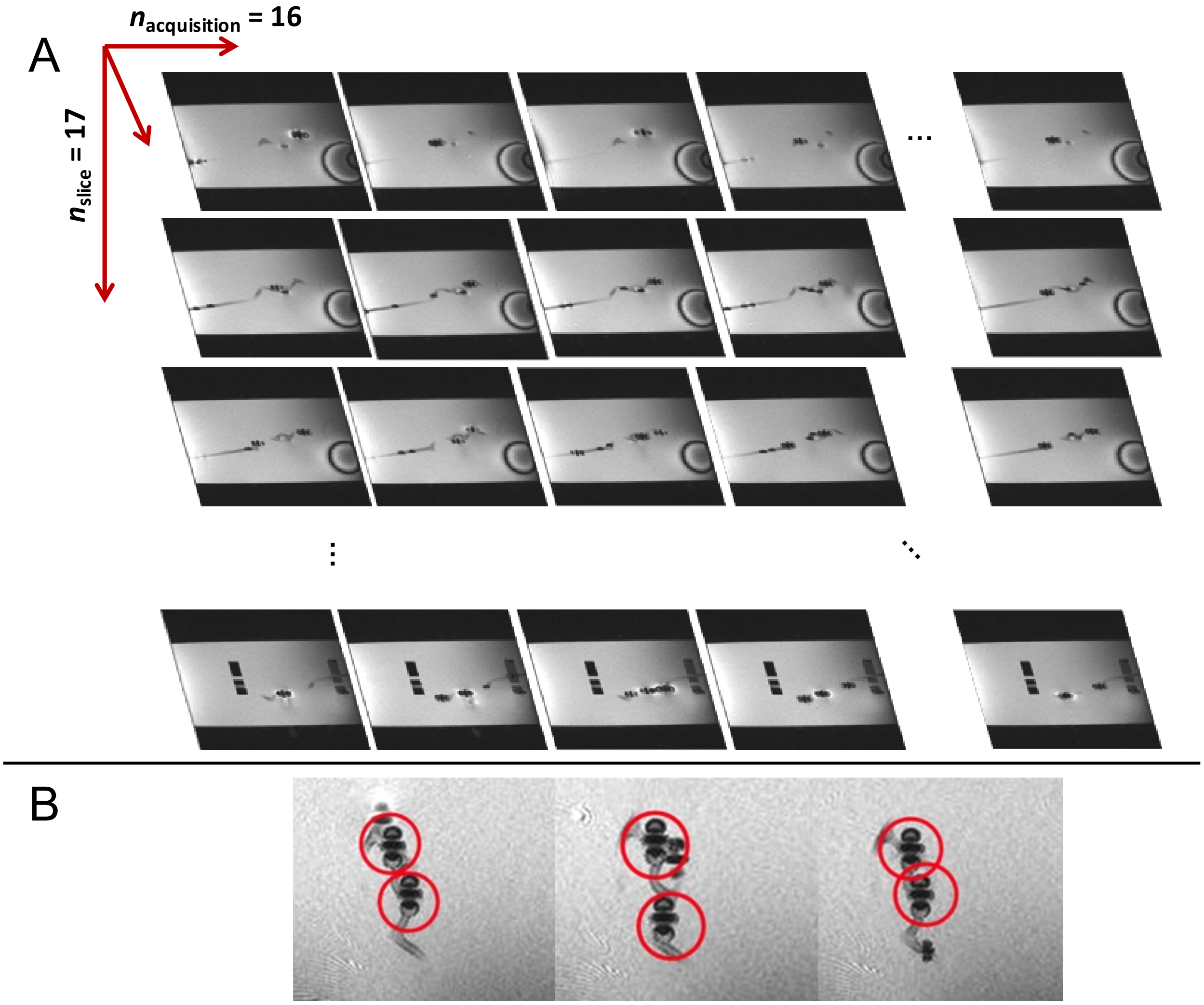

Figure 6-5: Susceptibility artifacts within multiple coronal slices at different time instants with the following imaging parameters: imaging matrix= 256×256, pixel spacing= 0.7813×0.7813 mm^2, TR = 4.32 ms, TE = 2.16 ms, slice thickness = 3.6 mm, and flip angle = 70˚ (A). Complete signal losses (circled artifacts) were considered to resemble the presence of a particle within the imaging slice (B).

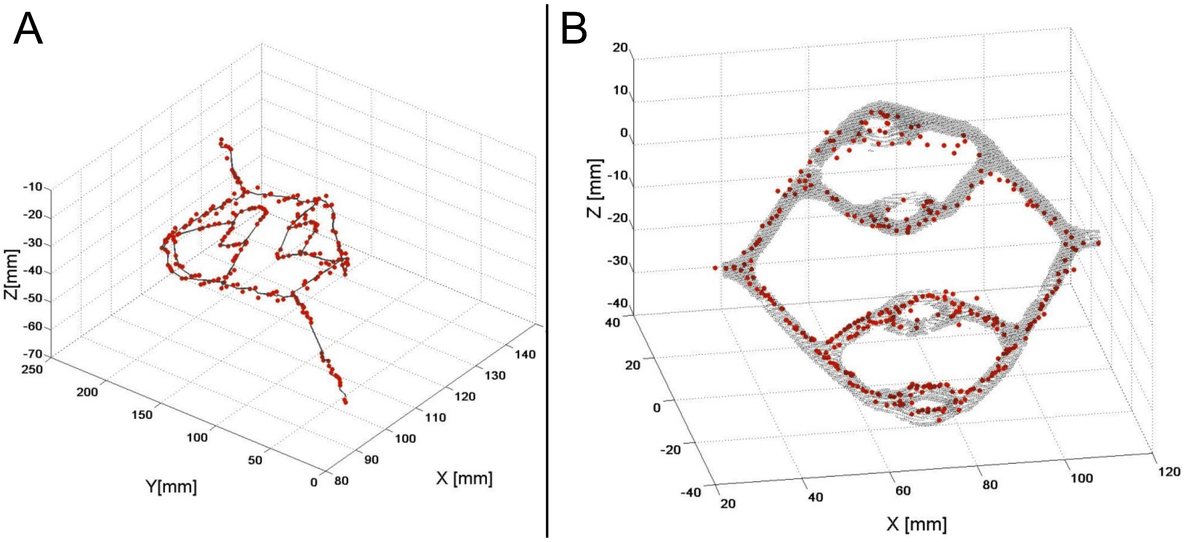

Figure 6-6: 3D reconstructed points (●) through the localization of the micro-agglomerations of Magnetite particles at 16 different acquisitions and 17 different slices. The points at each segment were fitted (solid line) based on a polynomial regression model in three dimensions (A). The measured points (●) superposed over the 3D reference image obtained from a 3D scan with the following parameters: Imaging volume = 256×512×128, pixel spacing = 0.39×0.39×0.80 mm^3, TR = 22 ms, TE = 9.2 ms and flip angle = 30˚ (B).

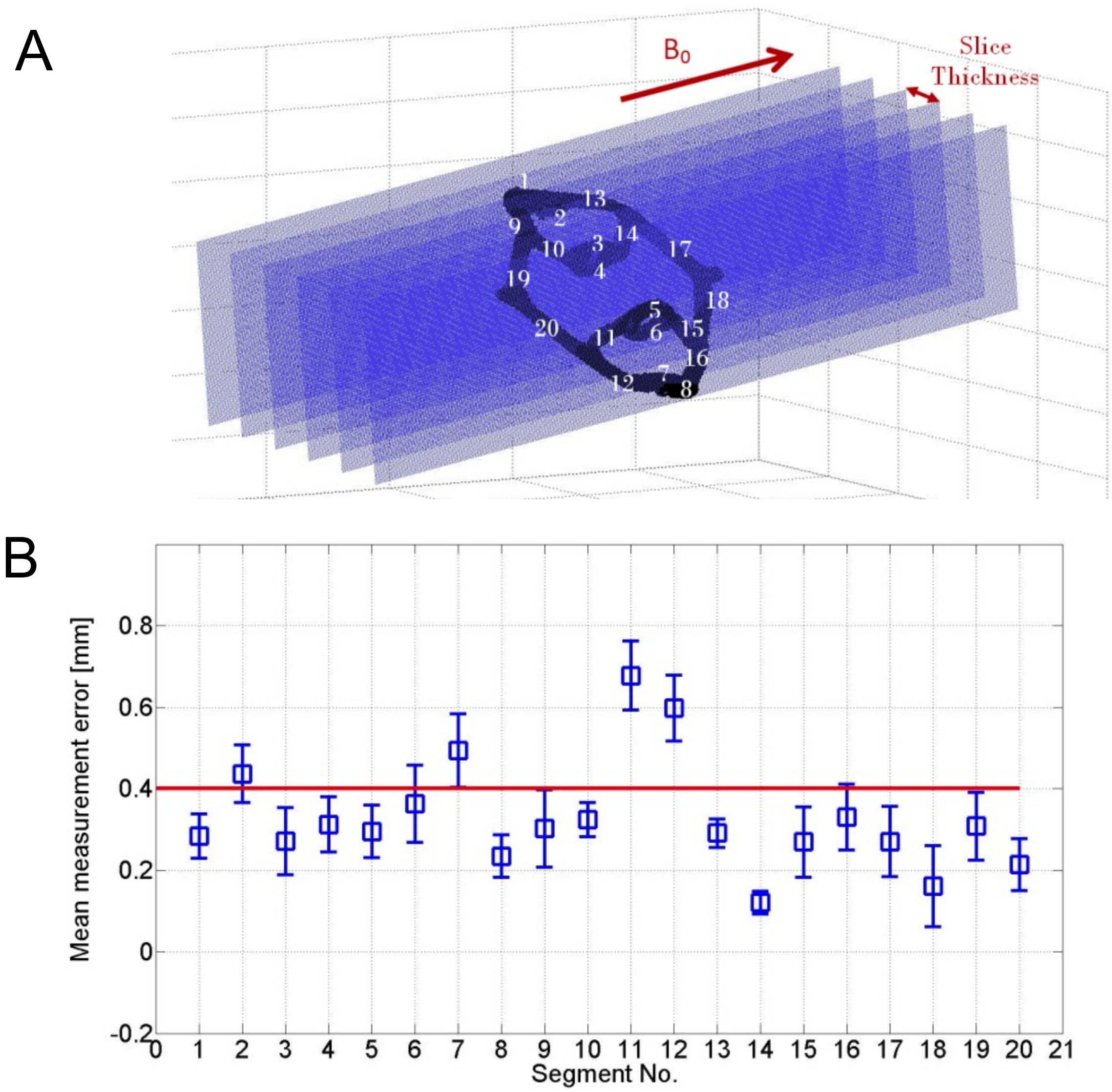

Figure 6-7: The distribution of the segment numbers and how the network is positioned in relation to the imaging coronal planes (A). Mean measurement error and the standard deviation for each segment based on coronal planes data (B).

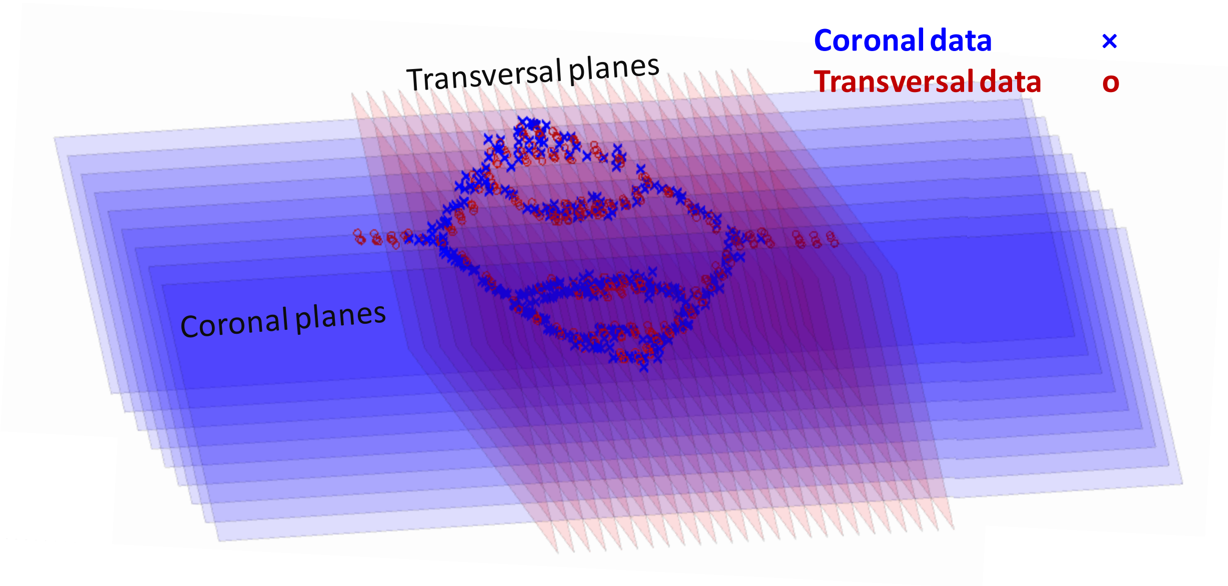

Figure 6-8: Combined imaging planes and 3D coordinates extracted from coronal and transversal imaging planes.

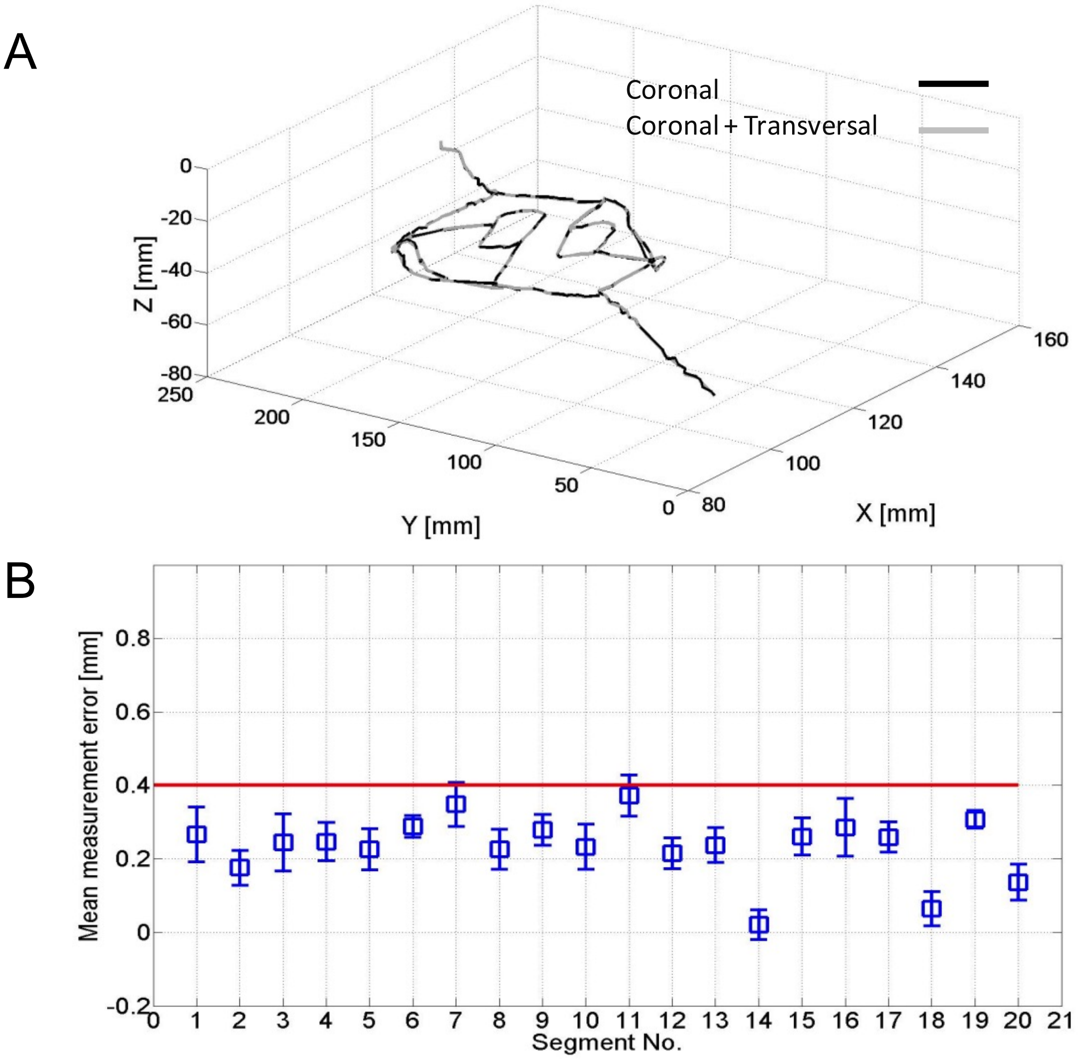

Figure 6-9: The coronal data (black) and the combined coronal-transversal data (gray) were fitted at each segment based on a polynomial regression model in three dimensions (A). Mean measurement error and the standard deviation for each segment based on the combined coronal-transversal data (B).

CHAPTER 7 COMPLEMENTARY RESULTS

Phantom experiments required the utilization of microfluidic channels mimicking the microvascular networks. Contrast agents (ferrofluid droplets) were also developed using a T-junction microfluidic device. The combination created an integrated microfluidic device including a vascular network, a T-junction geometry and a tortuous reservoir to collect the generated droplets. The integrated microfluidic device was fabricated on Plexiglas using a micro-milling machine. This chapter presents details of the fabrication process.

7.1 Fabrication of microchannels

The experimental vascular networks were fabricated on Plexiglas (PMMA) using a circuit-board plotter machine (LPKF Protomat 95S/II) and a multi press machine (LPKF Multipress II) for high pressure thermal sealing.

The vascular network's map was designed and plotted using LPKF CircuitCAM PCB software (Figure 7-1). The software is used for creating the design data required for the LPKF milling machine. The output is an LMD file, readable by the LPKF PCB machine.

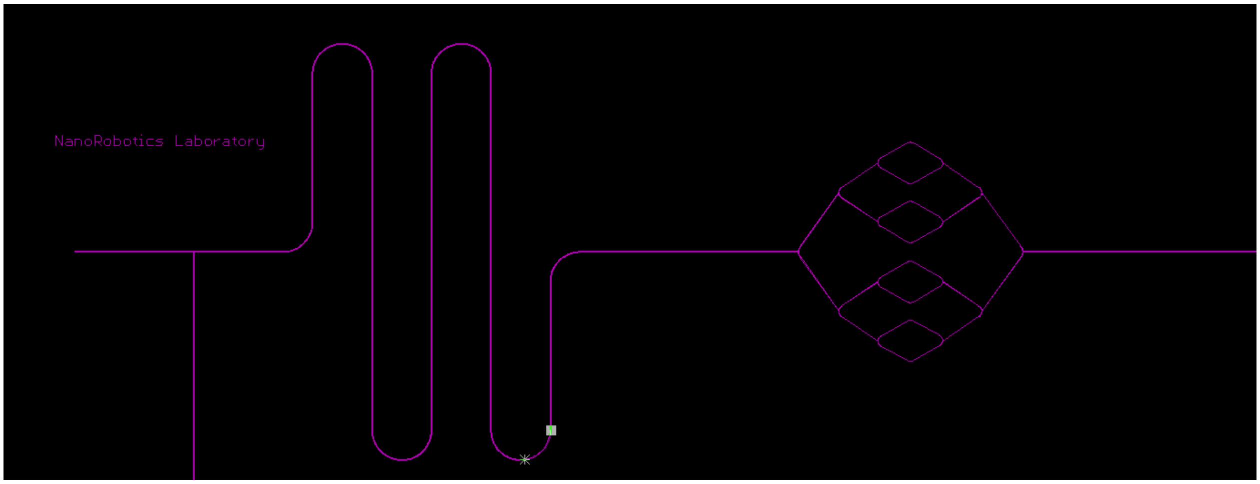

Figure 7-1: The design of the vascular in the CircuitCAM software.

The constituent segments of the pattern were milled. The mills were automatically selected by the machine according to the size of the channels defined in the plot. A PMMA top layer including built-in holes was used to seal the milled PMMA layer. Once the two PMMA pieces were aligned, a press machine was used to assemble and seal the contact area (Figure 7-2). The temperature and the pressure were set to 105˚C (glass transition temperature of PMMA) and 140 N/cm^2, respectively. Total duration of the cure was 60 min.

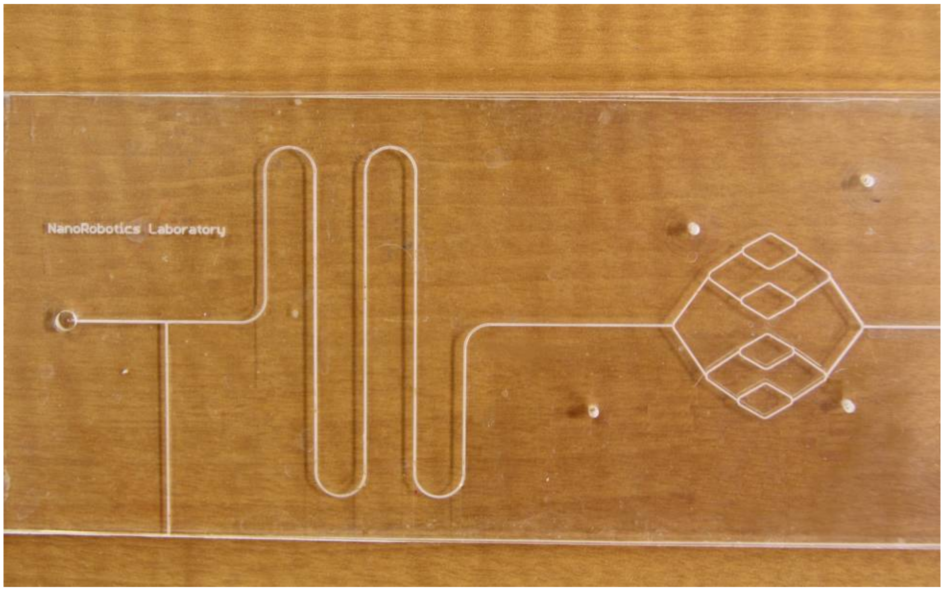

Figure 7-2: The final milled PMMA sealed in the press machine.

7.2 Formation of microagglomerations through a T-junction geometry

A T-junction geometry was integrated in the design to generate droplets of oil-based ferrofluid in water. Successful generation of the droplets and fluidity of their movement in the channels depend on the wetting property of the channels' surface (Figure 7-3).

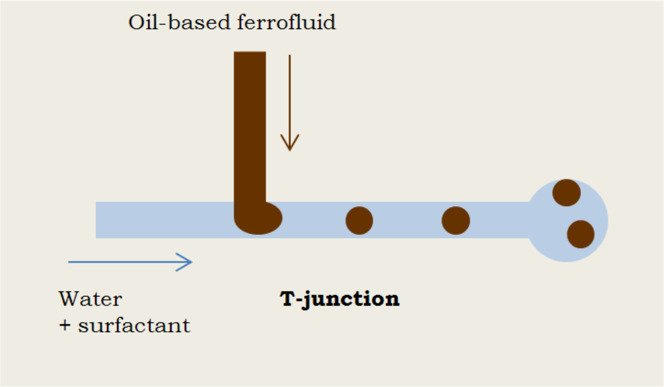

Figure 7-3: Formation of undefined oil droplets in water in a T-junction geometry with hydrophilic channels.

PMMA's surface is highly hydrophobic. However, formation of unconfined oil-in-water droplets necessitates a hydrophilic surface. In order to inverse the wetting property of the PMMA, surface of the channels as well as their mirror pattern on the top layer were coated by Silicon dioxide, also known as Silica (SiO_2) (Figure 7-4). Silica has a high hydrophilic characteristic. A thin layer of Silica (~ 50 nm) was deposited using a Boxer coating system (*Leybold Optics*).

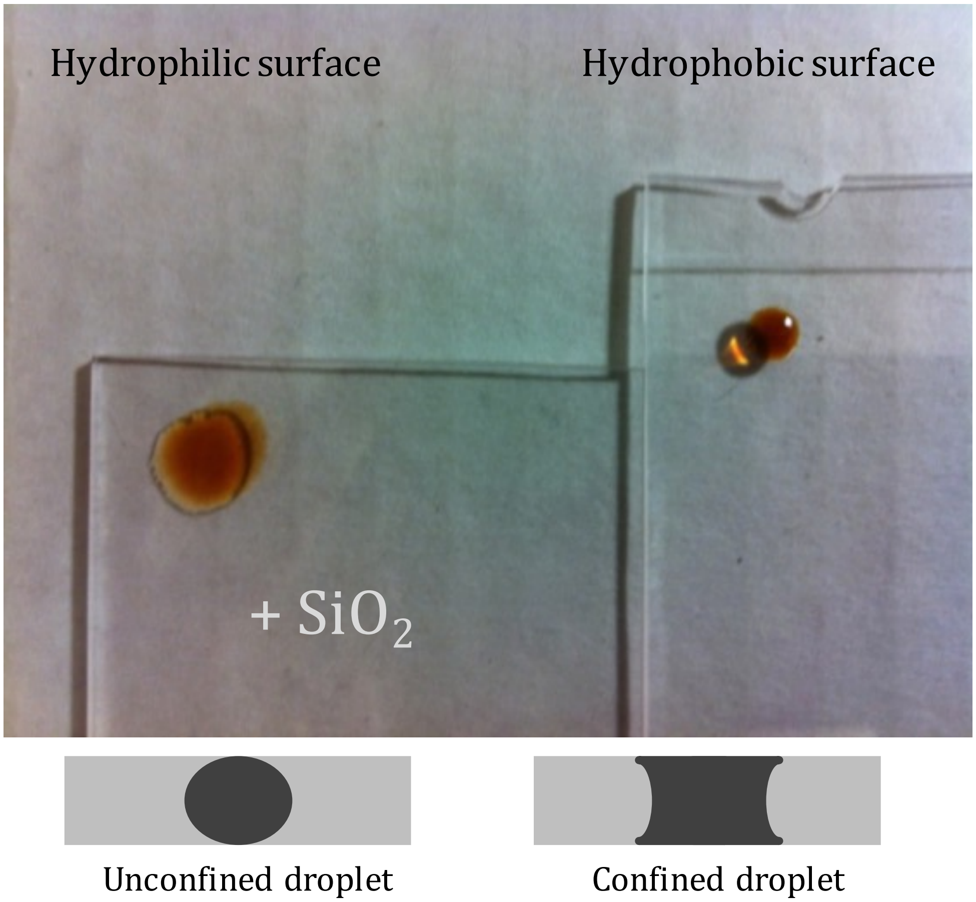

Figure 7-4: Impact of silica coated PMMA on the wetting property of the surface.

In order to coat the channels' surface solely and avoid the negative impact on the assembly of the top and bottom layers, prior to the coating process a protection mask was laid on both PMMA layers. The protection mask was as well a PMMA based layer fabricated by the PCB machine (Figures 7-5 and 7-6). They were removed after the silica treatment process.

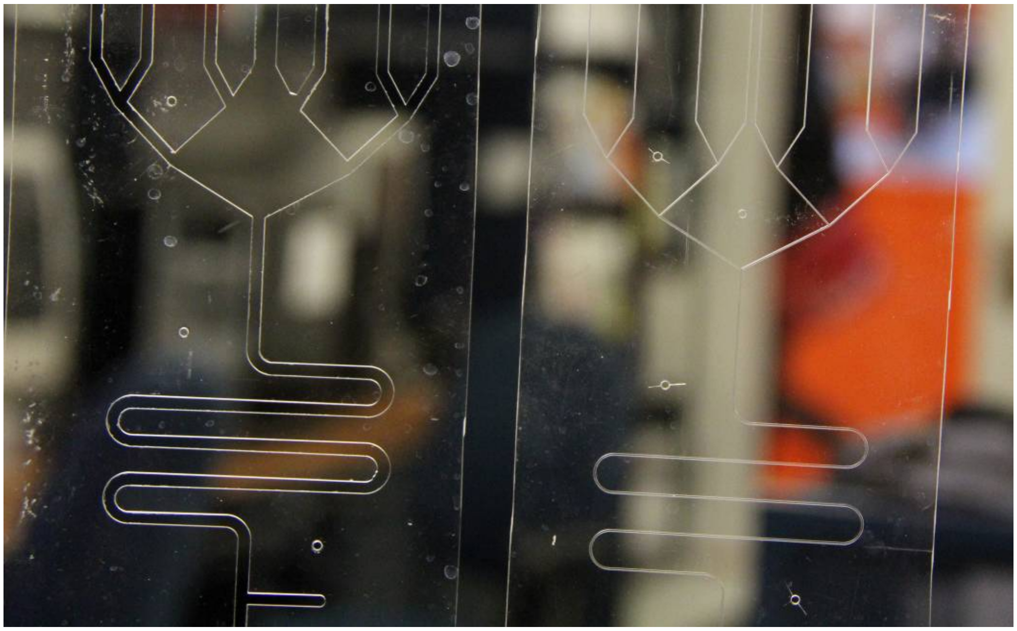

Figure 7-5: A milled PMMA and its mask to exclusively expose channels to the Silica treatment.

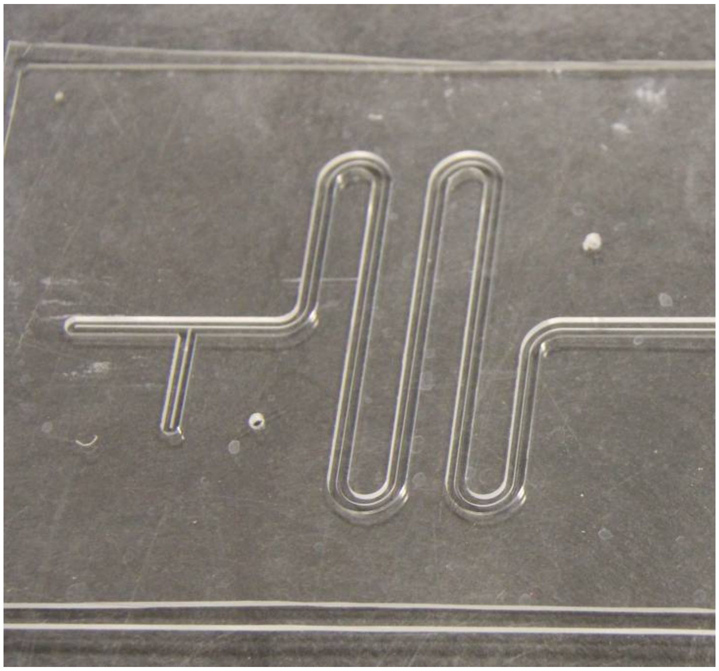

Figure 7-6: A milled PMMA with exposed channels' surface prior to Silica coating.

CHAPTER 8 GENERAL DISCUSSION

MRI is a versatile imaging modality that allows for 3D assessments of tissue morphology, metabolism and physiology. The recent advances in the MRI technology including creation of more powerful gradient systems, advanced receiver coils and development of new contrast agents has led to faster image acquisitions with higher resolution and sensitivity. In this study, we present the application of micron-sized agglomerations of iron-oxide nanoparticles in the visualization of microvessels. We studied behaviors of the susceptibility artifact in the images acquired by the clinical MR scanners

In previous studies pre-clinical scanners were used to detect single particles (~ 1µm in diameter) for cellular and molecular imaging purposes [108, 109, 113, 114]. Recognition of signal cells using a 1.5 T scanner has been reported through the application of custom-built solenoidal RF coils and/or custom gradient coils with an inner diameter of 11 cm and a maximum gradient of 600 mT/m [115]. However, such instrumentations cannot be used for clinical applications. In-vivo visualization of single cells at 1.5 T can also be achieved by using high-temperature superconducting surface coils measuring 12 mm in size. Such RF coils produce images with a very limited FOV (~ 1 cm^2) [101]. Therefore, lack of spatial resolution and/or penetration depth limits the application of clinical scanners in detection of magnetic microparticles in the human's organs. We performed our studies using a 1.5 T MR scanner and a commercial head coil. The images were acquired over a rather large FOV. It was confirmed that a 15 µm particle and a 50 µm agglomeration of iron-oxide nanoparticles is visible using a fast steady state sequence acquired from a clinical 1.5 T MR scanner (TrueFISP). We proposed real-time tracking of the magnetic particles to obtain their travel trajectory through a fast imaging sequence. Assembling all the trajectories allowed for the reconstruction of the local microvasculature which is a complementary step in the MRN.

In our preliminary study (Appendix A) it was shown that a single 15 µm ferromagnetic particle is visible in the GRE images of a clinical MR scanner. However, the remanent magnetization of the ferromagnetic particles once exposed to a magnetic field prevents their application as contrast agents in the MRI. Moreover, their rather large size is a limiting factor in clearance from the body. On the other hand, owing to the macrophage process in the reticuloendothelial system, superparamagnetic nanoparticles are easily cleared from the body. Furthermore, they do not retain any net magnetization upon removal from the magnetic field [31]. These characteristics along with their strong effect on the proton's relaxation time make them interesting contrast agents for the clinical applications.

Sensitivity of a clinical scanner is not sufficient to detect a single superparamagnetic particle. However, an assembly of such particles can be detected by a clinical scanner. An agglomeration of iron-oxide (Fe_3O_4) nanoparticles measuring 50 μm in diameter was visible in the images acquired by a fast susceptibility-sensitive MR sequence [116].

8.1 Agglomeration of iron-oxide nanoparticles

A microfluidic T-junction geometry was used to generate microagglomerations of nanoparticles required for the imaging experiment. The technique has previously been presented in [117-122]. Oil-in-water droplets have been generated through different microfluidic-based geometries. However, the presence of magnetic nanoparticles in the oil-based ferrofluid, creates limitations in the application of certain techniques.

An assembly of superparamagnetic nanoparticles measuring in the range of 50 μm to 200 μm cannot be obtained from the commercial market. Hence, we assessed the behavior of such particles when used for the visualization of microvessels by using an oil-based ferrofluid composed of iron-oxide nanoparticles. Although water-in-oil emulsions composed of iodized oil carrying anti-cancer drugs is used in the treatment of the hepatic tumors [123], oil-based ferrofluid has never been used clinically as a contrast agent. Therefore, the clinical application of such particles shall be subject to further studies.

This contrast micro agent generating technique was used due to several advantages and conveniences; 1) availability of oil-based or water-based ferrofluids at a low cost, 2) ease of injection, 3) accessibility to a PCB machine, 4) uniformity and monodispersity of the droplets generated and 5) an easy control over the particles' size and their spacing.

The stability of droplets' formation highly depends on the interfacial tension between the continuous phase and the microchannels' wall. Stable generation of droplets is feasible only if the continuous phase wets the channels' wall thoroughly, while the dispersed phase does not wet them at all. In our model, the continuous phase is water and the fluid to be dispersed is oil-based ferrofluid. Since the PMMA is highly hydrophobic, formation of stable oil-in-water droplets was not possible. Several techniques have been developed to inverse the wetting property of the materials. Exposure to oxygen plasma effectively increases the surface energy of the material resulting in a surface that is hydrophilic. However, this effect is temporary and, due to the contact of the treated surface to the air, it only lasts for few hours [124, 125]. Addition of a surfactant, such as SDS, into the water phase is another technique to change the wetting property of the channels' wall. Water absorbs the surfactant's polar head and, as the result, their tail is oriented towards the wall. This orientation changes the wetting property of the wall [120]. Yet, this technique failed in our experiments as it did not create the stability required for generating the oil-based ferrofluid drops in water.

Hybrid coatings containing Silica and PMMA are applied to protect metallic surfaces from corrosion [126]. Other effects on the surface are thermal stability, mechanical strength and wettability. Channels made of glass or Silicon are inherently hydrophilic making them an ideal tool for the generation of oil-in-water drops [127].

We applied Silica coating on the PMMA surface to inverse its wetting property from hydrophobic to hydrophilic. Creation of hydrophilic channel walls allowed for formation of unconfined stable ferrofluid droplets in water and as well alleviated a friction-free movement of the ferrofluid droplets in the microvascular channel.

Various microfluidic geometries are used for the formation of droplets. T-junctions are one of the most frequently used geometries. Size of the produced droplets and their spacing depend on: 1) the flow rates of the continuous and the dispersed phases, 2) the concentration of the surfactant and 3) the internal diameter of the channels. In order to achieve smaller drops we used a micro liter syringe and a needle with an internal diameter of 100 μm. In the MR imaging, a minimum distance between the droplets should be maintained so that the susceptibility effects of the individual droplets do not interfere. The spacing becomes larger as the flow rate of the continuous phase increases relative to that of the dispersed phase.

Furthermore, due to the magnetic force exerted on the magnetic volumes, presence of a magnetic field disrupts the formation of ferrofluid drops. As such, all the drops were generated outside of the MRI room and were collected in a tortuous reservoir built in the microfluidic device next to the T-junction. The droplets were propelled inside the vascular network during the imaging sequence.

In conclusion, the application of a T-junction hydrophilic geometry together with a built-in reservoir was found to be an effective method for generating stable isolated oil-based ferrofluid drops.

8.2 Iron-oxide nanoparticles as positive contrast agents

Iron-oxide nanoparticles are extensively used in MRI as negative contrast agents for different applications such as angiography, cell labeling and tracking [22, 24, 28, 35, 47]. In the presence of B_0, the nanoparticles induce inhomogeneities in the local magnetic field. This effect results in shortening of T_2 relaxation time of the protons and darkening of the MR images.

In our study, we applied a real-time tracking of the magnetic microparticles (micron-sized agglomerations of nanoparticles) as they were released in a vascular network to identify their trajectory path. The signal voids arising from the distortions in the T_2^*-weighted GRE images represent the presence and the position of the particles. They are found to be the most effective way to enhance the effect of a microparticle, the size of which is significantly inferior to the spatial resolution of the system. However, the signal voids result in an undesirable negative contrast, causing tissues with a low proton density to mask the particles. As a result, the magnetic microparticles cannot be distinguished from a void in the image.

It is possible to achieve positive contrast with superparamagnetic nanoparticles by employing T_1 weighting [128]. However, due to the predominant T_2 and spin dephasing effects of the magnetic nanoparticles, in detecting magnetic nanoparticles the T_1-weighted images are not as sensitive as the T_2-weighted counterparts [129]. Therefore, it is of a great interest to acquire T_2-weighted positive contrast images in the tissues containing superparamagnetic nanoparticles.

A variety of sequence modification-base techniques have been developed for positive contrast imaging of iron oxide nanoparticles, applying to cell tracking or real-time visualization of devices in interventional MRI. The main class of sequences are 1) frequency selective excitation [130], 2) gradient sensitive sequences [131], and 3) steady state free precession techniques [132].

In a recent study by [133], a novel and fast positive contrast technique, employing a balanced steady state pulse sequence, was presented and successfully implemented in an in-vivo cell detection experiment on a clinical MRI platform. Such applications of the steady state pulse sequence support the feasibility of an in-vivo application of our proposed technique.

8.3 Real-time imaging of magnetic particles

The fact that 180° pulses do not exist in the gradient echo sequences implies that T_2^* effects are not reversed during the sequence and as a result, compared to the SE techniques, the GRE sequences are more sensitive to the magnetic susceptibility effects. Detection of superparamagnetic iron-oxide particles has been accomplished through T_1 [134], T_2 [135] and T_2^*-weighted images [136, 137]. T_2^*-weighted GRE acquisitions provide the highest sensitivity to the presence of a superparamagnetic magnetic particle. However, their sensitivity is equally high to the other sources of susceptibility such as hemorrhage or tissue-air interfaces. This makes them less specific in the detection of iron-oxide nanoparticles. Contrarily, T_1 and T_2-weighted imaging are less sensitive and more specific in the detection of iron-oxide nanoparticles. This is due to the refocusing of the background field inhomogeneities through the SE acquisitions.

The balanced steady state free precession technique, known as True-FISP, has shown to provide the highest sensitivity to the presence of iron-oxide nanoparticles [33, 115] whereas it is not sensitive to the background inhomogeneities. [67]. The short repetition times (much smaller than T1 and T2 relaxation times) in the True-FISP sequence allows to obtain an acquisition time of ~ 0.5 s per slice in real-time MR imaging [138, 139]. Therefore, True-FISP acquisition was our method of choice in the identification of magnetic particles in real-time. However, the sequence shall be modified to provide positive contrasts for the in-vivo applications.

8.4 Accuracy of the proposed technique

In a recent study [140], the total spectrum of the human hepatic vasculature, covering the macro- down to the microcirculation, was visualized and reconstructed in 3D through vascular corrosion casting and micro-CT scanning. Although, results were based on the scans of a single liver, the detailed 3D data gathered gives an insight into the liver morphology including the mean radius and length as well as the estimated number of vessels per generation.

At the macrocirculation level, mean radii vary from 13 mm to 1 mm. At the microcirculation level, mean radii and the mean length of the hepatic artery vary in the range of 80 to 800 μm and 0.7 to 54 mm, respectively. At the capillary level (mean radii smaller than 40μm), the vascular network becomes highly interconnected and intertwined and thus a 3D illustration will only be possible through microscopic techniques and over a very limited region.

In chapters 4 and 5, we showed the possibility of visualization of small microagglomerations reaching 50 μm in diameter with an accuracy of approximately half the size of a pixel (the positioning error decreases as the spatial resolution increases). Therefore, the identification of multiple agglomerations in a single voxel poses a particular challenge in the proposed technique. We calculated the artifacts' center of mass to determine the position of the particles. This technique yields an estimate of the particle's position with sub-pixel accuracy. On the other hand, new advanced mathematical models have been used to develop techniques for improving the precision in particle positioning and measuring the displacement of a moving mass [141-144]. Application of such techniques in enhancing the positioning accuracy is subject to further studies.

In chapter 6, we showed the feasibility of 3D reconstruction of a vascular network through our proposed technique. The positioning error was found to be significantly larger on the axis that is perpendicular to the imaging plane. This difference arises from the imaging limitation in setting the slice thickness. Decreasing the slice thickness results in a significant drop in the signal to noise ratio. In order to compensate for a relatively high positioning error on the third dimension, we proposed to combine the reconstructed points generated by the scans of at least two different spatial planes. If the images of a 3D vascular network are acquired using a particular imaging plane, information relating to the parts of the network located between the two adjacent slices will be missed. The missing data can be compensated by adding the coordinates obtained from the images of other spatial planes.

In our proposed technique, delineation of the vessels necessitates; 1) a sensitive imaging sequence to detect small quantities of nanoparticles and 2) an adequate number of agglomerations to be injected in the vascular network so that the initial dispersed reconstructed points turn to a pattern illustrating the vascular network. Number of the agglomerations to be injected may be obtained in advance through a simulation study. Information of the local vasculature where the imaging is performed will be the necessary inputs for the simulation study. This includes the mean radius, the mean length, the estimated number of vessels per generation as well as the imaging parameters.

CHAPTER 9 CONCLUSION AND RECOMMENDATIONS

This project aimed to develop a new technique for visualization of human microvasculatures not visible using the current clinical imaging modalities and is a complementary step in the MRN-assisted chemoembolization intervention [12, 13]. Our objective was to find a 3D representation of the local vascular network leading to a tumor site, which can subsequently be used for the navigation of therapeutic magnetic carriers. Our visualization technique was developed based on the magnetic particles' effect on the homogeneous magnetic field of a clinical MRI system.

Initially, behavior of the magnetic particles of different sizes and magnetic domains in the presence of MRI's magnetic field was studied through simulation and phantom experiments. Subsequently, capacity of the clinical scanners in detecting magnetic particles was evaluated. These gave an insight into the potentials and the limitations of the proposed technique (Appendices A and B and chapter 4). They helped achieve the first two objectives of the project, defined in chapter 3.

Thereafter, an algorithm was proposed for 3D reconstruction of an unknown vascular network. The algorithm was based on susceptibility effect of the magnetic nanoparticles and their real-time MR tracking. The proposed algorithm was assessed through 2D visualization of a micrometric vascular network using magnetic agglomerations. The results suggested that the technique could be used to reconstruct a micrometric vascular tree beyond the spatial resolution of the system, with a measured average error of approximately half of a pixel's size (chapter 5). The experiment was carried out using a 1.5T MR scanner, a standard head coil and typical imaging parameters over a 16×16 cm^2 FOV.

Conclusively, the proposed technique was studied in a 3D model (chapter 6). The technique was tested in a phantom model. It was confirmed that the method could be used for reconstruction of a vascular network using a clinical scanner at the subpixel accuracy. A new technique in the generation of stable micron-sized agglomerations of nanoparticles using a microfluidic device was developed and presented in chapter 7.

In-vivo realization of the proposed technique necessitates further steps:

- The sequence of choice (True-FISP) should be modified to yield positive contrast imaging of the iron oxide nanoparticles [132],
- A simulation method should be developed to determine the number of the microagglomerations necessary to visualize a vascular network and also the amount of the required magnetic nanoparticles,
- The localization technique may be improved by applying a new mathematical model for positioning of moving masses through real-time images [141, 143],
- Soft tissue and motion artifacts should be assessed and compensated,
- Novel image reconstruction techniques, such as compressed sensing, may be applied to reduce the acquisition time per slice [139, 145, 146].

The clinical application of the proposed technique will result in:

- Decreasing the amount of antitumor drug,
- Reducing the side effects of chemo-therapy,
- Reducing the risk of tumor reformation, and
- Reducing the risk of tumor metastases to other organs of the body.

The results outlined can improve treatment of cancer significantly and reduce the costs incurred to the patients. It will have an impact on life expectancy of the patients fighting with cancer and as well, improve their quality of life during the treatment.

REFERENCES

[1] S. A. Hussain, D. R. Ferry, G. El-Gazzaz, D. F. Mirza, N. D. James, P. McMaster*, et al.*, "Hepatocellular carcinoma," *Ann Oncol,* vol. 12, pp. 161-72, Feb 2001.

[2] M. J. O'Connell, J. A. Martenson, H. S. Wieand, J. E. Krook, J. S. Macdonald, D. G. Haller*, et al.*, "Improving adjuvant therapy for rectal cancer by combining protracted-infusion fluorouracil with radiation therapy after curative surgery," *N Engl J Med,* vol. 331, pp. 502-7, Aug 25 1994.

[3] J. C. Barreto-Andrade, E. V. Efimova, H. J. Mauceri, M. A. Beckett, H. G. Sutton, T. E. Darga*, et al.*, "Response of Human Prostate Cancer Cells and Tumors to Combining PARP Inhibition with Ionizing Radiation," *Molecular Cancer Therapeutics,* vol. 10, pp. 1185-1193, Jul 2011.

[4] P. Warde, M. Mason, K. Ding, P. Kirkbride, M. Brundage, R. Cowan*, et al.*, "Combined androgen deprivation therapy and radiation therapy for locally advanced prostate cancer: a randomised, phase 3 trial," *Lancet,* vol. 378, pp. 2104-2111, Dec 17 2011.

[5] G. N. Hortobagyi, F. C. Ames, A. U. Buzdar, S. W. Kau, M. D. McNeese, D. Paulus*, et al.*, "Management of stage III primary breast cancer with primary chemotherapy, surgery, and radiation therapy," *Cancer,* vol. 62, pp. 2507-16, Dec 15 1988.

[6] H. W. Herr, S. M. Donat, and D. F. Bajorin, "Post-chemotherapy surgery in patients with unresectable or regionally metastatic bladder cancer," *J Urol,* vol. 165, pp. 811-4, Mar 2001.

[7] E. Liapi, C. C. Georgiades, K. Hong, and J. F. Geschwind, "Transcatheter arterial chemoembolization: current technique and future promise," *Tech Vasc Interv Radiol,* vol. 10, pp. 2-11, Mar 2007.

[8] G. Maleux, H. van Malenstein, V. Vandecaveye, S. Heye, J. Vaninbroukx, F. Nevens*, et al.*, "Transcatheter chemoembolization of unresectable hepatocellular carcinoma: current knowledge and future directions," *Dig Dis,* vol. 27, pp. 157-63, 2009.

[9] L. Brannon-Peppas and J. O. Blanchette, "Nanoparticle and targeted systems for cancer therapy," *Advanced Drug Delivery Reviews,* vol. 64, pp. 206-212, Dec 2012.

[10] D. M. Goldenberg, "Targeted therapy of cancer with radiolabeled antibodies," *Journal of Nuclear Medicine,* vol. 43, pp. 693-713, May 2002.

[11] J. F. Kukowska-Latallo, K. A. Candido, Z. Y. Cao, S. S. Nigavekar, I. J. Majoros, T. P. Thomas*, et al.*, "Nanoparticle targeting of anticancer drug improves therapeutic response in animal model of human epithelial cancer," *Cancer Research,* vol. 65, pp. 5317-5324, Jun 15 2005.

[12] P. Pouponneau, J. C. Leroux, G. Soulez, L. Gaboury, and S. Martel, "Co-encapsulation of magnetic nanoparticles and doxorubicin into biodegradable microcarriers for deep tissue targeting by vascular MRI navigation," *Biomaterials,* vol. 32, pp. 3481-3486, May 2011.

[13] P. Pouponneau, J. C. Leroux, and S. Martel, "Magnetic nanoparticles encapsulated into biodegradable microparticles steered with an upgraded magnetic resonance imaging system for tumor chemoembolization," *Biomaterials,* vol. 30, pp. 6327-6332, Nov 2009.

[14] J. B. Mathieu, G. Beaudoin, and S. Martel, "Method of propulsion of a ferromagnetic core in the cardiovascular system through magnetic gradients generated by an MRI system," *IEEE Trans Biomed Eng,* vol. 53, pp. 292-9, Feb 2006.

[15] J. B. Mathieu, S. Martel, L. Yahia, G. Soulez, and G. Beaudoin, "Preliminary investigation of the feasibility of magnetic propulsion for future microdevices in blood vessels," *Biomed Mater Eng,* vol. 15, pp. 367-74, 2005.

[16] S. Martel, J. B. Mathieu, O. Felfoul, A. Chanu, E. Aboussouan, S. Tamaz*, et al.*, "Automatic navigation of an untethered device in the artery of a living animal using a conventional clinical magnetic resonance imaging system," *Applied Physics Letters,* vol. 90, Mar 12 2007.

[17] S. Tamaz, R. Gourdeau, A. Chanu, J. B. Mathieu, and S. Martel, "Real-time MRI-based control of a ferromagnetic core for endovascular navigation," *Ieee Transactions on Biomedical Engineering,* vol. 55, pp. 1854-1863, Jul 2008.

[18] O. Felfoul, E. Aboussouan, A. Chanu, and S. Martel, "Real-time Positioning and Tracking Technique for Endovascular Untethered Microrobots Propelled by MRI Gradients," *Icra: 2009 Ieee International Conference on Robotics and Automation, Vols 1-7,* pp. 2447-2452, 2009.

[19] O. Felfoul, J. B. Mathieu, G. Beaudoin, and S. Martel, "In vivo MR-tracking based on magnetic signature selective excitation," *Ieee Transactions on Medical Imaging,* vol. 27, pp. 28-35, Jan 2008.

[20] P. Pouponneau, G. Soulez, G. Beaudoin, J. C. Leroux, and S. Martel, "MR Imaging of Therapeutic Magnetic Microcarriers Guided by Magnetic Resonance Navigation for Targeted Liver Chemoembolization," *Cardiovascular and Interventional Radiology,* vol. 37, pp. 784-790, Jun 2014.

[21] A. Bigot, C. Tremblay, G. Soulez, and S. Martel, "Magnetic Resonance Navigation of a Bead Inside a Three-Bifurcation PMMA Phantom Using an Imaging Gradient Coil Insert," *Ieee Transactions on Robotics,* vol. 30, pp. 719-727, Jun 2014.

[22] J. W. M. Bulte and D. L. Kraitchman, "Iron oxide MR contrast agents for molecular and cellular imaging," *Nmr in Biomedicine,* vol. 17, pp. 484-499, Nov 2004.

[23] B. Chertok, B. A. Moffat, A. E. David, F. Q. Yu, C. Bergemann, B. D. Ross*, et al.*, "Iron oxide nanoparticles as a drug delivery vehicle for MRI monitored magnetic targeting of brain tumors," *Biomaterials,* vol. 29, pp. 487-496, Feb 2008.

[24] M. K. Yu, Y. Y. Jeong, J. Park, S. Park, J. W. Kim, J. J. Min*, et al.*, "Drug-loaded superparamagnetic iron oxide nanoparticles for combined cancer imaging and therapy in vivo," *Angewandte Chemie-International Edition,* vol. 47, pp. 5362-5365, 2008.

[25] S. Laurent, S. Dutz, U. O. Hafeli, and M. Mahmoudi, "Magnetic fluid hyperthermia: Focus on superparamagnetic iron oxide nanoparticles," *Advances in Colloid and Interface Science,* vol. 166, pp. 8-23, Aug 10 2011.

[26] Z. Liu, T. Lammers, J. Ehling, S. Fokong, J. Bornemann, F. Kiessling*, et al.*, "Iron oxide nanoparticle-containing microbubble composites as contrast agents for MR and ultrasound dual-modality imaging," *Biomaterials,* vol. 32, pp. 6155-6163, Sep 2011.

[27] R. A. Brooks, "T-2-shortening by strongly magnetized spheres: A chemical exchange model," *Magnetic Resonance in Medicine,* vol. 47, pp. 388-391, Feb 2002.

[28] S. Kinner, S. Maderwald, N. Parohl, J. Albert, C. Corot, P. Robert*, et al.*, "Contrast-Enhanced Magnetic Resonance Angiography in Rabbits Evaluation of the Gadolinium-Based Agent P846 and the Iron-Based Blood Pool Agent P904 in Comparison With Gadoterate Meglumine," *Investigative Radiology,* vol. 46, pp. 524-529, Aug 2011.

[29] M. A. Sieber, H. Pietsch, J. Walter, W. Haider, T. Frenzel, and H. J. Weinmann, "A preclinical study to investigate the development of nephrogenic systemic fibrosis: A possible role for gadolinium-based contrast media," *Investigative Radiology,* vol. 43, pp. 65-75, Jan 2008.

[30] M. A. Sieber, T. Steger-Hartmann, P. Lengsfeld, and H. Pietsch, "Gadolinium-Based Contrast Agents and NSF: Evidence from Animal Experience," *Journal of Magnetic Resonance Imaging,* vol. 30, pp. 1268-1276, Dec 2009.

[31] T. K. Jain, M. K. Reddy, M. A. Morales, D. L. Leslie-Pelecky, and V. Labhasetwar, "Biodistribution, clearance, and biocompatibility of iron oxide magnetic nanoparticles in rats," *Molecular Pharmaceutics,* vol. 5, pp. 316-327, Mar-Apr 2008.

[32] C. Luna, M. D. Morales, C. J. Serna, and M. Vazquez, "Multidomain to single-domain transition for uniform Co80Ni20 nanoparticles," *Nanotechnology,* vol. 14, pp. 268-272, Feb 2003.

[33] M. Mahmoudi, S. Sant, B. Wang, S. Laurent, and T. Sen, "Superparamagnetic iron oxide nanoparticles (SPIONs): Development, surface modification and applications in chemotherapy," *Advanced Drug Delivery Reviews,* vol. 63, pp. 24-46, Jan-Feb 2011.

[34] C. Tassa, S. Y. Shaw, and R. Weissleder, "Dextran-Coated Iron Oxide Nanoparticles: A Versatile Platform for Targeted Molecular Imaging, Molecular Diagnostics, and Therapy," *Accounts of Chemical Research,* vol. 44, pp. 842-852, Oct 2011.

[35] T. Allkemper, C. Bremer, L. Matuszewski, W. Ebert, and P. Reimer, "Contrast-enhanced blood-pool MR angiography with optimized iron oxides: Effect of size and dose on vascular contrast enhancement in rabbits," *Radiology,* vol. 223, pp. 432-438, May 2002.

[36] R. Weissleder, D. D. Stark, B. L. Engelstad, B. R. Bacon, C. C. Compton, D. L. White*, et al.*, "Superparamagnetic Iron-Oxide - Pharmacokinetics and Toxicity," *American Journal of Roentgenology,* vol. 152, pp. 167-173, Jan 1989.

[37] M. Sigovan, W. Gasper, H. F. Alley, C. D. Owens, and D. Saloner, "USPIO-enhanced MR Angiography of Arteriovenous Fistulas in Patients with Renal Failure," *Radiology,* vol. 265, pp. 584-590, Nov 2012.

[38] A. B. Nayak, A. Luhar, M. Hanudel, B. Gales, T. R. Hall, J. P. Finn*, et al.*, "High-resolution, whole-body vascular imaging with ferumoxytol as an alternative to gadolinium agents in a pediatric chronic kidney disease cohort," *Pediatr Nephrol,* Sep 12 2014.

[39] B. H. Kim, N. Lee, H. Kim, K. An, Y. I. Park, Y. Choi*, et al.*, "Large-scale synthesis of uniform and extremely small-sized iron oxide nanoparticles for high-resolution T1

magnetic resonance imaging contrast agents," *J Am Chem Soc,* vol. 133, pp. 12624-31, Aug 17 2011.

[40] Y. Y. I. Shih, E. R. Muir, G. Li, B. H. De La Garza, and T. Q. Duong, "High-Resolution 3D MR Microangiography of the Rat Ocular Circulation," *Radiology,* vol. 264, pp. 234-241, Jul 2012.

[41] C. Heyn, C. V. Bowen, B. K. Rutt, and P. J. Foster, "Detection threshold of single SPIO-Labeled cells with FIESTA," *Magnetic Resonance in Medicine,* vol. 53, pp. 312-320, Feb 2005.

[42] T. Lowery, "Nanomaterials - Based Magnetic Relaxation Switch Biosensors," *Magnetic Nanomaterials,* pp. 3-53, 2009.

[43] H. W. de Haan, "Mechanisms of Proton Spin Dephasing in a System of Magnetic Particles," *Magnetic Resonance in Medicine,* vol. 66, pp. 1748-1758, Dec 2011.

[44] S. Taktak, D. Sosnovik, M. J. Cima, R. Weissfeder, and L. Josephson, "Multiparameter magnetic relaxation switch assays," *Analytical Chemistry,* vol. 79, pp. 8863-8869, Dec 1 2007.

[45] C. V. Bowen, X. W. Zhang, G. Saab, P. J. Gareau, and B. K. Rutt, "Application of the static dephasing regime theory to superparamagnetic iron-oxide loaded cells," *Magnetic Resonance in Medicine,* vol. 48, pp. 52-61, Jul 2002.

[46] R. M. Weisskoff, C. S. Zuo, J. L. Boxerman, and B. R. Rosen, "Microscopic Susceptibility Variation and Transverse Relaxation - Theory and Experiment," *Magnetic Resonance in Medicine,* vol. 31, pp. 601-610, Jun 1994.

[47] V. Demas and T. J. Lowery, "Magnetic resonance for in vitro medical diagnostics: superparamagnetic nanoparticle-based magnetic relaxation switches," *New Journal of Physics,* vol. 13, Feb 4 2011.

[48] R. Hong, M. J. Cima, R. Weissleder, and L. Josephson, "Magnetic microparticle aggregation for viscosity determination by MR," *Magnetic Resonance in Medicine,* vol. 59, pp. 515-520, Mar 2008.

[49] J. R. Reichenbach, R. Venkatesan, D. A. Yablonskiy, M. R. Thompson, S. Lai, and E. M. Haacke, "Theory and application of static field inhomogeneity effects in gradient-echo imaging," *J Magn Reson Imaging,* vol. 7, pp. 266-79, Mar-Apr 1997.

[50] C. J. G. Bakker, R. Bhagwandien, M. A. Moerland, and L. M. P. Ramos, "Simulation of Susceptibility Artifacts in 2d and 3d Fourier-Transform Spin-Echo and Gradient-Echo Magnetic-Resonance-Imaging," *Magnetic Resonance Imaging,* vol. 12, pp. 767-774, 1994.

[51] C. J. G. Bakker, R. Bhagwandien, M. A. Moerland, and M. Fuderer, "Susceptibility Artifacts in 2dft Spin-Echo and Gradient-Echo Imaging - the Cylinder Model Revisited," *Magnetic Resonance Imaging,* vol. 11, pp. 539-548, 1993.

[52] J. F. Schenck, "The role of magnetic susceptibility in magnetic resonance imaging: MRI magnetic compatibility of the first and second kinds," *Medical Physics,* vol. 23, pp. 815-850, Jun 1996.

[53] D. A. Yablonskiy and E. M. Haacke, "Theory of Nmr Signal Behavior in Magnetically Inhomogeneous Tissues - the Static Dephasing Regime," *Magnetic Resonance in Medicine,* vol. 32, pp. 749-763, Dec 1994.

[54] O. Beuf, A. Briguet, M. Lissac, and R. Davis, "Magnetic resonance imaging for the determination of magnetic susceptibility of materials," *Journal of Magnetic Resonance Series B,* vol. 112, pp. 111-118, Aug 1996.

[55] C. Bos, M. A. Viergever, and C. J. G. Bakker, "On the artifact of a subvoxel susceptibility deviation in spoiled gradient-echo imaging," *Magnetic Resonance in Medicine,* vol. 50, pp. 400-404, Aug 2003.

[56] P. T. Callaghan, "Susceptibility-Limited Resolution in Nuclear-Magnetic-Resonance Microscopy," *Journal of Magnetic Resonance,* vol. 87, pp. 304-318, Apr 1990.

[57] A. Ericsson, A. Hemmingsson, B. Jung, and G. O. Sperber, "Calculation of MRI artifacts caused by static field disturbances " *Physics in Medicine and Biology*

, vol. 33, pp. 1103-1112, 1988.

[58] S. Posse and W. P. Aue, "Susceptibility Artifacts in Spin-Echo and Gradient-Echo Imaging," *Journal of Magnetic Resonance,* vol. 88, pp. 473-492, Jul 1990.

[59] T. Wortmann, C. Dahmen, and S. Fatikow, "Study of MRI Susceptibility Artifacts for Nanomedical Applications," *Journal of Nanotechnology in Engineering and Medicine,* vol. 1, 2010.

[60] G. Zabow, S. J. Dodd, E. Shapiro, J. Moreland, and A. P. Koretsky, "Microfabricated High-Moment Micrometer-Sized MRI Contrast Agents," *Magnetic Resonance in Medicine,* vol. 65, pp. 645-655, Mar 2011.

[61] K. P. Pruessmann, M. Weiger, M. B. Scheidegger, and P. Boesiger, "SENSE: Sensitivity encoding for fast MRI," *Magnetic Resonance in Medicine,* vol. 42, pp. 952-962, Nov 1999.

[62] D. K. Sodickson and W. J. Manning, "Simultaneous acquisition of spatial harmonics (SMASH): Fast imaging with radiofrequency coil arrays," *Magnetic Resonance in Medicine,* vol. 38, pp. 591-603, Oct 1997.

[63] M. H. Buonocore and L. S. Gao, "Ghost artifact reduction for echo planar imaging using image phase correction," *Magnetic Resonance in Medicine,* vol. 38, pp. 89-100, Jul 1997.

[64] E. M. Haacke, R. W. Brown, M. R. Thompson, and R. Venkatesan, "Magnetic Resonance Imaging: Physical Principles and Sequence Design," 1999.

[65] M. A. Bernstein, K. F. King, and X. J. Zhou, "Handbook of MRI Pulse Sequences," 2004.

[66] T. Y. Huang, I. J. Huang, C. Y. Chen, K. Scheffler, H. W. Chung, and H. C. Cheng, "Are TrueFISP images T2/T1-weighted?," *Magn Reson Med,* vol. 48, pp. 684-8, Oct 2002.

[67] K. Scheffler and J. Hennig, "Is TrueFISP a gradient-echo or a spin-echo sequence?," *Magnetic Resonance in Medicine,* vol. 49, pp. 395-397, Feb 2003.

[68] A. Bozzao, R. Floris, M. Pocek, F. Fasoli, F. G. Garaci, and G. Simonetti, "[Non-invasive assessment of epiaortic vessels. Comparison of magnetic resonance angiography with

gadolinium, spiral computerized tomography angiography, and digital angiography]," *Radiol Med,* vol. 101, pp. 48-53, Jan-Feb 2001.

[69] A. Hochmuth, U. Spetzger, and M. Schumacher, "Comparison of three-dimensional rotational angiography with digital subtraction angiography in the assessment of ruptured cerebral aneurysms," *American Journal of Neuroradiology,* vol. 23, pp. 1199-1205, Aug 2002.

[70] P. J. Nederkoorn, Y. van der Graaf, and M. Hunink, "Duplex ultrasound and magnetic resonance angiography compared with digital subtraction angiography in carotid artery stenosis - A systematic review," *Stroke,* vol. 34, pp. 1324-1331, May 2003.

[71] S. G. Wetzel, E. Kirsch, K. W. Stock, M. Kolbe, A. Kaim, and E. W. Radue, "Cerebral veins: comparative study of CT venography with intraarterial digital subtraction angiography," *AJNR Am J Neuroradiol,* vol. 20, pp. 249-55, Feb 1999.

[72] H. K. Pannu, R. E. Thompson, J. Phelps, C. A. Magee, and E. K. Fishman, "Optimal contrast agents for vascular imaging on computed tomography: Iodixanol versus iohexol," *Academic Radiology,* vol. 12, pp. 576-584, May 2005.

[73] M. Anzidei, A. Napoli, F. Zaccagna, P. Di Paolo, L. Saba, B. C. Marincola*, et al.*, "Diagnostic accuracy of colour Doppler ultrasonography, CT angiography and blood-pool-enhanced MR angiography in assessing carotid stenosis: a comparative study with DSA in 170 patients," *Radiologia Medica,* vol. 117, pp. 54-71, Feb 2012.

[74] M. Killer, M. R. McCoy, M. C. Vestal, L. Weitgasser, and G. M. Cruise, "Use of CT Angiography in Comparison with Other Imaging Techniques for the Determination of Embolus and Remnant Size in Experimental Aneurysms Embolized with Hydrogel Filaments," *American Journal of Neuroradiology,* vol. 32, pp. 923-928, May 2011.

[75] R. C. Gessner, C. B. Frederick, F. S. Foster, and P. A. Dayton, "Acoustic angiography: a new imaging modality for assessing microvasculature architecture," *Int J Biomed Imaging,* vol. 2013, p. 936593, 2013.

[76] Y. Yuan, "Optical-resolution photoacoustic microscopy for imaging blood vessels in vivo," *Optics in Health Care and Biomedical Optics V,* vol. 8553, 2012.

[77] A. P. Tregaskiss, A. N. Goodwin, L. D. Bright, C. H. Ziegler, and R. D. Acland, "Three-dimensional CT angiography: A new technique for imaging microvascular anatomy," *Clinical Anatomy,* vol. 20, pp. 116-123, Mar 2007.

[78] A. Berrington de Gonzalez and S. Darby, "Risk of cancer from diagnostic X-rays: estimates for the UK and 14 other countries," *Lancet,* vol. 363, pp. 345-351, Jan 31 2004.

[79] B. J. Wintersperger, S. B. Reeder, K. Nikolaou, O. Dietrich, A. Huber, A. Greiser*, et al.*, "Cardiac CINE MR Imaging with a 32-channel cardiac coil and parallel imaging: Impact of acceleration factors on image quality and volumetric accuracy," *Journal of Magnetic Resonance Imaging,* vol. 23, pp. 222-227, Feb 2006.

[80] R. J. Nijenhuis, T. Leiner, E. M. J. Cornips, J. T. Wilmink, M. J. Jacobs, J. M. A. van Engelshoven*, et al.*, "Spinal cord feeding arteries at MR angiography for thoracoscopic spinal surgery: Feasibility study and implications for surgical approach," *Radiology,* vol. 233, pp. 541-547, Nov 2004.

[81] A. C. Stamm, C. L. Wright, M. V. Knopp, P. Schmalbrock, and J. T. Heverhagen, "Phase contrast and time-of-flight magnetic resonance angiography of the intracerebral arteries at 1.5, 3 and 7 T," *Magnetic Resonance Imaging,* vol. 31, pp. 545-549, May 2013.

[82] M. A. O'Reilly and K. Hynynen, "A super-resolution ultrasound method for brain vascular mapping," *Medical Physics,* vol. 40, Nov 2013.

[83] H. Ragde, G. M. Kenny, G. P. Murphy, and K. Landin, "Transrectal ultrasound microbubble contrast angiography of the prostate," *Prostate,* vol. 32, pp. 279-283, Sep 1 1997.

[84] S. Makita, Y. Hong, M. Yamanari, T. Yatagai, and Y. Yasuno, "Optical coherence angiography," *Optics Express,* vol. 14, pp. 7821-7840, Aug 21 2006.

[85] S. Makita, F. Jaillon, M. Yamanari, M. Miura, and Y. Yasuno, "Comprehensive in vivo micro-vascular imaging of the human eye by dual-beam-scan Doppler optical coherence angiography," *Optics Express,* vol. 19, pp. 1271-1283, Jan 17 2011.

[86] Y. Jia, S. T. Bailey, D. J. Wilson, O. Tan, M. L. Klein, C. J. Flaxel*, et al.*, "Quantitative optical coherence tomography angiography of choroidal neovascularization in age-related macular degeneration," *Ophthalmology,* vol. 121, pp. 1435-44, Jul 2014.

[87] M. A. Konerding, A. J. Miodonski, and A. Lametschwandtner, "Microvascular corrosion casting in the study of tumor vascularity: A review," *Scanning Microscopy,* vol. 9, pp. 1233-1244, 1995.

[88] B. J. Vakoc, R. M. Lanning, J. A. Tyrrell, T. P. Padera, L. A. Bartlett, T. Stylianopoulos*, et al.*, "Three-dimensional microscopy of the tumor microenvironment in vivo using optical frequency domain imaging," *Nat Med,* vol. 15, pp. 1219-23, Oct 2009.

[89] B. J. Vakoc, R. M. Lanning, J. A. Tyrrell, T. P. Padera, L. A. Bartlett, T. Stylianopoulos*, et al.*, "Three-dimensional microscopy of the tumor microenvironment in vivo using optical frequency domain imaging," *Nature Medicine,* vol. 15, pp. 1219-U151, Oct 2009.

[90] C. K. Kang, C. A. Park, Y. B. Lee, C. W. Park, S. M. Hong, Y. B. Kim*, et al.*, "Micro-Vascular Imaging Experiences of Time-of-Flight MRA at 7T for Cerebrovascular Diseases," *International Journal of Imaging Systems and Technology,* vol. 24, pp. 121-128, Jun 2014.

[91] P. J. Bolan, E. Yacoub, M. Garwood, K. Ugurbil, and N. Harel, "In vivo micro-MRI of intracortical neurovasculature," *Neuroimage,* vol. 32, pp. 62-69, Aug 1 2006.

[92] R. Savai, A. C. Langheinrich, R. T. Schermuly, S. S. Pullamsetti, R. Dumitrascu, H. Traupe*, et al.*, "Evaluation of Angiogenesis Using Micro-Computed Tomography in a Xenograft Mouse Model of Lung Cancer," *Neoplasia,* vol. 11, pp. 48-56, Jan 2009.

[93] C. A. Berrios-Otero, Y. Z. Wadghiri, B. J. Nieman, A. L. Joyner, and D. H. Turnbull, "Three-Dimensional Micro-MRI Analysis of Cerebral Artery Development in Mouse Embryos," *Magnetic Resonance in Medicine,* vol. 62, pp. 1431-1439, Dec 2009.

[94] N. Petridou, M. Italiaander, B. L. van de Bank, J. C. Siero, P. R. Luijten, and D. W. Klomp, "Pushing the limits of high-resolution functional MRI using a simple high-density multi-element coil design," *NMR Biomed,* vol. 26, pp. 65-73, Jan 2013.

[95] J. H. Jensen, H. Z. Lu, and M. Inglese, "Microvessel density estimation in the human brain by means of dynamic contrast-enhanced echo-planar imaging," *Magnetic Resonance in Medicine,* vol. 56, pp. 1145-1150, Nov 2006.

[96] E. Laistler, R. Loewe, and E. Moser, "Magnetic resonance microimaging of human skin vasculature in vivo at 3 Tesla," *Magn Reson Med,* vol. 65, pp. 1718-23, Jun 2011.

[97] E. Laistler, Poirier-Quinot M, Ginefri JC, Lambert S, Dubuisson RM, and M. E. Boriasse E, Darrasse L, "Sub-nanoliter microscopic MR imaging of the human skin in vivo using a 12 mm superconducting surface coil at 1.5 Tesla. P," *ISMRM, Honolulu, USA,* p. 4758, 2009.

[98] J. H. Lee, "High-Contrast In Vivo Visualization of Microvessels Using Novel FeCo/GC Magnetic Nanocrystals (vol 62, pg 1497, 2009)," *Magnetic Resonance in Medicine,* vol. 63, pp. 1723-1723, Jun 2010.

[99] B. Blasiak, S. Barnes, T. Foniok, D. Rushforth, J. Matyas, D. Ponjevic*, et al.*, "Comparison of T2 and T2*-weighted MR molecular imaging of a mouse model of glioma," *BMC Med Imaging,* vol. 13, p. 20, Jul 18 2013.

[100] P. Smirnov, E. Lavergne, F. Gazeau, M. Lewin, A. Boissonnas, B. T. Doan*, et al.*, "In vivo cellular imaging of lymphocyte trafficking by MRI: a tumor model approach to cell-based anticancer therapy," *Magn Reson Med,* vol. 56, pp. 498-508, Sep 2006.

[101] P. Smirnov, M. Poirier-Quinot, C. Wilhelm, E. Lavergne, J. C. Ginefri, B. Combadiere*, et al.*, "In vivo single cell detection of tumor-infiltrating lymphocytes with a clinical 1.5 Tesla MRI system," *Magn Reson Med,* vol. 60, pp. 1292-7, Dec 2008.

[102] R. M. Lebel, R. S. Menon, and C. V. Bowen, "Relaxometry model of strong dipolar perturbers for balanced-SSFP: application to quantification of SPIO loaded cells," *Magn Reson Med,* vol. 55, pp. 583-91, Mar 2006.

[103] A. R. Mohammadi-Nejad, G. A. Hossein-Zadeh, and H. Soltanian-Zadeh, "Quantitative evaluation of optimal imaging parameters for single-cell detection in MRI using simulation," *Magn Reson Imaging,* vol. 28, pp. 408-17, Apr 2010.

[104] R. L. Lindquist, S. Papazoglou, C. Scharlach, H. Waiczies, J. Schnorr, M. Taupitz*, et al.*, "Imaging of magnetic microfield distortions allows sensitive single-cell detection," *Mol Imaging,* vol. 12, pp. 83-9, Mar-Apr 2013.

[105] T. Y. Siow, C. C. Chen, C. Y. Lin, J. Y. Chen, and C. Chang, "MR phase imaging: sensitive and contrast-enhancing visualization in cellular imaging," *Magn Reson Imaging,* vol. 30, pp. 247-53, Feb 2012.

[106] R. Di Corato, F. Gazeau, C. Le Visage, D. Fayol, P. Levitz, F. Lux*, et al.*, "High-resolution cellular MRI: gadolinium and iron oxide nanoparticles for in-depth dual-cell imaging of engineered tissue constructs," *ACS Nano,* vol. 7, pp. 7500-12, Sep 24 2013.

[107] G. Lamanna, A. Garofalo, G. Popa, C. Wilhelm, S. Begin-Colin, D. Felder-Flesch*, et al.*, "Endowing carbon nanotubes with superparamagnetic properties: applications for cell labeling, MRI cell tracking and magnetic manipulations," *Nanoscale,* vol. 5, pp. 4412-21, May 21 2013.

[108] E. M. Shapiro, S. Skrtic, K. Sharer, J. M. Hill, C. E. Dunbar, and A. P. Koretsky, "MRI detection of single particles for cellular imaging," *Proc Natl Acad Sci U S A,* vol. 101, pp. 10901-6, Jul 27 2004.

[109] P. Smirnov, F. Gazeau, J. C. Beloeil, B. T. Doan, C. Wilhelm, and B. Gillet, "Single-cell detection by gradient echo 9.4 T MRI: a parametric study," *Contrast Media Mol Imaging,* vol. 1, pp. 165-74, Jul-Aug 2006.

[110] M. Wolters, M. Oostendorp, B. F. Coolen, M. J. Post, J. M. Janssen, G. J. Strijkers*, et al.*, "Efficacy of positive contrast imaging techniques for molecular MRI of tumor angiogenesis," *Contrast Media Mol Imaging,* vol. 7, pp. 130-9, Mar-Apr 2012.

[111] C. Heyn, J. A. Ronald, L. T. Mackenzie, I. C. MacDonald, A. F. Chambers, B. K. Rutt*, et al.*, "In vivo magnetic resonance imaging of single cells in mouse brain with optical validation," *Magn Reson Med,* vol. 55, pp. 23-9, Jan 2006.

[112] K. A. Hinds, J. M. Hill, E. M. Shapiro, M. O. Laukkanen, A. C. Silva, C. A. Combs*, et al.*, "Highly efficient endosomal labeling of progenitor and stem cells with large magnetic particles allows magnetic resonance imaging of single cells," *Blood,* vol. 102, pp. 867-72, Aug 1 2003.

[113] E. M. Shapiro, K. Sharer, S. Skrtic, and A. P. Koretsky, "In vivo detection of single cells by MRI," *Magn Reson Med,* vol. 55, pp. 242-9, Feb 2006.

[114] L. Ciobanu and C. H. Pennington, "3D micron-scale MRI of single biological cells," *Solid State Nuclear Magnetic Resonance,* vol. 25, pp. 138-141, Jan 2004.

[115] P. Foster-Gareau, C. Heyn, A. Alejski, and B. K. Rutt, "Imaging single mammalian cells with a 1.5 T clinical MRI scanner," *Magnetic Resonance in Medicine,* vol. 49, pp. 968-971, May 2003.

[116] N. Olamaei, F. Cheriet, and S. Martel, "Magnetic resonance imaging of microvessels using iron-oxide nanoparticles," *Journal of Applied Physics,* vol. 113, p. 124701, Mar 28 2013.

[117] G. F. Christopher and S. L. Anna, "Microfluidic methods for generating continuous droplet streams," *Journal of Physics D-Applied Physics,* vol. 40, pp. R319-R336, Oct 7 2007.

[118] R. Dreyfus, P. Tabeling, and H. Willaime, "Ordered and disordered patterns in two-phase flows in microchannels," *Physical Review Letters,* vol. 90, Apr 11 2003.

[119] R. Seemann, M. Brinkmann, T. Pfohl, and S. Herminghaus, "Droplet based microfluidics," *Reports on Progress in Physics,* vol. 75, Jan 2012.

[120] J. H. Xu, S. W. Li, J. Tan, Y. J. Wang, and G. S. Luo, "Preparation of highly monodisperse droplet in a T-junction microfluidic device," *Aiche Journal,* vol. 52, pp. 3005-3010, Sep 2006.

[121] C. X. Zhao and A. P. J. Middelberg, "Two-phase microfluidic flows," *Chemical Engineering Science,* vol. 66, pp. 1394-1411, Apr 1 2011.

[122] A. G. G. Toh, Z. F. Wang, and S. H. Ng, "Fabrication of Embedded Microvalve on PMMA Microfluidic Devices through Surface Functionalization," *Dtip 2008: Symposium on Design, Test, Integration and Packaging of Mems/Moems,* pp. 267-272, 2008.

[123] H. Demachi, O. Matsui, H. Abo, and H. Tatsu, "Simulation model based on non-Newtonian fluid mechanics applied to the evaluation of the embolic effect of emulsions of iodized oil and anticancer drug," *Cardiovascular and Interventional Radiology,* vol. 23, pp. 285-290, Jul-Aug 2000.

[124] C. X. Wang, Y. Liu, H. L. Xu, Y. Ren, and Y. P. Qiu, "Influence of atmospheric pressure plasma treatment time on penetration depth of surface modification into fabric," *Applied Surface Science,* vol. 254, pp. 2499-2505, Feb 15 2008.

[125] A. Larsson and H. Derand, "Stability of polycarbonate and polystyrene surfaces after hydrophilization with high intensity oxygen RF plasma," *Journal of Colloid and Interface Science,* vol. 246, pp. 214-221, Feb 1 2002.

[126] J. M. Yeh, C. J. Weng, W. J. Liao, and Y. W. Mau, "Anticorrosively enhanced PMMA-SiO2 hybrid coatings prepared from the sol-gel approach with MSMA as the coupling agent," *Surface & Coatings Technology,* vol. 201, pp. 1788-1795, Oct 5 2006.

[127] L. Yobas, S. Martens, W. L. Ong, and N. Ranganathan, "High-performance flow-focusing geometry for spontaneous generation of monodispersed droplets," *Lab on a Chip,* vol. 6, pp. 1073-1079, 2006.

[128] S. Ichihashi, N. Marugami, T. Tanaka, S. Iwakoshi, N. Kurumatani, S. Kitano*, et al.*, "Preliminary experience with superparamagnetic iron oxide-enhanced dynamic magnetic resonance imaging and comparison with contrast-enhanced computed tomography in endoleak detection after endovascular aneurysm repair," *Journal of Vascular Surgery,* vol. 58, pp. 66-72, Jul 2013.

[129] F. D. Knollmann, J. C. Bock, K. Rautenberg, J. Beier, W. Ebert, and R. Felix, "Differences in predominant enhancement mechanisms of superparamagnetic iron oxide and ultrasmall superparamagnetic iron oxide for contrast-enhanced portal magnetic resonance angiography. Preliminary results of an animal study original investigation," *Invest Radiol,* vol. 33, pp. 637-43, Sep 1998.

[130] C. H. Cunningham, T. Arai, P. C. Yang, M. V. McConnell, J. M. Pauly, and S. M. Conolly, "Positive contrast magnetic resonance imaging of cells labeled with magnetic nanoparticles," *Magn Reson Med,* vol. 53, pp. 999-1005, May 2005.

[131] J. H. Seppenwoolde, M. A. Viergever, and C. J. Bakker, "Passive tracking exploiting local signal conservation: the white marker phenomenon," *Magn Reson Med,* vol. 50, pp. 784-90, Oct 2003.

[132] S. Patil, D. Jirak, F. Saudek, M. Hajek, and K. Scheffler, "Positive contrast visualization of SPIO-labeled pancreatic islets using echo-dephased steady-state free precession," *Eur Radiol,* vol. 21, pp. 214-20, Jan 2011.

[133] C. Diwoky, D. Liebmann, B. Neumayer, A. Reinisch, F. Knoll, D. Strunk*, et al.*, "Positive contrast of SPIO-labeled cells by off-resonant reconstruction of 3D radial half-echo bSSFP," *NMR Biomed,* Nov 7 2014.

[134] A. Moore, E. Marecos, A. Bogdanov, and R. Weissleder, "Tumoral distribution of long-circulating dextran-coated iron oxide nanoparticles in a rodent model," *Radiology,* vol. 214, pp. 568-574, Feb 2000.

[135] V. Dousset, C. Delalande, L. Ballarino, B. Quesson, D. Seilhan, M. Coussemacq, *et al.*, "In vivo macrophage activity imaging in the central nervous system detected by magnetic resonance," *Magnetic Resonance in Medicine,* vol. 41, pp. 329-333, Feb 1999.

[136] S. A. Schmitz, S. E. Coupland, R. Gust, S. Winterhalter, S. Wagner, M. Kresse, *et al.*, "Superparamagnetic iron oxide-enhanced MRI of atherosclerotic plaques in Watanabe hereditable hyperlipidemic rabbits," *Investigative Radiology,* vol. 35, pp. 460-471, Aug 2000.

[137] E. M. Shapiro, S. Skrtic, K. Sharer, J. M. Hill, C. E. Dunbar, and A. P. Koretsky, "MRI detection of single particles for cellular imaging," *Proceedings of the National Academy of Sciences of the United States of America,* vol. 101, pp. 10901-10906, Jul 27 2004.

[138] A. Kluge, C. Muller, J. Hansel, T. Gerriets, and G. Bachmann, "Real-time MR with TrueFISP for the detection of acute pulmonary embolism: initial clinical experience," *European Radiology,* vol. 14, pp. 709-718, Apr 2004.

[139] K. H. Zhang, L. Zhang, and M. H. Yang, "Real-Time Compressive Tracking," *Computer Vision - Eccv 2012, Pt Iii,* vol. 7574, pp. 864-877, 2012.

[140] C. Debbaut, P. Segers, P. Cornillie, C. Casteleyn, M. Dierick, W. Laleman, *et al.*, "Analyzing the human liver vascular architecture by combining vascular corrosion casting and micro-CT scanning: a feasibility study," *Journal of Anatomy,* vol. 224, pp. 509-517, Apr 2014.

[141] M. Debella-Gilo and A. Kaab, "Sub-pixel precision image matching for measuring surface displacements on mass movements using normalized cross-correlation," *Remote Sensing of Environment,* vol. 115, pp. 130-142, Jan 17 2011.

[142] R. Parthasarathy, "Rapid, accurate particle tracking by calculation of radial symmetry centers," *Nature Methods,* vol. 9, pp. 724-U291, Jul 2012.

[143] R. Parthasarathy, "Rapid, Accurate Single Particle Tracking Based on Radial Symmetry Center Determination," *Biophysical Journal,* vol. 102, pp. 202a-202a, Jan 31 2012.

[144] Y. Feng, J. Goree, and B. Liu, "Accurate particle position measurement from images," *Review of Scientific Instruments,* vol. 78, May 2007.

[145] A. Majumdar, R. K. Ward, and T. Aboulnasr, "Compressed Sensing Based Real-Time Dynamic MRI Reconstruction," *Ieee Transactions on Medical Imaging,* vol. 31, pp. 2253-2266, Dec 2012.

[146] M. Uecker, S. Zhang, D. Voit, A. Karaus, K. D. Merboldt, and J. Frahm, "Real-time MRI at a resolution of 20 ms," *Nmr in Biomedicine,* vol. 23, pp. 986-994, Oct 2010.

[147] E. M. Haacke, *Magnetic resonance imaging : physical principles and sequence design*. New York: Wiley, 1999.

[148] G. Zabow, S. J. Dodd, E. Shapiro, J. Moreland, and A. P. Koretsky, "Microfabricated high-moment micrometer-sized MRI contrast agents," *Magn Reson Med,* Oct 6 2010.

[149] C. Bos, M. A. Viergever, and C. J. Bakker, "On the artifact of a subvoxel susceptibility deviation in spoiled gradient-echo imaging," *Magn Reson Med,* vol. 50, pp. 400-4, Aug 2003.

[150] H. M. Silvennoinen, *et al.,* "CT angiographic analysis of carotid artery stenosis: comparison of manual assessment, semiautomatic vessel analysis, and digital subtraction angiography," *AJNR Am J Neuroradiol*, vol. 28, pp. 97-103, Jan 2007.

[151] Y. Tang, *et al*., "In vivo assessment of RAS-dependent maintenance of tumor angiogenesis by real-time magnetic resonance imaging," *Cancer Research*, vol. 65, pp. 8324-8330, Sep 15 2005.

[152] A. R. Guimaraes, *et al.*, "MRI with Magnetic Nanoparticles Monitors Downstream Anti-Angiogenic Effects of mTOR Inhibition," *Mol Imaging Biol*, Jun 18 2010.

[153] J. R. McCarthy, *et al.*, "Targeted nanoagents for the detection of cancers," *Mol Oncol*, Sep 8 2010.

[154] J. R. McCarthy and R. Weissleder, "Multifunctional magnetic nanoparticles for targeted imaging and therapy," Adv Drug Deliv Rev, vol. 60, pp. 1241-51, Aug 17 2008. R. Klabunde, "*Cardiovascular physiology concepts*," 2005.

[155] J. S. Weinstein, *et al.*, "Superparamagnetic iron oxide nanoparticles: diagnostic magnetic resonance imaging and potential therapeutic applications in neurooncology and central nervous system inflammatory pathologies, a review," *Journal of Cerebral Blood Flow and Metabolism*, vol. 30, pp. 15-35, Jan 2010

[156] A. K. Gupta and M. Gupta, "Synthesis and surface engineering of iron oxide nanoparticles for biomedical applications," *Biomaterials*, vol. 26, pp. 3995-4021, Jun 2005.

[157] S. Arbab, *et al.*, "Characterization of biophysical and metabolic properties of cells labeled with superparamagnetic iron oxide nanoparticles and transfection agent for cellular MR imaging," *Radiology*, vol. 229, pp. 838-846, Dec 2003.

[158] T. de Baere, *et al.*, "Modification of arterial and portal hemodynamics after injection of iodized oils and different emulsions of iodized oils in the hepatic artery: An experimental study," *Journal of Vascular and Interventional Radiology*, vol. 9, pp. 305-310, Mar-Apr 1998.

[159] M. Stuber, *et al.*, "Positive contrast visualization of iron oxide-labeled stem cells using inversion-recovery with ON-Resonant water suppression (IRON)," *Magnetic Resonance in Medicine,* vol. 58, pp. 1072-1077, Nov 2007.

[160] M. Spahn, "X-ray detectors in medical imaging," *Nuclear Instruments & Methods in Physics Research Section a-Accelerators Spectrometers Detectors and Associated Equipment*, vol. 731, pp. 57-63, Dec 11 2013.

[161] R. Jansen, *et al.*, "Chondramides A-D, new cytostatic and antifungal cyclodepsipeptides from Chondromyces crocatus (Myxobacteria): Isolation and structure elucidation," *Liebigs Annalen*, pp. 285-290, Feb 1996.

[162] J. C. Ginefri, *et al.*, "Contrast-enhanced dynamic MRI protocol with improved spatial and time resolution for in vivo microimaging of the mouse with a 1.5-T body scanner and a

superconducting surface coil," *Magnetic Resonance Imaging*, vol. 23, pp. 239-243, Feb 2005.

[163] D. R. Emerson, *et al.*, "Biomimetic design of microfluidic manifolds based on a generalised Murray's law," Lab on a Chip, vol. 6, pp. 447-54, Mar 2006. M. Spahn, "X-ray detectors in medical imaging," *Nuclear Instruments & Methods in Physics Research Section a-Accelerators Spectrometers Detectors and Associated Equipmen*t, vol. 731, p. 57, Dec 11 2013.

[164] N. Olamaei, *et al.*, "Dynamic tracking of magnetic nanoparticles for mapping microvascular networks using a clinical 1.5 T magnetic resonance scanner," *Applied Physics Letters*, vol. 104, May 26 2014.

[165] W. Wu, *et al.*, "Magnetic Iron Oxide Nanoparticles: Synthesis and Surface Functionalization Strategies," *Nanoscale Research Letters*, vol. 3, pp. 397-415, Nov 2008.

[166] M. Y. Yousif, *et al.*, "A blood-mimicking fluid for particle image velocimetry with silicone vascular models," *Experiments in Fluids*, vol. 50, pp. 769-774, Mar 2011.

APPENDIX A – VISIBILITY OF MAGNETIC MICROPARICLES IN CLINICAL MR IMAGES

Ferromagnetic materials have a rather high susceptibility. Magnetic susceptibility is a dimensionless quantitative measure of the degree of a material's ability to induce a local magnetic field inhomogeneity within an applied homogeneous magnetic field. The induced magnetic field inhomogeneity from a small object can be approximated by the magnetic fields of a dipole:

$$\vec{B}(\vec{r}) = B_0\hat{z} + \frac{\mu_0}{4\pi}\left(3\frac{(\vec{m}.\vec{r})\hat{r}}{r^5} - \frac{\vec{m}}{r^3}\right) \qquad (1)$$

where $\mu_o=4\pi\times10^{-7}$ is the permeability of the free space, $\hat{r}$ is the *r*-directional unit vector, $\hat{z}$ is the unit vector in z-direction, B_0 is the external uniform magnetic field and $\vec{m}$ is the magnetic dipole moment calculated by:

$$\vec{m} = \frac{4}{3}\pi a^3\vec{M}_{sat} \qquad (2)$$

where $\vec{\mathrm{M}}_{\mathrm{sat}}$and *a* correspond to the saturation magnetization and the radius of the sphere, respectively. The local field inhomogeneity leads to: a) signal loss as the result of the intravoxel dephasing and b) position shift caused by the wrong frequency encoding according to Larmor frequency:

$$\omega(\vec{r}) = \gamma\vec{B}_z(\vec{r}) \qquad (3)$$

where γ is the gyromagnetic ratio (42.576 MHz T^{-1}) for protons. For the intravoxel dephasing, the average signal (*s*) over the slice selection can be written as Fourier transform of the spin density (ρ), given by:

$$s = \int\rho(x,y,z)e^{-i\varphi}dz \text{ with } \varphi = \gamma\vec{B}_z(\vec{r})TE \qquad (4)$$

where φ is the phase dispersion across the voxel and TE is the echo time. The intravoxel dephasing creates an intensity distortion in the MR image, in the form of a signal loss (S_{loss}). Due to the 180° refocusing pulse, the dephasing effect is compensated in the SE sequence while it is well presented in the GE sequence. On the other hand, the wrong frequency encoding is followed by a geometrical distortion the degree of which is determined by the local field inhomogeneity and the readout gradient strength. The position error due to geometrical distortion is calculated by:

$$x' = x + \frac{\Delta B_z(\vec{r})}{G_R} \qquad (5)$$

where x is the readout direction, x' is the position generated from the MRI data and G_R in the strength of the readout direction.

Simulations were performed to systematically investigate the pattern and the amount of the susceptibility artifact under varying values of the TE, the diameter of the microsphere and the field strength. The susceptibility artifact was simulated based on the intravoxel dephasing by the phase accumulation at the TE (see Eq. (4)) using MATLAB® programming language.

Phantom experiments were carried out using three isolated stainless steel spheres (Salem specialty Ball Co., Inc.) measured 40, 20 and 15 µm in diameter and a saturation magnetization of 207 emu g^{-1}. A single microsphere for each of the mentioned sizes was isolated under microscope and it was suspended in the middle of a solution made up of gelatin and Sodium Chloride to mimic the human body relaxation times. Imaging was performed using 1.5T (Magnetom Siemens) and 3T (Acheiva Philips) MRI systems.

Experimental observations of S_{loss} (summing the in plane signal loss over the region of interest) as a function of TE on the coronal plane using external field strengths of 3T (a) and 1.5 T (b) for -♦- 40 µm, -■- 20 µm and -▲-15 µm stain less steel microspheres:

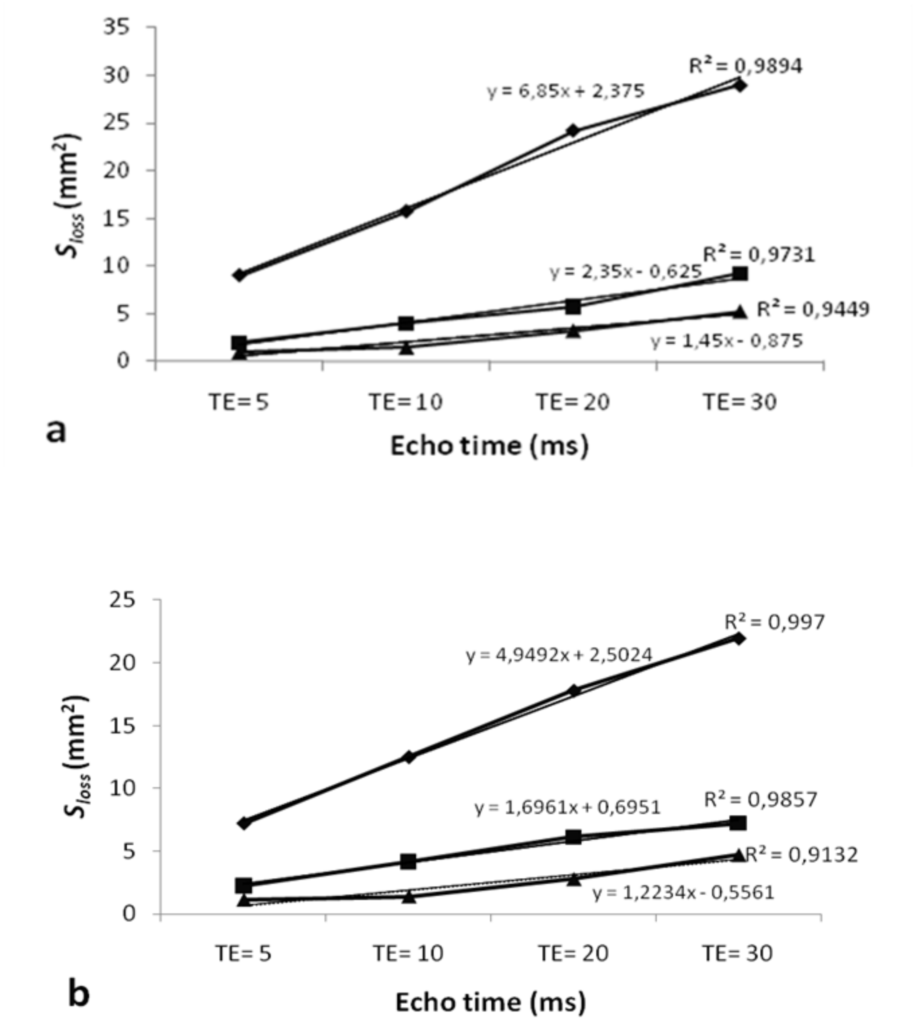

Experimental coronal images of the stain less steel microparticles sized 15 µm (left), 20 µm (middle) and 40 µm (right) in diameter, imaged by a 1.5 T and a 3 T scanners with a TE= 5 ms (a), TE= 20 ms (b) and TE = 30 ms (c). Right: Simulated coronal images of the stain less steel microparticles sized 15 µm (left), 20 µm (middle) and 40 µm (right) in diameter, with the following scan parameters: B0= 1.5 T and B0=3 T, TE= 5 ms (a), TE= 20 ms (b) and TE = 30 ms (c):

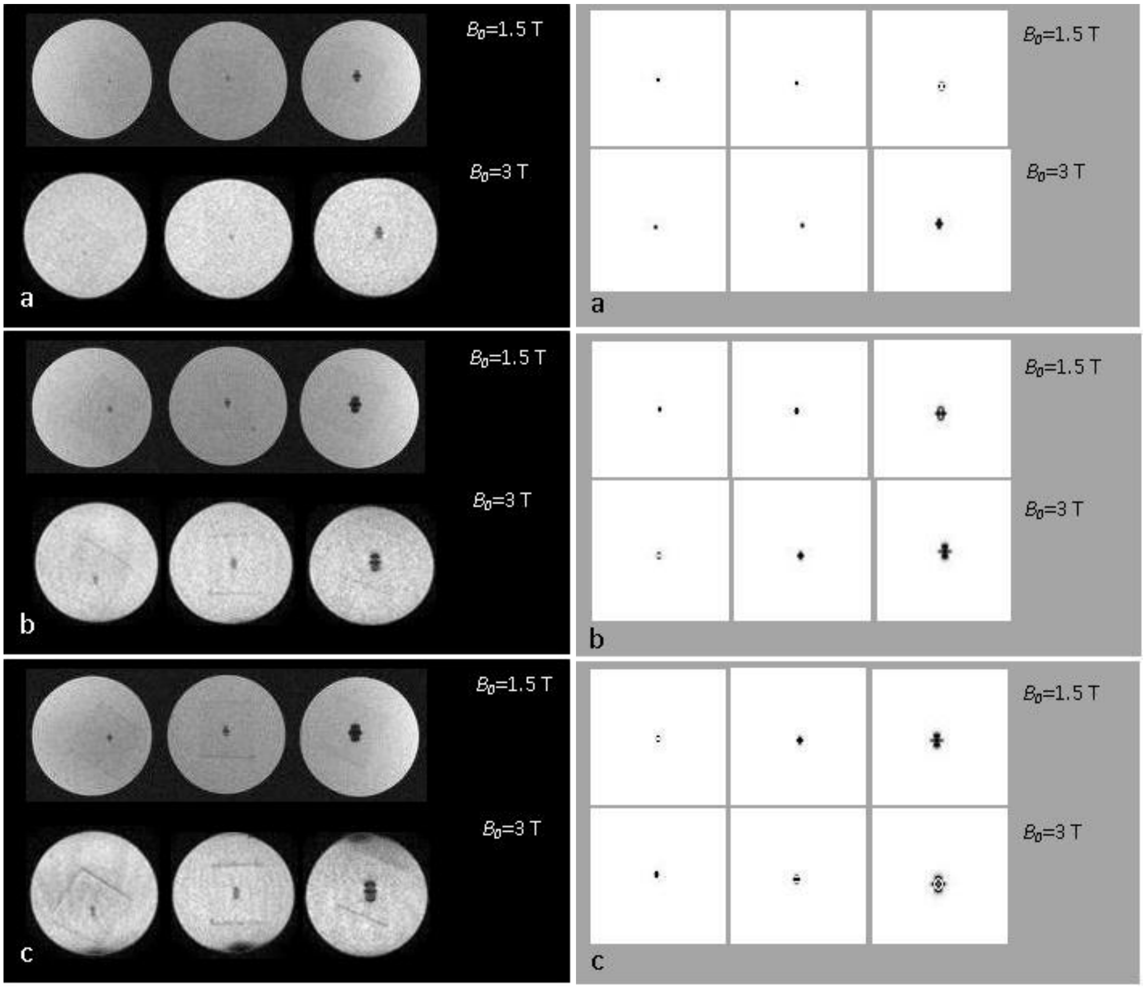

Amplification factors according to the scanner's magnetic field strength and the TE. The measured and the simulated results are shown in transversal and coronal planes:

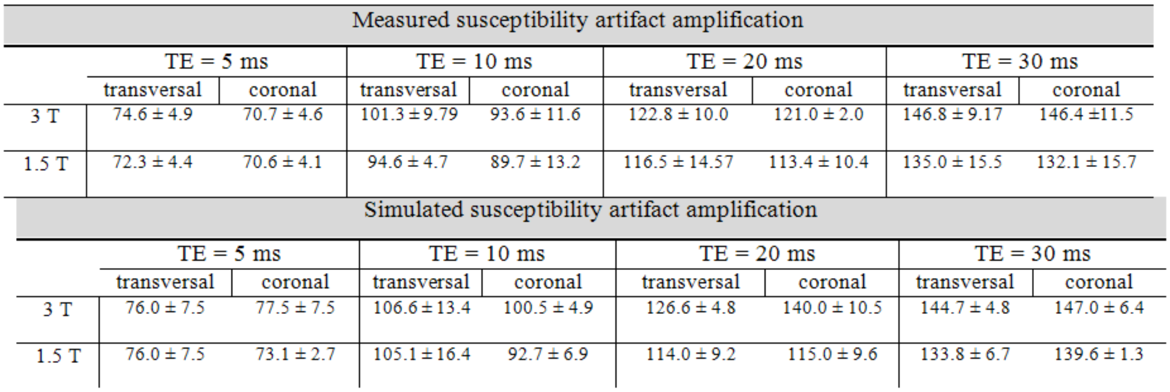

Measured susceptibility artifact amplification								
	TE = 5 ms		TE = 10 ms		TE = 20 ms		TE = 30 ms	
	transversal	coronal	transversal	coronal	transversal	coronal	transversal	coronal
3 T	74.6 ± 4.9	70.7 ± 4.6	101.3 ± 9.79	93.6 ± 11.6	122.8 ± 10.0	121.0 ± 2.0	146.8 ± 9.17	146.4 ±11.5
1.5 T	72.3 ± 4.4	70.6 ± 4.1	94.6 ± 4.7	89.7 ± 13.2	116.5 ± 14.57	113.4 ± 10.4	135.0 ± 15.5	132.1 ± 15.7

Simulated susceptibility artifact amplification								
	TE = 5 ms		TE = 10 ms		TE = 20 ms		TE = 30 ms	
	transversal	coronal	transversal	coronal	transversal	coronal	transversal	coronal
3 T	76.0 ± 7.5	77.5 ± 7.5	106.6 ± 13.4	100.5 ± 4.9	126.6 ± 4.8	140.0 ± 10.5	144.7 ± 4.8	147.0 ± 6.4
1.5 T	76.0 ± 7.5	73.1 ± 2.7	105.1 ± 16.4	92.7 ± 6.9	114.0 ± 9.2	115.0 ± 9.6	133.8 ± 6.7	139.6 ± 1.3

Depending on the TE values, the amplification factors vary in the ranges of 75 to 146 for the 3T MRI scanner and 72 to 135 for the 1.5T MRI scanner (Table 1). The simulation results and the in vitro measurements were compared using the paired Student's *t*-test with statistical significance defined for probability values less than 5%. The results showed no significant difference between the two observations with $p = 0.075$ and $p = 0.054$ for the 1.5 T and 3T scanners' results, respectively.

APPENDIX B – POSITIONING OF MAGNETIC MICROPARTICLES USING SUSCEPTIBILITY ARTIFACTS

Ferromagnetic materials induce a distorted region in MR images due to the field inhomogeneties caused by their high magnetic susceptibility. The field induced by sphere magnetic particles can be approximated by that of a dipole.

The susceptibility difference is the source of two types of artifact in MR images; geometrical distortion and echo shifting. Geometrical distortion is any misregistration of spin positions caused by field variations during frequency encoding [50, 58, 147]. If G' represents the static background gradient created by field inhomogeneties, spins residing at position x will be mapped to position x':

$$x' = x\left(1 + \frac{G'_x}{G_x}\right) \qquad (1)$$

Background gradient along the phase encoding direction (perpendicular to the readout direction) imposes a distortion on the voxel shape. Image distortion is reflected on both the gradient echo sequence (GE) and the spin echo sequence (SE). On the other hand, due to the 180° refocusing pulse of the SE sequences, the echo shifting effect only appears in GE images. The influence of a position dependent phase term is added to that of the unusual scaling of the k-space variable (as in SE) to determine the position of the spins:

$$\varphi(x) = -2\pi\gamma G'_x xTE \qquad (2)$$

When the phase dispersion is a nonzero positive integer multiple of 2π, the voxel signal vanishes completely. Therefore, echo shifting creates a signal loss in MR images. GE images are affected by both forms of artifacts; however echo shifting has a dominant effect on the geometrical distortion in GE scans. In [148], two different image simulations have been compared: a) based on geometrical distortion and phase dispersion and b) based on phase dispersion only. Significant deviations have been observed in the results obtained for high resolution images (< 100 µm) produced in high field MRI scanners. Nevertheless, for image resolutions of > 200 µm (clinical MR scanners) the difference has not been significant.

Total signal loss in GE imaging is expected to be independent of the in-plane resolution and the geometrical distortion [149]. Moreover, the position of the artifact is expected to reflect the exact position of the microparticle.

For intravoxel dephasing, the measured signal within the volume of interest in GE imaging and with a homogeneous

spin density (ρ) is described by:

$$S(t) = \int_v \rho \exp(-i\varphi(\vec{r},t))dv \qquad (3)$$

$$\varphi(t) = \gamma B_z(\vec{r})TE \qquad (4)$$

where φ is the phase dispersion across the voxel, TE is the echo time and γ is the gyromagnetic ratio for protons. The field distribution induced by ferromagnetic objects at position $\vec{r}$ varies as [147]:

$$\Delta B_z(\vec{r}) = \sum_{i=1}^{N} \frac{\mu_0}{4\pi}\left(3\left(\frac{(\vec{m}.\vec{r}_i)\vec{r}_i}{r_i^5} - \frac{\vec{m}}{r_i^3}\right)\right) \text{ with } \vec{m} = \frac{1}{6}\pi D^3 \vec{M}_{sat} \qquad (5)$$

where $\vec{m}$ is the net dipole moment, N is the number of the particles within the field of view (FOV), D is the diameter of the particles and $\vec{M}_{sat}$ is the magnetization saturation of the particles. The normalized signal is given by:

$$\frac{s}{s_0} = \int_v \rho \exp(-i\Delta B_z(\vec{r})TE)dv \qquad (6)$$

The susceptibility artifact of particles was simulated using MATLAB® programming language and based on the intravoxel dephasing caused by the phase accumulation at the TE in the GE scan (see equation (6)). The area of the S_{loss} was calculated by summing the in plane signal loss over the region of interest. Different distances and angles between microparticles were simulated to study the pattern of the artifacts and the minimum distance required to see them distinguishably. The images were evaluated for a coronal plane with a slice thickness of 3.5 mm and a pixel spacing of 0.5 mm. It was assumed that the microparticles are saturated at the magnetic field strength of 1.5 T.

Phantom experiments were carried out using chrome-steel microspheres (Salem specialty Ball Co., Inc.) measured 0.4 mm and 0.8 mm in diameter and a saturation magnetization of ~1.3×10^6

A/m. Pairs of particles at distances set to different multiples of their diameters (15×D, 30×D, 40×D and 80×D) were fixed on plastic plates.

Simulated GE signal intensity as a function of the distance between the particles on the coronal plane with the following scan parameters: B_0=1.5T, in-plane resolution = 0.5×0.5 mm^2 and TE=10ms: The distance is labeled by multiples of the particles' diameter (*D*). Curve labels indicate the diameter of the particles in micrometer.

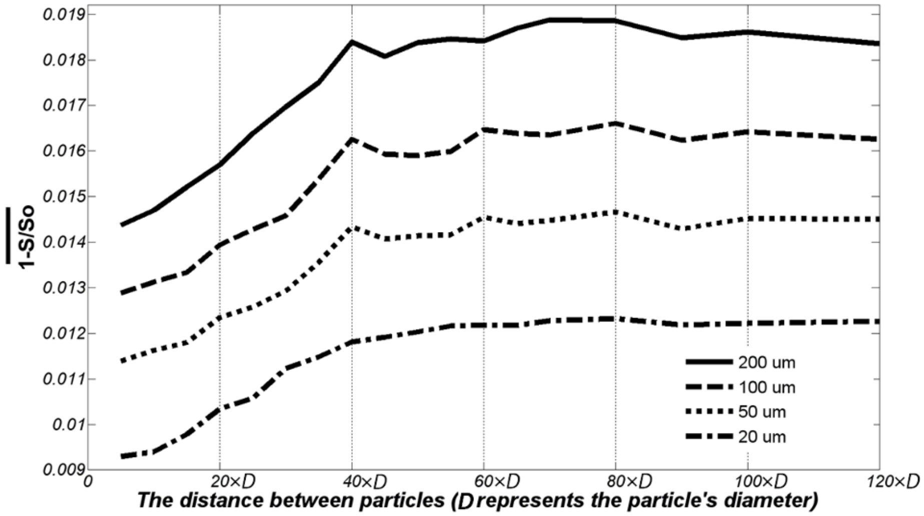

The distance is labeled by multiples of the particles' diameter (*D*). Curve labels indicate the diameter of the particles in micrometer.

GE simulated signal of the micropaticles measured 40 μm in diameter with the following scan parameters: B_0=1.5T, TE=10ms, in-plane resolution = 0.4×0.4 mm^2 distances at 15×D (a), 25×D (b) and 40×D (c):

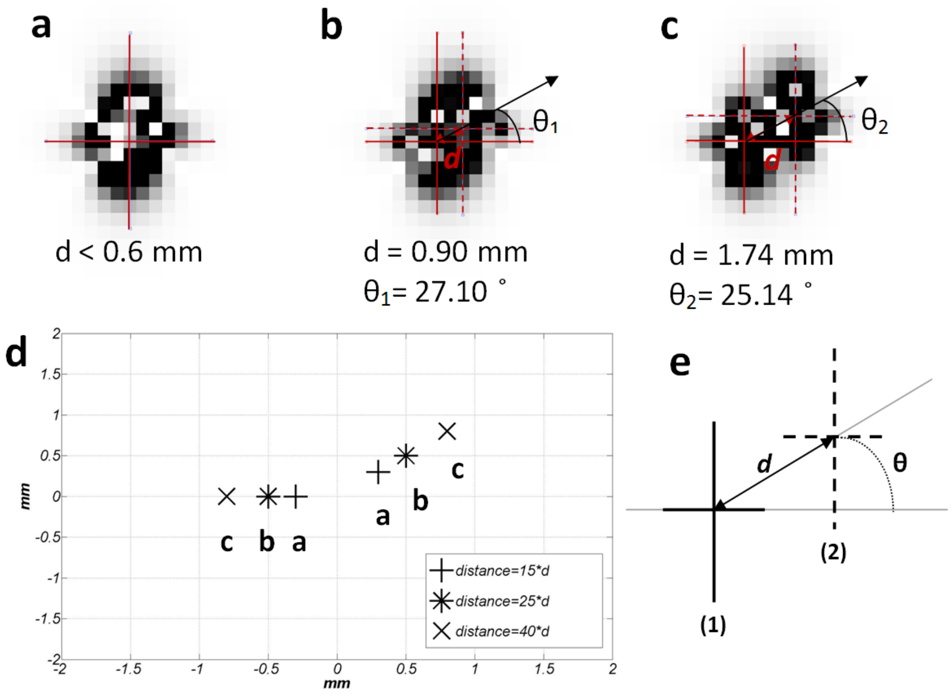

Each pair of the particles were distanced and angulated according to the plot d. The centers of the artifacts (1) and (2) were used to calculate the distance and the angle between the particles (e).

GE simulated signal of the micropaticles measured 20 μm in diameter using the following scan parameters: B_0=1.5T, TE=10ms, in-plane resolution = 0.2×0.2 mm^2 (*a*) and 0.5×0.5 mm^2 (*b*):

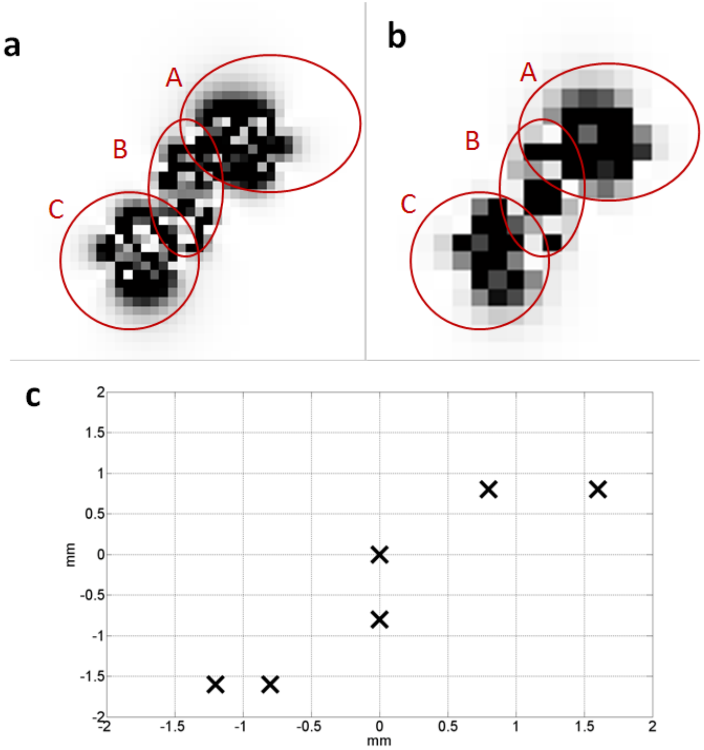

The particles are distributed according to the plot *c*. Circled regions show particle pairs with different spacing. Region A presents two particles distanced within 15×D and 40×D. Region B and C present two particles distanced at 40×D and smaller than 15×D, respectively.

Experimental (odd rows) and simulated (even rows) coronal images of 0.4 mm and 0.8 mm chrome-steel microspheres; (*a*) a single microparticle and (b) to (e) pairs distanced at 15×D, 30×D, 40×D and 80×D respectively:

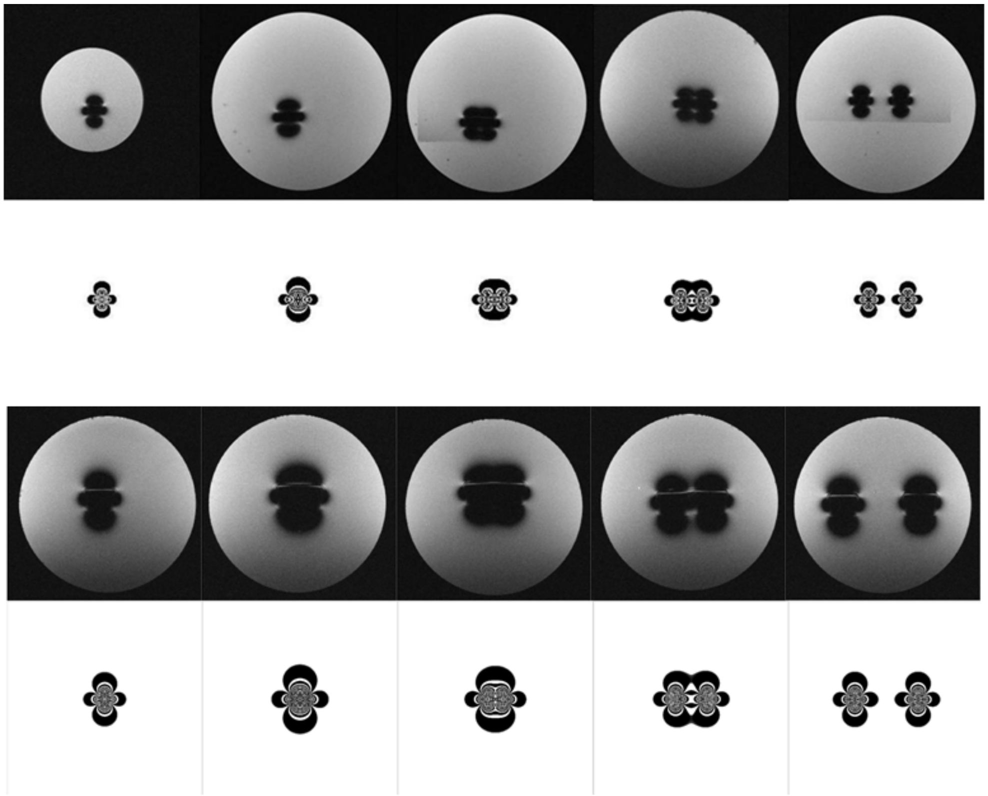

Identical scan parameters were B_0=1.5T, in plane resolution 0.6×0.6 mm^2 and TE=10 ms.